UNIVERSITY OF OKLAHOMA

GRADUATE COLLEGE

EHD-INDUCED FLOW AND HEAT TRANSFER IN A SQUARE CHANNEL

A DISSERTATION

SUBMITTED TO THE GRADUATE FACULTY

in partial fulfillment of the requirements for the

Degree of

DOCTOR OF PHILOSOPHY

By

JINFENG ZHANG
Norman, Oklahoma
2010

EHD-INDUCED FLOW AND HEAT TRANSFER IN A SQUARE CHANNEL

A DISSERTATION APPROVED FOR THE
SCHOOL OF AEROSPACE AND MECHANICAL ENGINEERING

BY

Dr. Feng C. Lai, Chair

Dr. M. Cengiz Altan

Dr. Wilson E. Merchan-Merchan

Dr. Takumi Hawa

Dr. Shihshu Walter Wei

To my husband and parents
for their love and support

ACKNOWLEDGMENTS

I would like to address my deepest gratitude to Professor Feng C. Lai for being such an excellent advisor. It was his guidance, suggestions, and patience that provided me the driving force for the completion of this work. Over the three years of experience working with Professor Lai, the knowledge I have gained has been tremendous. His great work ethic and personal merits are qualities to which I shall aspire for the rest of my life. I greatly appreciate all the opportunities that he created for me to participate in various conferences, which have improved my presentation skills considerably. Most importantly, his financial support over my entire period of study has made everything possible. I feel extremely lucky to have had Professor Lai as my advisor.

I also would like to thank Professor M. Cengiz Altan, Professor Wilson E. Merchan-Merchan, Professor Takumi Hawa, and Professor Shihshu Walter Wei for their time, effort, and valuable suggestions as members of my dissertation committee. In addition, I want to express my appreciation to Professor Peter J. Attar and Professor Prakash Vedula for their generous time and helpful discussions on certain problems. Their hard working ethic is a great inspiration to me.

The opportunities of being a teaching assistant for the past years are greatly appreciated. Therefore, a special thank goes to the Department of Aerospace and Mechanical Engineering.

All of the help from my colleagues need to be recognized. I have benefited the most from Mr. Robert L. Marvel for his comprehensive experience and excellent

computer skills. His generosity with his time and willingness to help are gratefully acknowledged. Additionally, he is a fun person to be around. His authentic humor makes the work environment more pleasant. Dr. Noel Brown and Dr. Chean Chin Ngo, who previously worked here, have provided a great start for my experimental study. I have received a lot of help from friends. Without them, this work would not have been accomplished successfully.

I am also deeply grateful to my husband, Brett Z. Sullivan, for everything he has done for me. It is his love and encouragement that provided me with enough energy every day to complete this endeavor. His caring and understanding are the foundation of this accomplishment. I am greatly indebted to all the generous support and unconditional love from my parents Peixing Wang and Jianmin Zhang. They are the reason that I have come this far.

TABLE OF CONTENTS

LIST OF TABLES

LIST OF FIGURES

ABSTRACT

Induction of a fluid flow within a square channel using electrohydrodynamic (EHD) principles and consequent effects on heat transfer enhancement are examined using both experimental and numerical methods. Experiments are conducted first to provide important information for computing the electric field in the numerical study.

EHD-induced flow in a square channel is investigated via experimentation. Electrode pins are flush mounted on the channel walls and charged with a high voltage. Three such configurations of the EHD gas pump are tested (with 4, 12, and 28 electrode pins, respectively) for a wide range of operating voltages starting from the corona threshold voltage up to 28 kV. Both corona current and corona wind velocity inside the channel are measured for operations using either positive or negative corona discharges. The performance of the EHD gas pump is then evaluated against that of conventional fans. The experimental results provide important insights for the optimal design of an EHD gas pump.

A numerical model is developed based on the experimental study. The three-dimensional governing equations for the electric, flow, and temperature fields are solved using the finite difference method. Corona-driven flow is calculated first, and its results are compared with the experimental data to validate the computational code. The numerical results enable vivid flow visualizations inside the channel, providing a great understanding of the development of the induced flow.

With forced convection, the influence of electric field on the flow and temperature fields is investigated. Numerical calculations are performed on the EHD gas

pump with all three electrode configurations at various applied voltages and a wide range of Reynolds numbers. The heat transfer enhancement and thermal hydraulic performance are then evaluated. The results of the numerical study show that EHD technique has a great potential for many engineering applications.

CHAPTER ONE

INTRODUCTION AND LITERATURE REVIEW

1.1 Introduction

The use of electrical field to modify the heat and mass transfer process of fluid flow has been a subject of great interest for many decades. The mechanism of this approach is based on using an electrical body force to induce a secondary flow, or simply create a flow where none would otherwise exist. A corona discharge occurs in the narrow region close to a needle or a wire electrode, and gas molecules are ionized by a high electrical field. These ions, controlled by the Coulomb force, migrate to the grounded electrode. During the migration to the grounded electrode, these ions transfer their momentum to neutral molecules via collision (Fig. 1.1). This creates a bulk flow, which is usually called ionic wind, or corona wind [1].

Electrohydrodynamic (EHD) flows have been applied to wide industrial and engineering fields. For example, in the food industry, corona wind has become a novel drying method to enhance the dehydration process [2-4]; in the aerospace industry, EHD actuators are used to reduce the drag of an aircraft or to stabilize the air flow [5-9]; in the thermal management of electronic systems, corona wind can produce a substantial increase in the heat transfer coefficient [10-12], which is also referred to as the electrohydrodynamic (EHD) enhancement technique. In addition, EHD technique has been widely used in manufacturing and power industries (i.e., electrostatic precipitators) to control particle emission and increase the efficiency of particle collection [13]. Recently, as mircroelectronics has become an emerging technology, EHD techniques

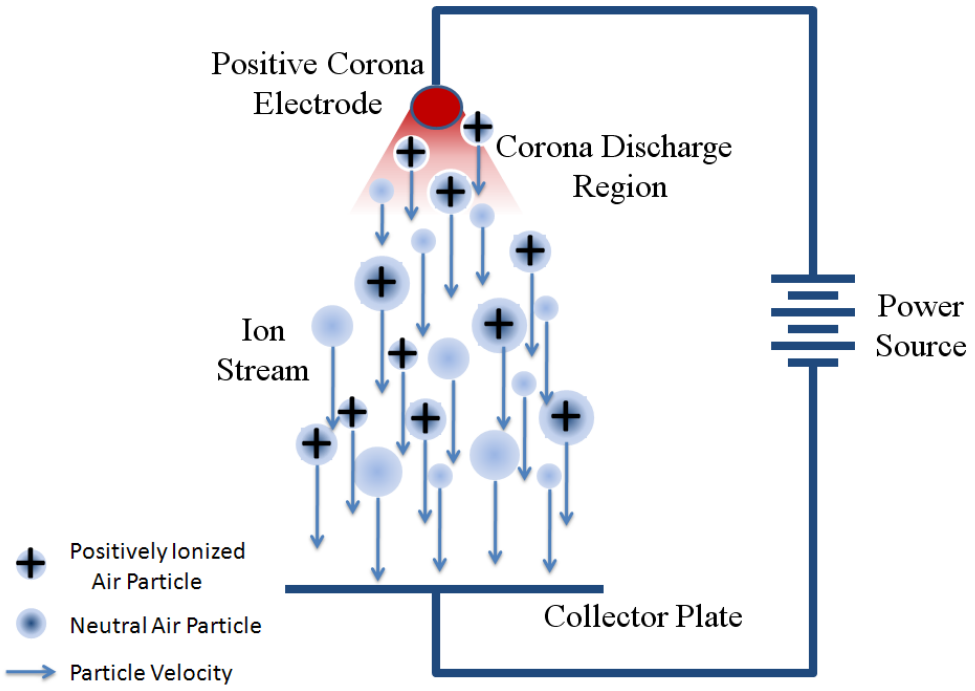

Figure 1.1 Mechanism of corona wind

have played an important role in the development of microelectromechanical system (MEMS) [14].

The advantage of this EHD technique is that it directly converts electric energy into kinetic energy without involving moving mechanical parts, and therefore the maintenance cost can be greatly reduced. Secondly, this technique is operated electronically, and it may be incorporated into the existing thermal systems and conveniently controlled by computer. Thirdly, it is highly compatible with chips and chip-level structures. Thus, miniaturization can be easily implemented [15]. Lastly and most importantly, the power consumption is usually very small, which makes this technique particularly attractive from the energy point of view. Its only disadvantage is the generation of extraneous gases such as ozone that might be harmful to human beings. However, ozone generation can be effectively monitored and minimized [16].

The characteristics of corona discharege vary significantly, depending on the working medium, device configuration, and ambient conditions. Corona discharge can occur either in liquids or gases. However, the liquid state is usually more chemically reactive compared to that of gases, which makes the electrohydrodynamic study more complicated. Device configurations are mostly determined by the purpose of their applications and directly affect the energy efficiency. The performance of corona wind is very sensitive to ambient conditions, such as temperature, pressure, and relative humidity, etc. For example, it has been shown that humidity affects the corona onset voltage [17]. The discharge current decreases when air humidity increases in the range between +20 ℃ and +65 ℃, but the wall temperature has no influence over the discharge [7]. In addition, the efficiency of the corona wind device depends on the polarity that it operates. In the case of corona surface treatment which improves flow separation, it has been found that negative coronas are generally less efficient than positive coronas [18].

1.2 Literature Review

Numerous studies have been conducted in various fields that utilize corona discharge. This study has been focused on the effect of corona discharge on a flow field, specifically air flow, and the resulting heat transfer enhancement.

1.2.1 EHD-Induced Flow

Rickard, et al. [19] investigated the characteristics of ionic wind velocity in a tube with a pin-to-ring electrode geometry for negative corona discharge. Both particle image velocimetry (PIV) and hot wire anemometry were used to validate their results. The velocity profile showed a velocity deficit at the core of the flow. In addition, a

converging nozzle was placed at the exit of the tube with an intention to accelerate the gas flow produced by the ionic wind generator. However, only a slight increase in the velocity was achieved by using the converging nozzle.

Chang, et al. [20] conducted experiments on the onset of EHD-induced turbulence over a cylinder in cross flow. The Reynolds number in their study ranged from 0.2 to 80 based on the cylinder diameter. The results showed that EHD turbulence could be generated even with Reynolds numbers of less than 0.2 if the EHD number (Ehd) was greater than the Reynolds number squared ($Ehd > Re^2$). Also, PIV images illustrated that the onset of EHD turbulence was usually initiated downstream of the near stagnation point.

A wire-non-parallel-plate EHD gas pump was experimentally investigated by Tsubone, et al. [21] to study the effects of various parameters, such as channel configuration, applied voltage and corona polarity. Their experiments were conducted with two different electrode configurations for both negative and positive applied voltages varying from 0 to 14 kV at atmospheric pressure and room temperature where air was the working fluid. A maximum gas velocity of 1.9 m/s, which corresponds to a volumetric flow rate of 44 L/min, was observed. The volumetric flow rate, gas velocity and pressure drop were found to increase with increasing applied voltage or EHD number. Numerical results [22] agreed qualitatively with these experimental results.

The flow characteristics of a wire-rod type EHD gas pump were studied by Komeili, et al. [23] for various pipe diameters. Experiments were conducted for negative DC applied voltage ranging from 0 to 24 kV. A maximum gas flow rate of 40.1 L/min

was generated for a pipe diameter of 20 mm, with a grounded rod electrode of a diameter of 3.1 mm and an electrode spacing of 12.6 mm. Their results showed that for the same pipe diameter and electrode spacing, the velocity generated increased with the rod diameter. However, for a fixed gas velocity it was better to use a rod electrode with a smaller diameter as it would generate the same flow velocity for a lower power consumption.

A similar wire-rod type of EHD gas pump was examined by Takeuchi, et al. [24] to study the effect of wire electrode diameters on the flow field when operating at both positive and negative polarities. In their experiments, the diameters of the wire electrode were 60 μm, 200 μm, and 300 μm, and that of the rod electrode 3 mm. It was found that a smaller diameter of the wire electrode produced a larger corona current and a higher flow velocity for both positive and negative discharges. A maximum flow velocity of 2 m/s was observed with a wire diameter of 60 μm and an applied voltage of -16 kV. In addition, the corona current and flow velocity were observed to fluctuate around an average value. Also, optical images showed that corona tufts were generated under negative discharge whereas steady glow coronas were observed with positive discharge.

Moreau and Touchard [25] conducted experiments to investigate the efficiency of an EHD gas pump with a grid-and-ring grounded electrode. The influence of several parameters, such as electrode polarity, collecting electrode geometry, electrode sapcing and tube diameter, were studied to optimize the design of EHD gas pumps. Their results showed that the maximum velocity was higher for the case of positive coronas than that of negative ones. In other words, the efficiency of negative coronas was smaller than that of positive ones. Using a grid as the collecting electrode was more efficient than a ring. In

their experiments, the most efficient configuration produced a corona wind of 10 m/s and a flow rate of about 1 L/s, which required a mechanical power of a few mW with an efficiency of about one percent.

1.2.2 EHD-Enhanced Heat Transfer

Robinson [26] experimentally investigated the heat transfer enhancement by utilizing the corona discharge on both natural and forced convections. His experiment was conducted using a wire-tube electrode configuration. With the heated wire electrode at the center of the channel, the gas density decreased and resulting in the change of air mobility. It was found that the decreased air density close to the hot wire lowered the corona onset voltage. In the case of the natural convection, corona wind could increase the heat transfer rate fourfold when the wire was at 500 °F. However, the heat transfer enhancement due to the corona wind in forced convection was less effective, but still significant. For example, with an incoming flow velocity of 92 ft/s, a 10 % increase in heat transfer was observed by using the corona wind. When compared to Robinson's study, Velkoff [27] demonstrated that if the tube was the heated element instead, the heat transfer contribution by the corona wind to the existing forced flow was negligible.

Kalman and Sher [28] proposed an electrostatic blower, which utilized the corona wind produced by electrodes to cool heated surfaces, such as power-unit chips. It was concluded that the heat transfer coefficient can be easily increased by a factor of more than two, as compared to that by natural convection. Also, the conversion efficiency of electrical energy into mechanical energy with positive corona was higher than that of negative corona.

Go, et al. [29] conducted experiments to examine the heat transfer enhancement by corona wind in the presence of forced convection. In their experiments, the wire electrode and the collecting electrode plate aligned so that the corona wind is in the direction of the bulk flow. Their results showed that the local heat transfer coefficients were increased by 200 %, and the maximum enhancement occurred in the vicinity of the electrode wire. It was also shown that the heat transfer coefficient was proportional to the fourth root of the corona current both analytically and experimentally. In addition, an increase in the spacing between the electrodes did not affect the local peak enhancement, but increase the area of heat transfer enhancement. Their numerical simulations confirmed the experimental observation that the local maximum heat transfer enhancement took place upstream of the collecting electrode and close to the emitting electrode [30].

A numerical and experimental investigation was performed by Molki, et al. [11] to study the effect of corona wind on the flow field and heat transfer enhancement of air flow in a channel. The experiments were conducted using a horizontal, square channel with a wire electrode placed at the centerline of the channel. A uniform wall heat flux was applied as the thermal boundary condition. The numerical model was based on Large-Eddy Simulation (LES) to take into account any potential turbulence generated by the electrical field. However, numerical results showed that the flow did not fluctuate, and turbulence did not appear in the flow. The Reynolds number in their study ranged from 500 to 2000. The maximum heat transfer enhancement in the fully-developed flow regime was $Nu/Nu_0 = 3.4$, while that in the developing flow regime was much smaller, ranging from 1.56 to 2.01. As an extension, flows with a wider range of Reynolds

numbers, varying from 500 to 10,000, were studied numerically using the turbulence k-ω model [12]. The normalized Nusselt number, Nu/Nu_0, was reported to vary from 1.06 (Re = 10,000 and 8.1 kV) to 13.58 (Re = 2000 and 11.7 kV). The numerical results revealed that the secondary flow induced by the corona discharge was the main mechanism behind the heat transfer enhancement for both developed and developing flow regimes. In addition, a hysteresis effect of corona discharge was reported in their experiments, which demonstrates that the corona currents were lower during the tests with increasing voltage than those with decreasing voltage. This observation was consistent with the findings of Chang, et al. [31-32].

Molki and Bhamidipati [33] also conducted experiments to study the level of heat transfer enhancement by corona wind in a circular tube for the transitional and lower ranges of turbulent flows with Reynolds number varying from 2500 to 13000. The maximum enhancement of the local and average heat transfer coefficients were 14-23% and 6-8%, respectively. The enhancement produced by corona wind in the low-Reynolds-number flows was much more pronounced, which indicates that, at higher Reynolds numbers, corona wind is suppressed by turbulence and become less effective.

Shooshtari, et al. [34] reported that the implementation of corona wind in small scales was not only feasible, but also preferable as it could lead to considerable heat transfer enhancement. Their experiments were conducted using on a square channel with a hydraulic diameter of 10 mm and a uniform heat flux around the channel wall. It was shown that heat transfer enhancement up to 200% was attainable while the amount of EHD power was only about 1.13 W. A three-dimensional numerical model was developed to validate the experimental results. It was concluded that the experimental

results agreed well with the numerical solutions in which the Joule heating effect was not considered.

A two-dimensional numerical simulation was carried out by Ahmedou and Havet [35] to study the EHD-enhanced heat transfer for a wire-plate configuration. Their results showed that a three-fold increase of local heat transfer coefficient was achieved at a Reynolds number of 3846 with single-wire plate configuration. No significant heat transfer enhancement was produced at higher Reynolds numbers. In addition, the average heat transfer coefficient decreased with an increase in the number of wires, which implies that in the case of multiple wire-plate geometry, the spacing between wires is an critical factor to the heat transfer enhancement.

The existence of oscillatory flows, induced by the electrical field under forced convection, was first reported by Lai, et al. [36-38]. The oscillatory flows were the product from the interactions between the electrical body force and the flow inertia of the primary flow. Their numerical results showed that the flow and temperature fields under the influence of an electrical field may became steady, periodic or non-periodic, depending on the flow Reynolds number and EHD number. The heat transfer enhancement by oscillatory flows was more effective than that of steady flows.

1.3 Objective of Present Study

Previous studies reveal that an EHD-induced secondary flow has significant influence on the primary flow and the resulting heat transfer coefficient. These influences directly depend on the device configurations and its electrode arrangement. The majority of studies on EHD applications so far has the emitting electrode (either single or

multiple) located at the center of the channel. To achieve the maximum heat transfer, the boundary layer near the channel wall needs to be perturbed. Placing the emitting electrode (and thus the corona-driven flow) close to the wall can produce this disturbance more efficiently, which in turn leads to a better performance on the heat transfer enhancement. Surface corona refers to the electrodes being flush mounted on the surface of the plate or the wall. Recent research [8, 39] on the surface corona are focused on flow control and drag reduction. However, it also has great potential on the heat transfer enhancement.

Most studies on EHD are based on experiments because of the complications involved. With the advancement of computer technology, numerical simulations are becoming more popular as they are cost effective and less affected by the ambient conditions. However, most numerical models for EHD applications are two-dimensional [40], and only very few are three-dimensional [34, 41]. Due to the interactions between the electric, flow, and temperature fields, solving EHD problems in three-dimensions is quite complicated and challenging. Until now, there has been no reported numerical study on heat transfer enhancement using surface corona.

The present EHD gas pump design consists of electrodes flush mounted on the inner wall of a square channel. For forced convection, the EHD-induced secondary flow directly interferes with the boundary layer, causing additional mixing and leading to an increase in the convective heat transfer coefficient.

The purpose of the present study is to evaluate the performance of an EHD gas pump and its application in the field of heat transfer. First, experiments are conducted to

study the EHD-induced gas flow alone in a square channel with electrodes flush mounted on the wall. Several important parameters, such as the number of electrodes, their corresponding arrangement, applied voltage and polarity, are investigated in search of the optimal operating conditions for its performance. Experimental results not only provide important insights to the design of an EHD gas pump, but also contribute important information for the subsequent numerical study. The second part of this study investigates the resulting heat transfer enhancement using numerical simulations. A three-dimensional model is developed based on the experimental results. Corona-driven flow is tested, and its results are compared to the experimental data to validate the numerical code. Once validated, thermal boundary conditions are applied, and forced convection is studied to determine the heat transfer enhancement induced by the electric field.

CHAPTER TWO

EXPERIMENTAL STUDY

The experimental study was conducted in the Heat Transfer Laboratory at the main campus of the university. This chapter presents the experimental setup, procedure, and results of the electrohydrodynamic gas pump in a square channel. Corona current and corona wind velocity measured from experiments provides important information for future numerical simulation.

2.1 Experimental Setup and Apparatus

The experimental setup used in this study is shown in Fig. 2.1. The main components of the setup are: EHD pump test unit, high voltage power supply, air velocity transducer, and data acquisition system (DAQ). The detailed descriptions about each unit are given below.

2.1.1 EHD Pump Test Unit

The channel is made of Plexiglas with 1/4 inch thickness, and the inner dimensions of the channel are 4 inches by 4 inches with a length of 20 inches. A copper wire loop is flush mounted on the inner wall of the channel. Several one-inch wire pins are welded with the loop and serve as the emitting electrodes. The size of the copper wire is 20 GA (0.03196 in. diameter). A 1/2 inch wide and 0.025 inch thick copper strip is also flush mounted on the inner wall and serves as the grounded electrode. The distance between the wire loop and the copper strip is 2.5 inches. It is necessary to include the wire pins to create a non-uniform electric field to induce the generation of corona wind.

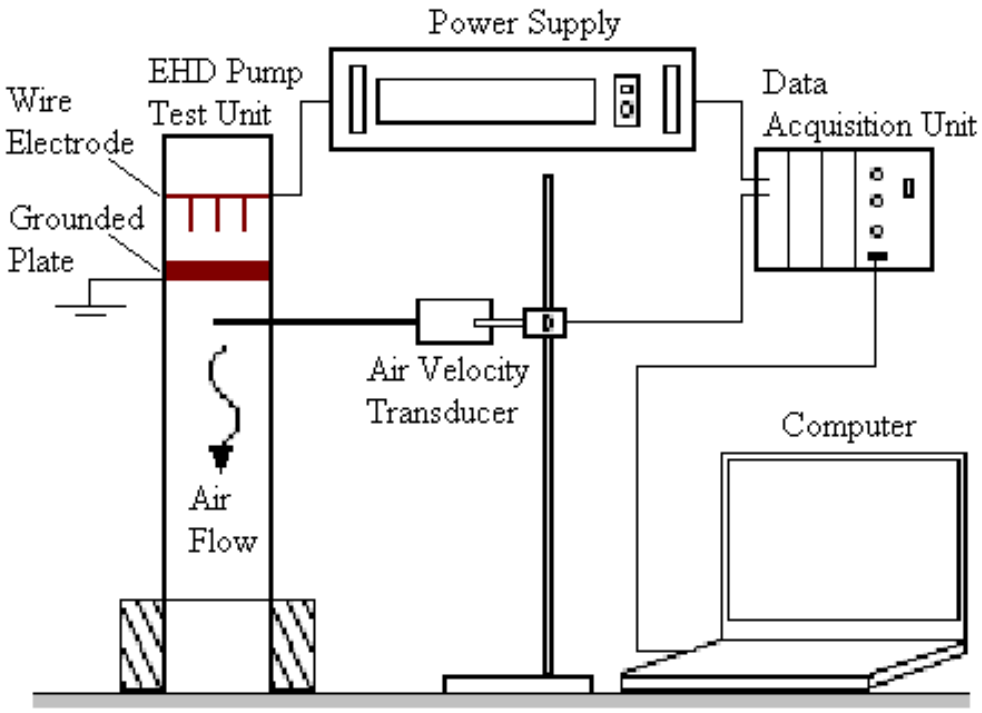

Figure 2.1 Experimental setup

Without these pins, the electric field inside the channel is uniformly stratified and no flow can be initiated from that particular configuration.

This experiment is conducted with three electrode configurations: 4 pins, 12 pins, and 28 pins. For all the configurations, pins are distributed evenly onto the channel walls. For example, in the case of 4 electrode pins (Fig. 2.2), there is one pin in the middle of each wall. Similarly, three pins are placed on each wall for the configuration with 12 electrode pins, and 7 pins per wall for the configuration with 28 pins.

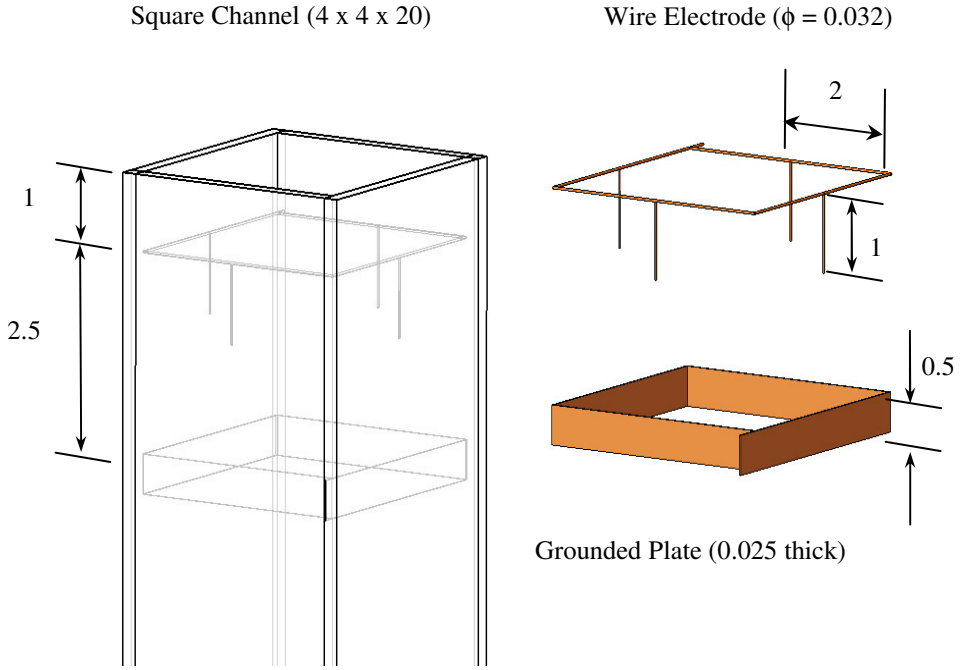

Figure 2.2 Configuration of EHD pump test unit (4 pins, dimensions in inches)

2.1.2 High-Voltage Power Supply

The voltage applied to the wire electrode is supplied by a DC power supply manufactured by Bertan Associates, Inc. (Series 205 B-30R) as shown in Fig. 2.3. It is important to have a DC electric field to produce the corona wind, since an AC field has no effect on the production of corona wind [42]. A maximum voltage of 30 kV can be provided by the power supply with either positive or negative polarity. The accuracy of this power supply's voltage is $\pm$ 0.1% of reading and + 0.1% of maximum. It is $\pm$ 0.25% of reading and + 0.25% of maximum for current.

Figure 2.3 High voltage power supply

2.1.3 Velocity Transducer

A hot-wire anemometer (Omega FMA 902-I) (Fig. 2.4) can accurately measure air velocity from 0 to 500 fpm (2.54 m/s) with an accuracy of 2.7% of full scale at room temperature. To facilitate air flow measurement, the anemometer is securely mounted in the channel with the use of 1/4-inch NPT compression fittings. These fittings are installed on three levels; 1, 2.5 and 4 inches downstream of the grounded plate. A total of nine sampling points are evenly distributed on each level. Figure 2.5 illustrates the locations of these velocity measurement points.

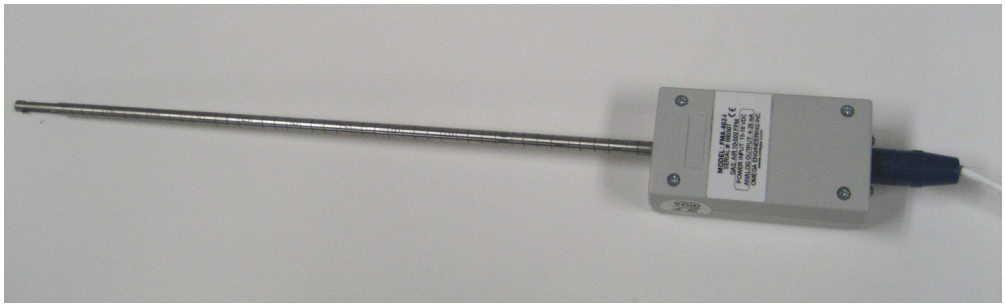

Figure 2.4 Air velocity transducer

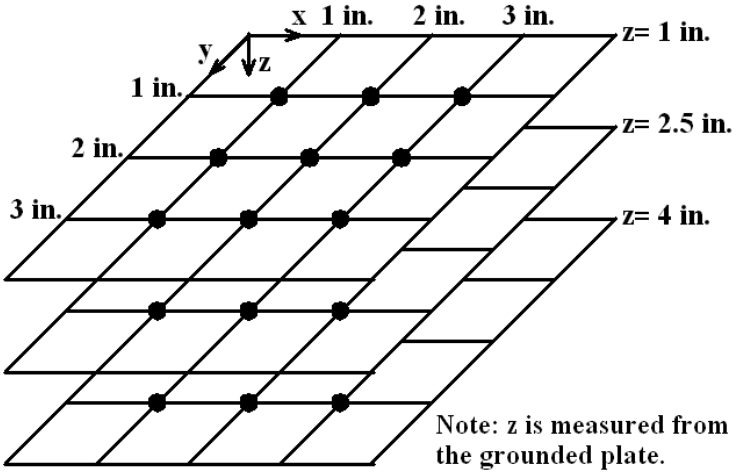

Figure 2.5 Locations of velocity measurement points

2.1.4 Data Acquisition System

The data acquisition system used is SCXI-1000 chassis and SCXI-1308 module from National Instruments, as shown in Figure 2.6. The data sampling and collection are aided by using the LabView program. The current signal received from the power supply and the velocity transducer are first calibrated and scaled to the correct current and air velocities. A sampling rate of 5 Hz is used for all experiments. It is determined by systematic trials that 5 Hz is sufficient to capture the variations of electric and flow fields.

Figure 2.6 Data acquisition system

2.2 Experimental Procedures

Experiments are conducted for three electrode configurations of the EHD pump with 4 pins, 12 pins, and 28 pins. Both positive and negative polarities are considered for comparison. The steps in each test are outlined as follows,

1. Data acquisition system is connected with the air velocity transducer and the power supply. A virtual instrument (VI) is built in LabView to collect and record the signals. The range of an input signal for the DAQ module is from 0-5 V or 0-20 mA. The output signals range from 0-5 V for the power supply and 4-20 mA for the velocity transducer. These signals vary linearly with the current from the power supply and the velocity at the transducer. Therefore,

the signals received from the power supply and velocity transducer can be scaled to the correct corona current and air velocity.

2. The high-voltage power supply is set to the desired polarity.
3. The wire electrodes are connected to the high voltage power supply and the copper strip is grounded.
4. The air velocity transducer is properly aligned to the flow and the sensor is positioned at the testing point.
5. The power supply is then turned on and the voltage is slowly increased until it reaches the threshold voltage, at which point a hissing sound can be heard. This threshold voltage marks the onset of corona discharge.
6. The current collected on the grounded plate and the velocity measured by the transducer are recorded by data acquisition system. The data collection starts from the threshold voltage up to 28 kV with an increment of 2 kV.
7. Steps 2 through 6 are repeated at each one of the 27 velocity measurement points for all three electrode configurations in both positive and negative polarities.

It is important to know the onset voltage and sparkover voltage for EHD gas pumps before starting the experiment. Operating at or beyond the sparkover voltage may damage the power supply or the data acquisition system. In the current study, the onset voltage is found to be 18 kV for most cases, except for the case with 28 electrode pins under positive polarity. This case has the threshold voltage around 21 kV. For all configurations, the sparkover voltage goes beyond 30 kV, which is the maximum output

voltage of the power supply. However, as the voltage approaches 30 kV, the corona current becomes increasingly unsteady.

This study is used to measure the corona current without forced air flow and heat transfer. Previous work by Molki, et al. [11] shows that the voltage-current relation (V-I curve) for flow through square ducts is independent of Reynolds number. Therefore, current measured from experiments without air flow can be used for future numerical simulation of forced flow and heat transfer. A picture of the complete experimental setup is depicted in Fig. 2.7.

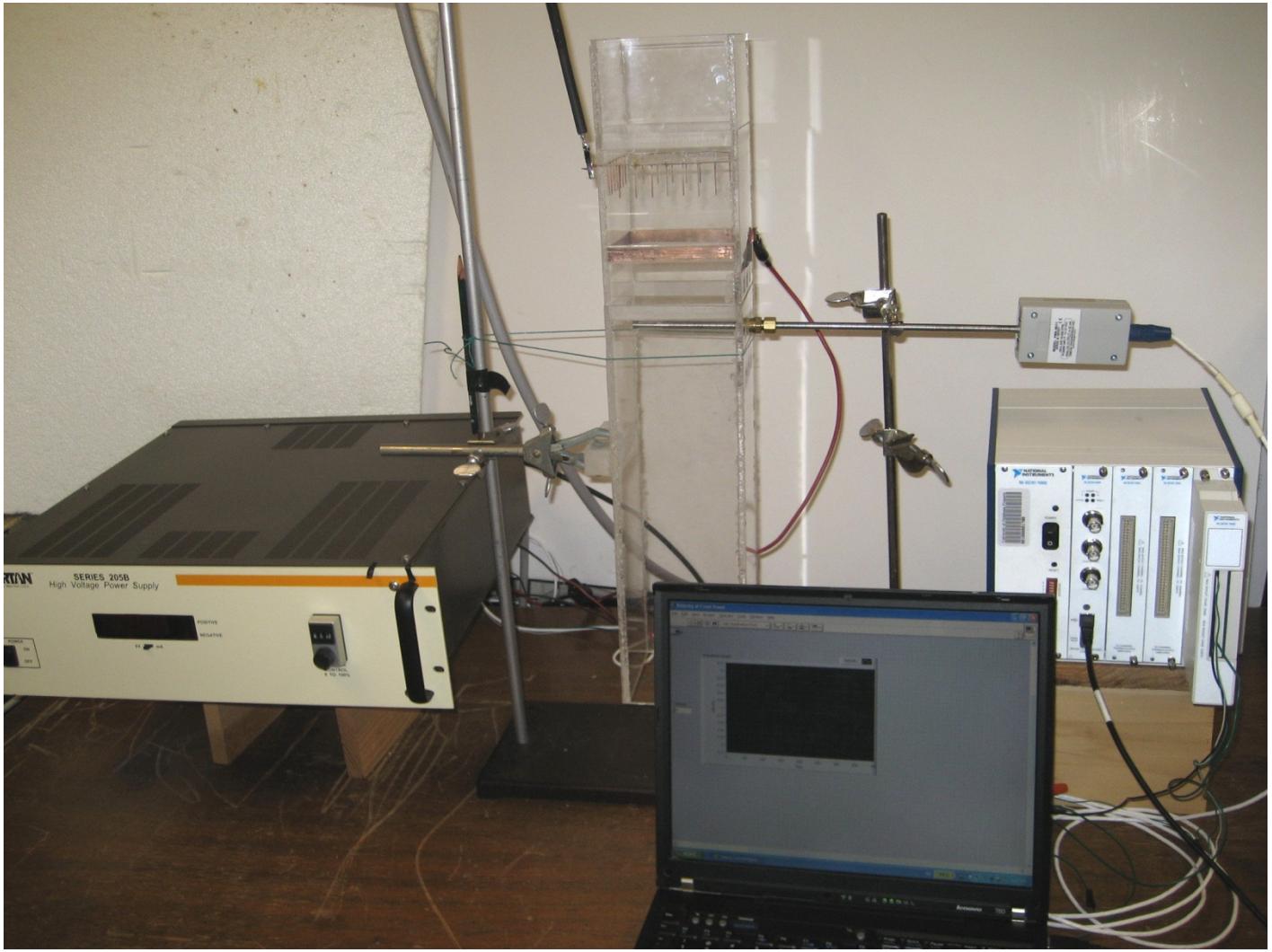

Figure 2.7 Photograph of experimental setup

2.3 Results and Discussion

2.3.1 Corona Current

The corona discharge phenomenon is sensitive to the ambient temperature and relative humidity. For the current study, all the experiments are conducted with the room temperature and the relative humidity varying within the range of 19-23℃ and 17-35%, respectively. Typical V-I curves for the three wire-electrode configurations operating under positive and negative corona discharges are shown in Fig. 2.8. An EHD pump with more electrode pins draws a larger current at a given applied voltage. This trend is more pronounced at a higher voltage. The slope of V-I curve becomes steeper as the number of pins increases, particularly for the case of 28 pins with positive polarity. In this case, the current increases dramatically as the voltage becomes larger. It is also noted that, for any configuration, an EHD pump operated in positive polarity requires a higher current than that operated in negative polarity.

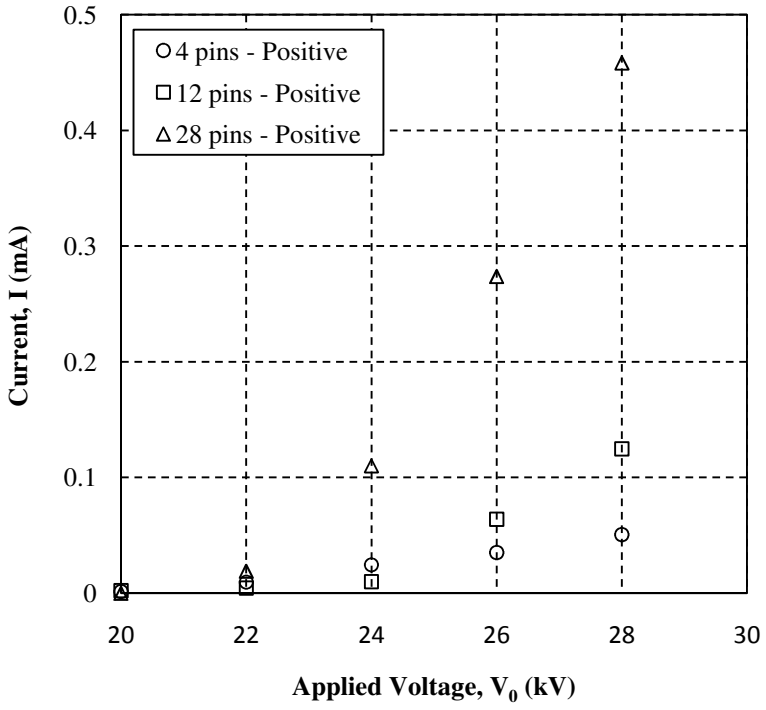

(a)

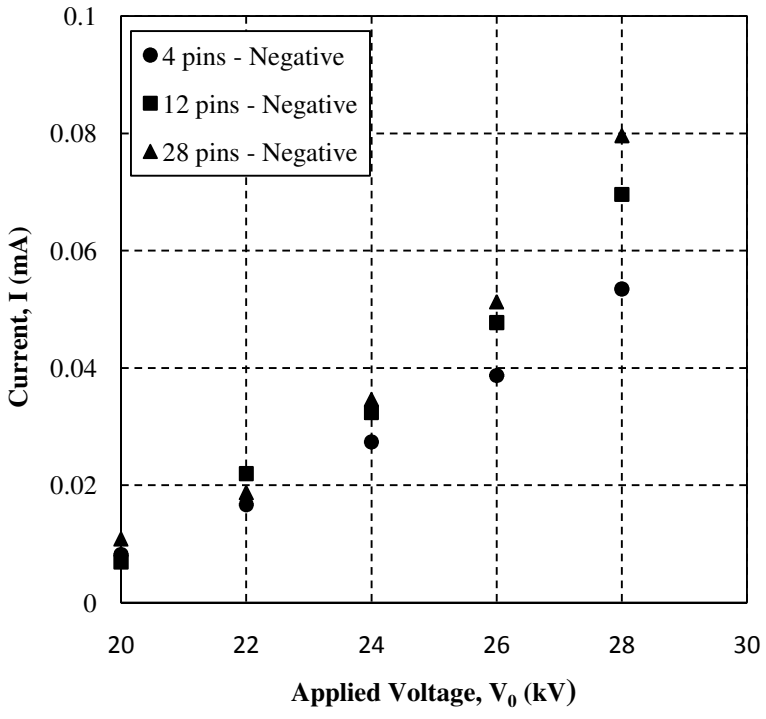

(b)

Figure 2.8 Typical V-I curves for EHD pumps
(a) positive polarity, (b) negative polarity

Figure 2.9 shows the variation of corona current with time for the configuration of 4 pins under positive polarity. A transient behavior is observed before the current reaches a steady state. This transient time period reduces as the applied voltage increases. The present observation is consistent with the findings of Moreau, et al. [7] and Molki and Damronglerd [12]. However, this unsteady behavior is contradictory to the conventional view that the corona current reaches a steady state within seconds.

In addition, it is observed that corona current fluctuates and it can be easily identified from Fig. 2.9 (c). Therefore, a time-averaged value for the time period after the current reaches steady state is used for further numerical study.

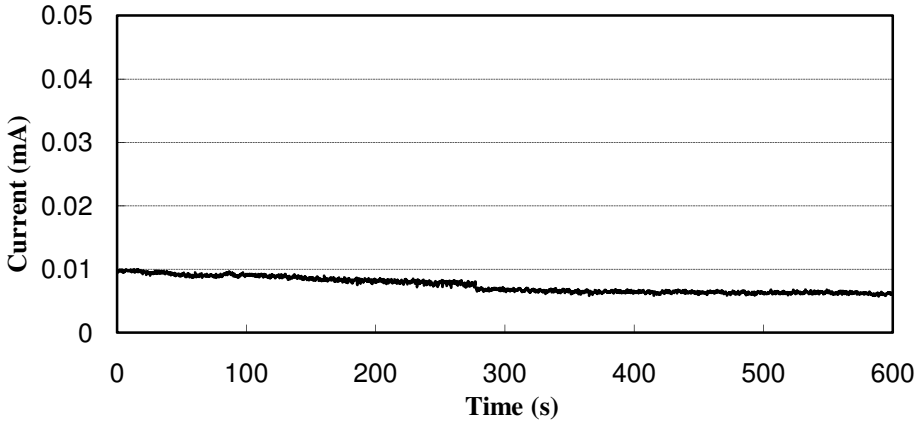

(a)

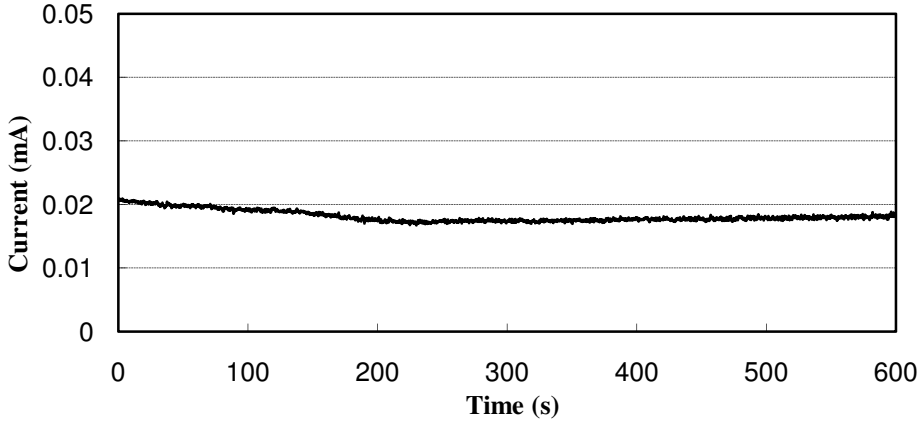

(b)

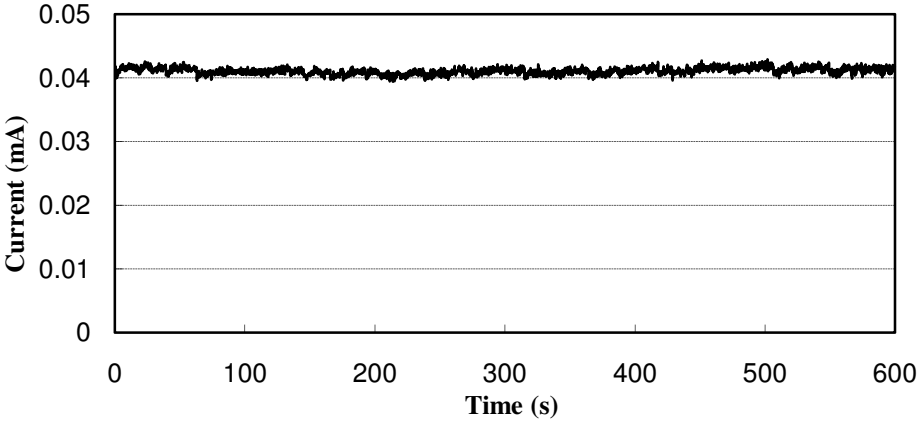

(c)

Figure 2.9 Variation of corona current with time
(a) V_0= 20 kV, (b) V_0= 24 kV, (c) V_0= 28 kV

2.3.2 EHD-induced Flows

To investigate the flow induced by the electric field, the variation of velocity with time is first shown in Fig. 2.10. Although this figure shows the case of 4 electrode pins with negative polarity at 24 kV, the features hold for all other cases. Air velocity fluctuates around an average value. Comparing to Fig. 2.9, this fluctuation is considered more rapid and violent than that of corona current. It is speculated that interactions of corona wind issuing from neighboring electrode pins might be responsible for the velocity fluctuations. Most importantly, the time-averaged velocity does not seem to change with time.

Figure 2.11 presents the time-averaged velocity at the center of the channel as a function of the applied voltage for the configuration of 28 electrode pins. As mentioned earlier, the air velocity fluctuates around a mean value. The error bar at each point in the figure represents the associated standard deviation. Regardless of the polarity, the velocity increases with an increase in the applied voltage. However, this increase in velocity for positive polarity appears to be faster than that of negative polarity. At lower voltages, negative polarity produces air flow with a higher velocity than that of the positive one. With an increase in the applied voltage ($V_0 \geq 24$ kV), positive polarity begins to produce air flow with a higher velocity than that of negative polarity.

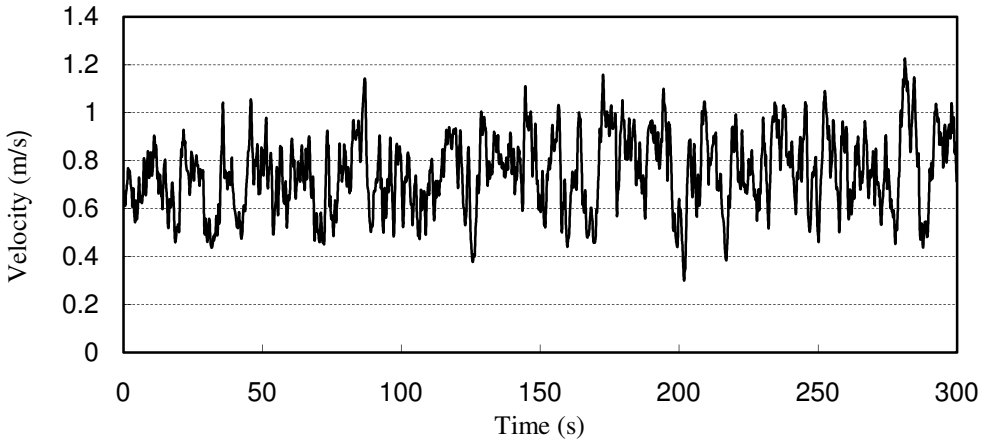

Figure 2.10 Variation of velocity with time (4 pins with negative polarity at 24 kV)

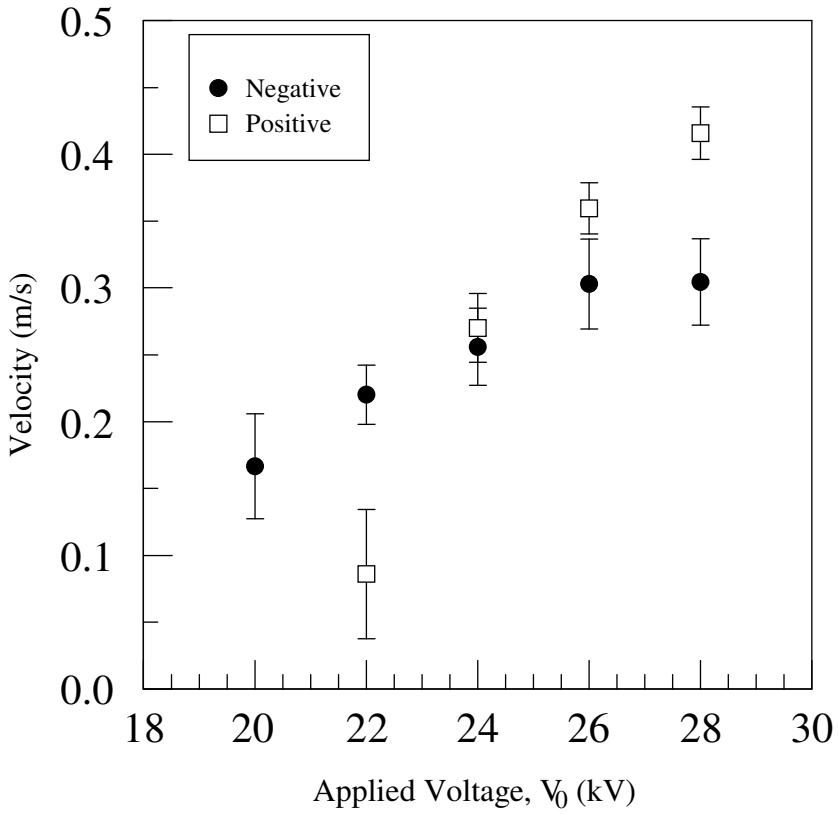

Figure 2.11 Average velocity vs. applied voltage (28 pins)

Therefore, the maximum velocity is higher for the case of positive corona discharge. This observation is consistent with previous findings by Chang, et al. [25]. For positive corona discharge, no velocity is detected below 20 kV because the electric field intensity is too weak to produce any effect.

Figure 2.12 depicts the velocity profile inside the channel with the configuration of 28 electrode pins under positive corona discharge. In this figure, the x- axis represents the channel width, so the locations of x = 0 in. and x = 4 in. refer to the channel walls. The velocity profile looks like an inverted parabola, which is the opposite of the fully

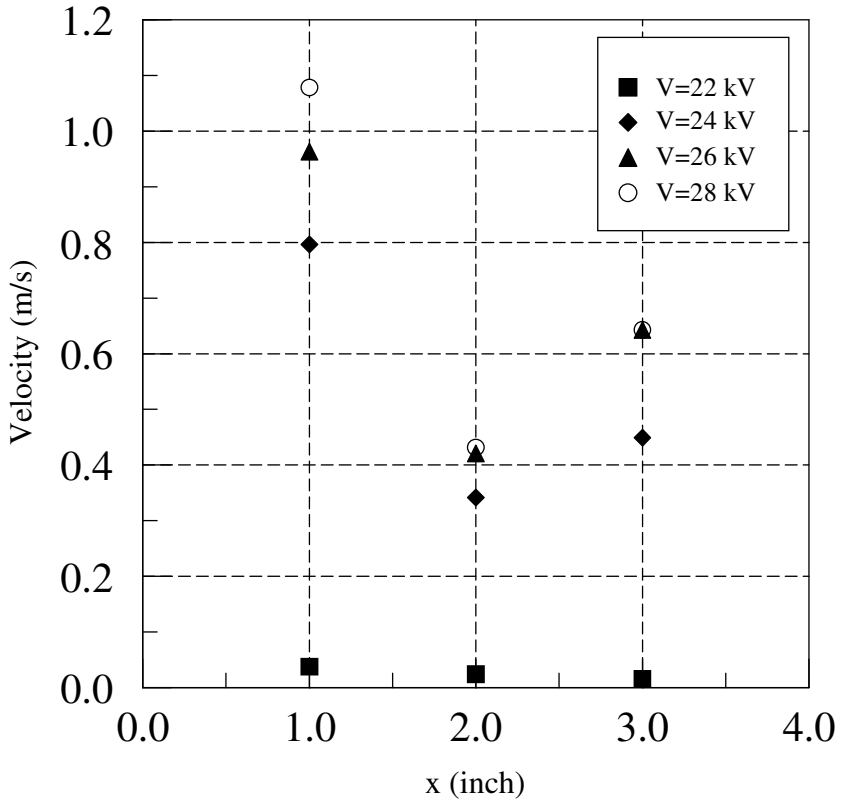

Figure 2.12 Velocity profile inside channel, 28 pins, positive polarity (z=4 in.)

developed velocity profile inside a channel. This is mainly due to the fact that the emitting electrode was embedded in the channel wall. The corona wind that it produced behaves like a wall jet, leading to the maximum air velocity occuring near the wall. This feature is more pronounced when the applied voltage reaches a certain value ($V_0 \geq 24$ kV). However, when the applied voltage is low ($V_0 = 22$ kV), the velocity profile is fairly uniform across the channel. Although one would anticipate that velocities at x = 1 in. and x = 3 in. would be the same because of symmetry, the velocity at x = 1 in. is actually higher. This asymmetric velocity profile may be caused by the presence of the velocity measuring probe, which blocks or modifies the flow. In addition, the induced airflow velocity increases with an increase in the applied voltage. The highest velocity measured in this configuration is as high as 1.08 m/s, which is within the typical range of a few meters per second for corona discharge [43]. These velocities are measured at the cross section z = 4 in. downstream from the grounded plate. The same features hold for other cross section levels (z = 1 in. and z = 2.5 in. in Appendix).

The average volume flow rate of air induced by the EHD pump is shown in Fig. 2.13 as a function of applied voltage. For all three configurations considered, the induced volume flow rate of air increases with an increase in the applied voltage. At lower voltages ($V_0 \leq 22$ kV for negative polarity; $V_0 \leq 24$ kV for positive polarity), the configuration with 4 electrode pins produces a higher volume flow rate than those with 12 or 28 pins. However, as the applied voltage increases, the configuration with 12 electrode pins produces the maximum volume flow rate of air. Thus, it is speculated that there may exist an optimal number of pins for an EHD pump to produce the maximum

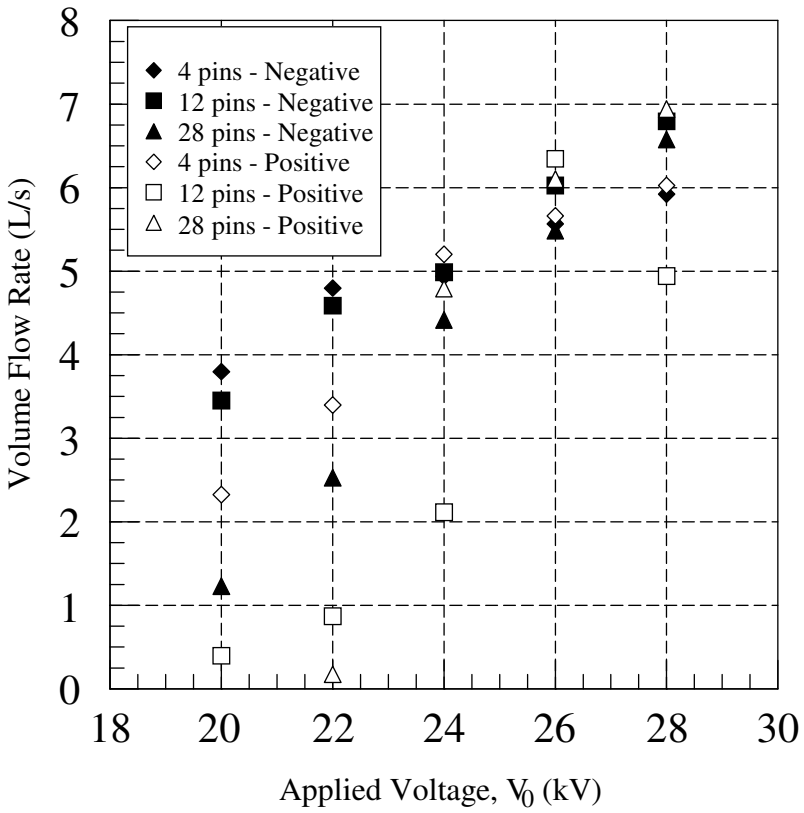

Figure 2.13 Average volume flow rate vs. applied voltage

volume flow rate of air at a given voltage. Also it is noticed that negative corona discharge produces a higher flow rate of air at a lower voltage than that of positive corona, whereas the opposite is true when the applied voltage increases ($V_0 \geq 24$ kV).

2.3.3 Performance Evaluation

To evaluate the performance of the EHD gas pump proposed against various conventional fans, an energy efficiency rating is employed, which is defined as the amount of air delivered per unit of the electric power used. The unit for this rating is usually CFM/W (cubic feet per minute per watt) or L/s/W (liters per second per watt).

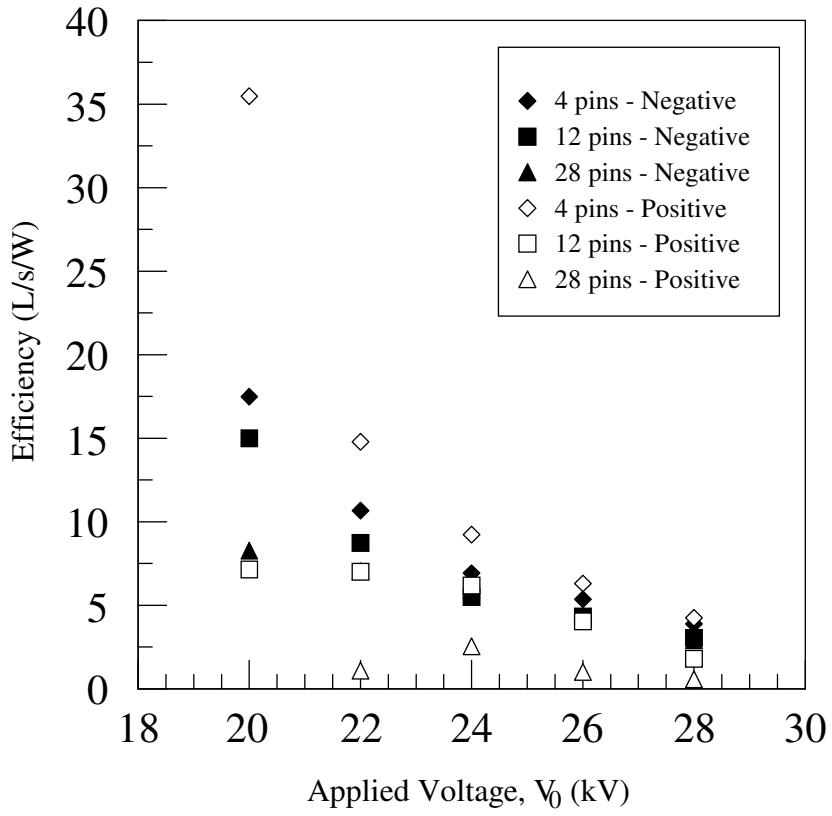

Figure 2.14 EHD gas pump performance as a function of applied voltage

Figure 2.14 shows the EHD gas pump performance as a function of the applied voltage for three electrode configurations operated at both positive and negative polarities. The gas pump has a maximum performance of 35 L/s/W for the configuration with 4 electrode pins operated at an applied voltage of 20 kV with positive corona discharge. The performance decreases sharply as the applied voltage increases. It is observed that the configuration with a fewer number of electrode pins has a higher efficiency rating. No definite conclusion can be drawn about the effect of polarity on the performance.

Table 2.1 Performance of conventional cooling fans for personal computer [44]

Pentium CPU fan	Fan Diameter (mm)	Performance (L/s/W)
Pentium II in desktop chassis	40	1.79
Pentium II & III in tower chassis	50	3.15
Pentium III in 1U server chassis	50	3.67
Pentium 4 in 1U server chassis	60	2.31

The performance of conventional computer cooling fans ranges from 1 to 4 L/s/W as shown in Table 1 [44], which is considered low when comparing with the data shown in Fig. 2.14. The EHD gas pump in the current study has a higher efficiency in energy use. In addition, with no moving parts, the EHD gas pump offers much quieter operation than the conventional fans.

2.4 Conclusions

The corona discharge phenomenon is investigated in a square channel with wire-electrodes without forced air flow or heat transfer. Experiments are conducted using an EHD gas pump with three electrode configurations (4 pins, 12 pins, and 28 pins) operated in either positive or negative DC voltage. Corona current in this experiment shows that a transient state exists before the current becomes steady. However, this transition period reduces as the applied voltage increases. Corona wind velocity fluctuates around an averaged value and this averaged velocity increases with an increase in the applied voltage. The velocity profile inside the channel reveals that the corona wind emitting from the electrodes accelerates the fluid flow near the wall, resulting in a reversed parabolic velocity profile. In terms of polarity, positive dischareg generally produces higher velocity than the negative one at a higher voltage. The maximum volume flow rate

of air induced by the EHD pump in the current experiment is as high as 7 liters per second for the configuration of 28 electrode pins with positive polarity.

Although present experiments are without forced air flow, the results provide important information and foundation for the subsequent numerical study when forced air flow and heat transfer are examined in a square channel with the EHD gas pump.

CHAPTER THREE

THEORETICAL BACKGROUND AND NUMERICAL FORMULATIONS

This chapter provides a theoretical foundation for the corona wind phenomenon. The interactions among electric fields, flow fields, and temperature fields will be discussed first. Governing equations for each field, upon which numerical calculations are based, will be presented in the following section.

3.1 Interactions among Electric, Flow and Temperature Fields

The electric body force, the main driving force behind corona-induced flow mixing and resulting heat transfer enhancement, is expressed as

$$\mathbf{f}_e = \rho_c \mathbf{E} - \frac{1}{2} E^2 \nabla \varepsilon + \frac{1}{2} \nabla \left[E^2 \rho \left(\frac{\partial \varepsilon}{\partial \rho} \right) \right]. \tag{3.1}$$

The first term, $\rho_c \mathbf{E}$, represents the Coulomb force acting on the charged particles. This is the force applied by the electric field on the electrons and ions that may exist in the fluid. The second term, $-(1/2) E^2 \nabla \varepsilon$, represents the force produced by the spatial change of electrical permittivity. The third term, $(1/2) \nabla \left[E^2 \rho (\partial \varepsilon / \partial \rho) \right]$, represents the force caused by the inhomogeneity of the electric field strength and is called electrostrictive force.

Many EHD applications use air as the working fluid. For corona discharge in air under atmospheric pressure and at room temperature, electric permittivity can be assumed

to be constant. The second and third terms on the right-hand side of equation (3.1) become negligible. In such cases, the electric body force is simply the Coulomb force.

No corona discharge occurs at low voltages, but when the applied voltage increases to a certain threshold value, ionization occurs at the nearby region of a needle or wire electrode. Ions, controlled by the Coulomb force, accelerate and migrate to the grounded plate. This migration causes collisions between charged particles and neutral molecules to produce a bulk of airflow, which is corona wind, but also creates an electric current, which is also called corona current or convective current.

Electric current is defined by

$$\mathbf{J} = \rho_c b\mathbf{E} + \rho_c \mathbf{u}, \tag{3.2}$$

where $\mathbf{u}$ is the bulk fluid velocity. The second term provides the coupling relation between flow field and electric field.

Typical interactions among the electric, flow, and temperature fields for corona discharge in air are shown in Fig. 3.1. Theoretically, the electric field and flow field interfere with each other. Corona wind produced by the electric field changes the flow pattern, and the fluid velocity in turn affects the electric field by changing the corona current. However, the ions travel at a speed which is generally several orders of magnitude larger than the speed of the bulk fluid. Therefore, the effect of the bulk flow on the electric field is negligible, which leads to the so-called one-way coupling assumption in numerical simulation. One-way coupling states that the electric field can

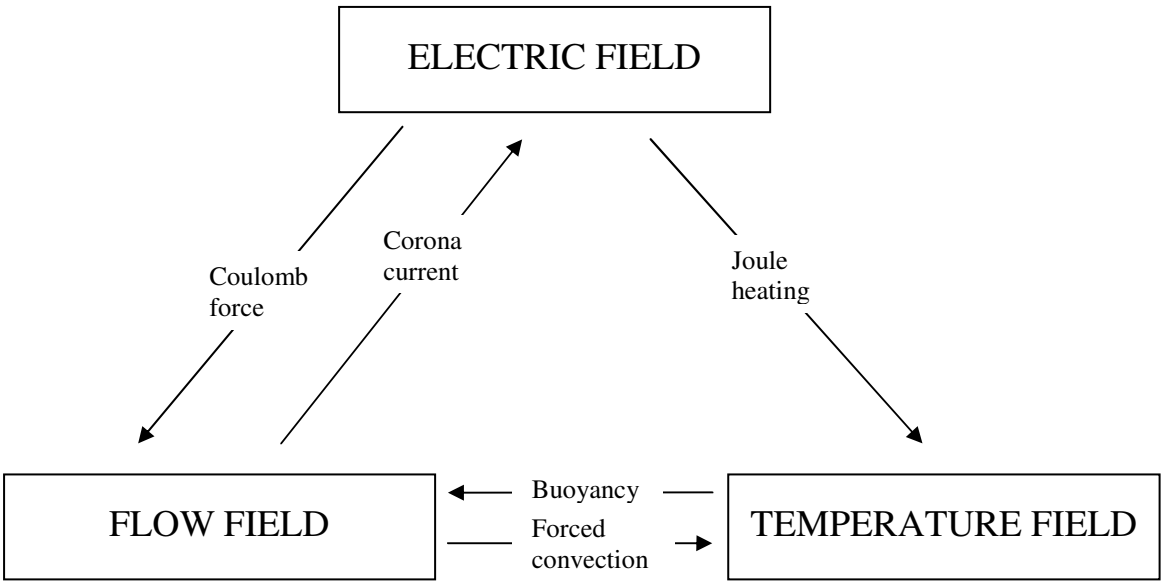

Figure 3.1 Interactions among electric, flow, and temperature fields

have influences on the flow field, but not vice versa. This assumption has been verified by Huang and Lai [45].

Both thermal buoyancy and Coulomb force affect the flow field. It has been shown that the flow field may become steady, periodic, or non-periodic depending on the flow Reynolds number due to the interaction between electric forces and flow inertia forces [36]. When the flow inertia is weak and the electric force is strong, the flow and temperature field become oscillatory. The addition of thermal buoyancy augments this instability [46-47].

Joule heating is released when current flows through wires and charged particles collide with ions or neutral molecules. For forced convection, the contribution to the heat transfer enhancement by Joule heating is negligible when compared to that by EHD flow convection alone. However, this is not the case for natural convection [48].

3.2 Governing Equations

In spite of complicated interactions between various fields, the electrohydrodynamic phenomenon is governed by the fundamental equations of electrostatics, fluid flow and heat transfer. For incompressible fluid with constant thermalphysical properties, the EHD governing equations for EHD-induced flows and heat transfer can be summarized as follows.

Maxwell equation:

$$\nabla \cdot \varepsilon \mathbf{E} = \rho_c. \tag{3.3}$$

Conservation of electric current:

$$\frac{\partial \rho_c}{\partial t} + \nabla \cdot \mathbf{J} = 0. \tag{3.4}$$

Continuity:

$$\nabla \cdot \mathbf{u} = 0. \tag{3.5}$$

Navier-Stokes equation:

$$\rho \frac{\partial \mathbf{u}}{\partial t} + \rho (\mathbf{u} \cdot \nabla) \mathbf{u} = -\nabla p + \mu \nabla^2 \mathbf{u} + \rho g + \mathbf{f}_e. \tag{3.6}$$

Energy equation:

$$\frac{\partial T}{\partial t} + (\mathbf{u} \cdot \nabla) T = \alpha \nabla^2 T. \tag{3.7}$$

As seen from the above equations, the complexity of the EHD phenomena is partly caused by the coupling of equations. One typical example of this is that the electric body force, f_e, is included as the external force in the Navier-Stokes equation of the flow field (Eq. 3.6), and at the same time, the fluid velocity, u, is involved in the electric

current (Eq. 3.2). However, appropriate assumptions can be made to simplify the equations for any particular application.

3.3 Numerical Formulations and Procedures - Governing Equations

For the present study, the working fluid is air under atmospheric pressure and room temperature. The following assumptions have been made in the development of numerical model.

1. The thermalphysical properties of air, which include density, viscosity, thermal conductivity, mobility, and permittivity are assumed constant.
2. The polarity of the generated ions is the same as the emitting electrode (unipolar charge condition).
3. The dominant electrical body force is Coulomb force while the force due to the gradient of the dielectric constant and the electrostrictive force are negligible.
4. The effect of a magnetic field, which is generated by the corona current, is negligible.
5. The coupling between the electric field and flow field is assumed one-way. In other words, the electric field affects the flow field, but not vice versa.
6. Joule heating is negligible.

With the above assumptions, the governing equations from the previous section can be simplified.

For the electric field with an electric field strength $\mathbf{E}$, defined as $\mathbf{E} = -\nabla V$, the Maxwell equation (Eq. 3.3) can be

$$\nabla^2 V = -\frac{\rho_c}{\varepsilon}. \tag{3.8}$$

The one-way coupling assumption gives $\mathbf{J} = \rho_c b\mathbf{E}$. Thus, for a steady DC power source, the conservation of electric current equation now becomes

$$\frac{\rho_c^2}{\varepsilon} + \nabla\rho_c \cdot \mathbf{E} = 0. \tag{3.9}$$

For the flow fields, with the electrical body force, $\mathbf{f}_e = \rho_c \mathbf{E}$, the Navier-Stokes equations become

$$\rho\frac{\partial \mathbf{u}}{\partial t} + \rho(\mathbf{u}\cdot\nabla)\mathbf{u} = -\nabla p + \mu\nabla^2\mathbf{u} + \rho_c\mathbf{E}. \tag{3.10}$$

For the temperature field, the energy equation remains the same,

$$\frac{\partial T}{\partial t} + (\mathbf{u}\cdot\nabla)T = \alpha\nabla^2 T. \tag{3.11}$$

A review of the above equations reveals that the electric field equations (3.8-3.9) are decoupled from the flow and temperature field equations (3.10-3.11) due to the one-way coupling assumption. However, the electric field needs to be solved first so that the electric body force can be included as the external body force in the momentum equation. Since energy equation is decoupled from the electric and flow fields, it can be solved separately once the flow filed is known.

3.3.1 Electric Field

In Cartesian coordinates, equations (3.8) and (3.9) can be rewritten to give

$$\frac{\partial^2 V}{\partial x^2}+\frac{\partial^2 V}{\partial y^2}+\frac{\partial^2 V}{\partial z^2}=-\frac{\rho_c}{\varepsilon}. \tag{3.12}$$

$$\frac{\rho_c^2}{\varepsilon}+\frac{\partial \rho_c}{\partial x}E_x+\frac{\partial \rho_c}{\partial y}E_y+\frac{\partial \rho_c}{\partial z}E_z=0. \tag{3.13}$$

The finite difference method is used to solve the above differential equations. A uniform mesh is employed for numerical calculations. A control volume of nodal P in a three-dimensional computational domain is shown in Fig. 3.2. Integrating equation (3.12) over the control volume yields

$$\int_{z,b}^{z,t}\int_{y,s}^{y,n}\int_{x,w}^{x,e}\left(\frac{\partial^2 V}{\partial x^2}+\frac{\partial^2 V}{\partial y^2}+\frac{\partial^2 V}{\partial z^2}\right)dxdydz=-\int_{z,b}^{z,t}\int_{y,s}^{y,n}\int_{x,w}^{x,e}\frac{\rho_c}{\varepsilon}dxdydz. \tag{3.14}$$

Integrate once, one obtains

$$\begin{aligned}\int_{z,b}^{z,t}\int_{y,s}^{y,n}\left[\left(\frac{\partial V}{\partial x}\right)_e-\left(\frac{\partial V}{\partial x}\right)_w\right]dydz+\int_{z,b}^{z,t}\int_{x,w}^{x,e}\left[\left(\frac{\partial V}{\partial y}\right)_n-\left(\frac{\partial V}{\partial y}\right)_s\right]dxdz\\ +\int_{y,s}^{y,n}\int_{x,w}^{x,e}\left[\left(\frac{\partial V}{\partial z}\right)_t-\left(\frac{\partial V}{\partial z}\right)_b\right]dxdy=-\int_{z,b}^{z,t}\int_{y,s}^{y,n}\int_{x,w}^{x,e}\frac{\rho_c}{\varepsilon}dxdydz.\end{aligned} \tag{3.15}$$

A central difference scheme is employed for the approximations of derivative terms. Then, equation (3.15) can be rewritten as

$$\begin{aligned}&\left(\frac{V_E-V_P}{x_E-x_P}-\frac{V_P-V_W}{x_P-x_W}\right)(y_n-y_s)(z_t-z_b)\\ &+\left(\frac{V_N-V_P}{y_N-y_P}-\frac{V_P-V_S}{y_P-y_S}\right)(x_e-x_w)(z_t-z_b)\\ &+\left(\frac{V_T-V_P}{z_T-z_P}-\frac{V_P-V_B}{z_P-z_B}\right)(y_n-y_s)(x_e-x_w)=-\frac{\rho_c}{\varepsilon}(x_e-x_w)(y_n-y_s)(z_t-z_b).\end{aligned} \tag{3.16}$$

For a uniform mesh, $\Delta x=\Delta y=\Delta z=\Delta$, equation (3.16) can be further simplified to give

$$\left(\frac{V_E - V_P}{\Delta} - \frac{V_P - V_W}{\Delta}\right) + \left(\frac{V_N - V_P}{\Delta} - \frac{V_P - V_S}{\Delta}\right) + \left(\frac{V_T - V_P}{\Delta} - \frac{V_P - V_B}{\Delta}\right) = -\frac{\rho_c}{\varepsilon}\Delta. \tag{3.17}$$

Multiplying equation (3.17) by Δ and combining like terms yields

$$-6V_P + V_E + V_W + V_N + V_S + V_T + V_B = -\frac{\rho_c}{\varepsilon}\Delta^2. \tag{3.18}$$

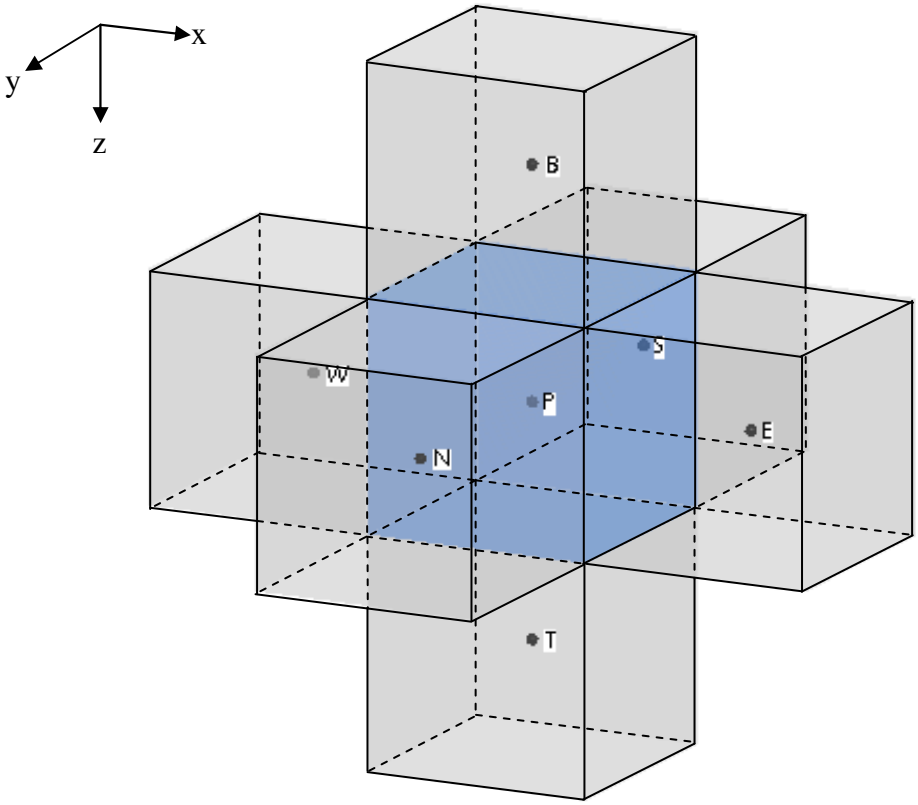

Figure 3.2 Control volume of nodal P in a three-dimensional computational domain

The final finite difference form for equation (3.12) becomes

$$V_P = \frac{1}{6}\left(V_E + V_W + V_N + V_S + V_T + V_B + \frac{\rho_c}{\varepsilon}\Delta^2 \right). \tag{3.19}$$

Similarly, the finite difference form of the current continuity equation can be derived by integrating the partial differential equation over a control volume, which gives

$$\begin{aligned} &\int_{z,b}^{z,t}\int_{y,s}^{y,n}\int_{x,w}^{x,e}\frac{\rho_c^2}{\varepsilon}dxdydz + \int_{z,b}^{z,t}\int_{y,s}^{y,n}\int_{x,w}^{x,e}\frac{\partial\rho_c}{\partial x}E_x dxdydz \\ &+\int_{z,b}^{z,t}\int_{y,s}^{y,n}\int_{x,w}^{x,e}\frac{\partial\rho_c}{\partial y}E_y dxdydz + \int_{z,b}^{z,t}\int_{y,s}^{y,n}\int_{x,w}^{x,e}\frac{\partial\rho_c}{\partial z}E_z dxdydz = 0. \end{aligned} \tag{3.20}$$

Carrying out the integrations, one obtains

$$\begin{aligned} &\frac{\rho_c^2}{\varepsilon}\Delta x\Delta y\Delta z + (\rho_{ce} - \rho_{cw})E_x\Delta y\Delta z \\ &+(\rho_{cn} - \rho_{cs})E_y\Delta x\Delta z + (\rho_{ct} - \rho_{cb})E_z\Delta x\Delta y = 0. \end{aligned} \tag{3.21}$$

With a uniform mesh, $\Delta x = \Delta y = \Delta z = \Delta$, the above equation can be simplified to give

$$\frac{\rho_c^2}{\varepsilon}\Delta + (\rho_{ce} - \rho_{cw})(E_x) + (\rho_{cn} - \rho_{cs})(E_y) + (\rho_{ct} - \rho_{cb})(E_z) = 0. \tag{3.22}$$

A backward difference scheme is applied for the charge density terms to eliminate the numerical instability which may occur. Thus, equation (3.22) can be reformulated by taking into account eight possible scenarios.

(1) $E_x \geq 0,\ E_y \geq 0,\ E_z \geq 0$

$$\frac{\Delta}{\varepsilon}\rho_{cP}^2 + E_x(\rho_{cP} - \rho_{cW}) + E_y(\rho_{cP} - \rho_{cS}) + E_z(\rho_{cP} - \rho_{cB}) = 0,$$

which can be rearranged to give

$$\frac{\Delta}{\varepsilon}\rho_{cP}^2+\left(E_x+E_y+E_z\right)\rho_{cP}+\left(-E_x\rho_{cW}-E_y\rho_{cS}-E_z\rho_{cB}\right)=0. \tag{3.23a}$$

(2) $E_x \le 0,\ E_y \ge 0,\ E_z \ge 0$

$$\frac{\Delta}{\varepsilon}\rho_{cP}^2+E_x\left(\rho_{cE}-\rho_{cP}\right)+E_y\left(\rho_{cP}-\rho_{cS}\right)+E_z\left(\rho_{cP}-\rho_{cB}\right)=0,$$

which can be rearranged to give

$$\frac{\Delta}{\varepsilon}\rho_{cP}^2+\left(-E_x+E_y+E_z\right)\rho_{cP}+\left(E_x\rho_{cE}-E_y\rho_{cS}-E_z\rho_{cB}\right)=0. \tag{3.23b}$$

(3) $E_x \ge 0,\ E_y \le 0,\ E_z \ge 0$

$$\frac{\Delta}{\varepsilon}\rho_{cP}^2+E_x\left(\rho_{cP}-\rho_{cW}\right)+E_y\left(\rho_{cN}-\rho_{cP}\right)+E_z\left(\rho_{cP}-\rho_{cB}\right)=0,$$

which can be rearranged to give

$$\frac{\Delta}{\varepsilon}\rho_{cP}^2+\left(E_x-E_y+E_z\right)\rho_{cP}+\left(-E_x\rho_{cW}+E_y\rho_{cN}-E_z\rho_{cB}\right)=0. \tag{3.23c}$$

(4) $E_x \ge 0,\ E_y \ge 0,\ E_z \le 0$

$$\frac{\Delta}{\varepsilon}\rho_{cP}^2+E_x\left(\rho_{cP}-\rho_{cW}\right)+E_y\left(\rho_{cP}-\rho_{cS}\right)+E_z\left(\rho_{cT}-\rho_{cP}\right)=0,$$

which can be rearranged to give

$$\frac{\Delta}{\varepsilon}\rho_{cP}^2+\left(E_x+E_y-E_z\right)\rho_{cP}+\left(-E_x\rho_{cW}-E_y\rho_{cS}+E_z\rho_{cT}\right)=0. \tag{3.23d}$$

(5) $E_x \le 0,\ E_y \le 0,\ E_z \ge 0$

$$\frac{\Delta}{\varepsilon}\rho_{cP}^2+E_x\left(\rho_{cE}-\rho_{cP}\right)+E_y\left(\rho_{cN}-\rho_{cP}\right)+E_z\left(\rho_{cP}-\rho_{cB}\right)=0,$$

which can be rearranged to give

$$\frac{\Delta}{\varepsilon}\rho_{cP}^2+\left(-E_x-E_y+E_z\right)\rho_{cP}+\left(E_x\rho_{cE}+E_y\rho_{cN}-E_z\rho_{cB}\right)=0. \tag{3.23e}$$

(6) $E_x \geq 0,\ E_y \leq 0,\ E_z \leq 0$

$$\frac{\Delta}{\varepsilon}\rho_{cP}^2+E_x\left(\rho_{cP}-\rho_{cW}\right)+E_y\left(\rho_{cN}-\rho_{cP}\right)+E_z\left(\rho_{cT}-\rho_{cP}\right)=0,$$

which can be rearranged to give

$$\frac{\Delta}{\varepsilon}\rho_{cP}^2+\left(E_x-E_y-E_z\right)\rho_{cP}+\left(-E_x\rho_{cW}+E_y\rho_{cN}+E_z\rho_{cT}\right)=0. \tag{3.23f}$$

(7) $E_x \leq 0,\ E_y \geq 0,\ E_z \leq 0$

$$\frac{\Delta}{\varepsilon}\rho_{cP}^2+E_x\left(\rho_{cE}-\rho_{cP}\right)+E_y\left(\rho_{cP}-\rho_{cS}\right)+E_z\left(\rho_{cT}-\rho_{cP}\right)=0,$$

which can be rearranged to give

$$\frac{\Delta}{\varepsilon}\rho_{cP}^2+\left(-E_x+E_y-E_z\right)\rho_{cP}+\left(E_x\rho_{cE}-E_y\rho_{cS}+E_z\rho_{cT}\right)=0. \tag{3.23g}$$

(8) $E_x \leq 0,\ E_y \leq 0,\ E_z \leq 0$

$$\frac{\Delta}{\varepsilon}\rho_{cP}^2+E_x\left(\rho_{cE}-\rho_{cP}\right)+E_y\left(\rho_{cN}-\rho_{cP}\right)+E_z\left(\rho_{cT}-\rho_{cP}\right)=0,$$

which can be rearranged to give

$$\frac{\Delta}{\varepsilon}\rho_{cP}^2+\left(-E_x-E_y-E_z\right)\rho_{cP}+\left(E_x\rho_{cE}+E_y\rho_{cN}+E_z\rho_{cT}\right)=0. \tag{3.23h}$$

Finally, the quadratic formula is used to solve the charge density (ρ_{cP}) in the above equations, $\rho_{cP} = \dfrac{-b \pm \sqrt{b^2 - 4ac}}{2a}$.

Equations (3.12) and (3.13) must be solved simultaneously to determine the electric potential and space charge density distribution. A numerical procedure proposed by Yamamoto and Velkoff [13] is employed for the present calculations. In this procedure, the electric potential is first estimated by solving equation (3.12) without space charge density (i.e., in the form of Laplace equation). Since the space charge density distribution is not known a priori, an assumed value of space charge density at the wire tip is needed to solve the equation (3.13). After the calculation of the space charge density distribution, equation (3.12) is re-calculated with the space charge density obtained (i.e., in the form of Poisson equation). Then, the total current at the grounded plate is calculated using equation (3.24) and compared with the experimental data. If they are different, a new value of space charge density at the wire tip is assumed and the calculation is repeated until the calculated total current agrees well with the measured value for that given applied voltage. The flow chart of this numerical procedure is illustrated in Fig. 3.3.

The corona current is related to the space charge density via

$$I = \int_A \rho_c b \nabla V \cdot dA, \tag{3.24}$$

where A represents the surface area of the grounded plate and b is the ion mobility.

The convergence criterion for electric field calculations is $\left|\frac{I_{cal} - I_{exp}}{I_{exp}}\right| \leq 10^{-3}$.

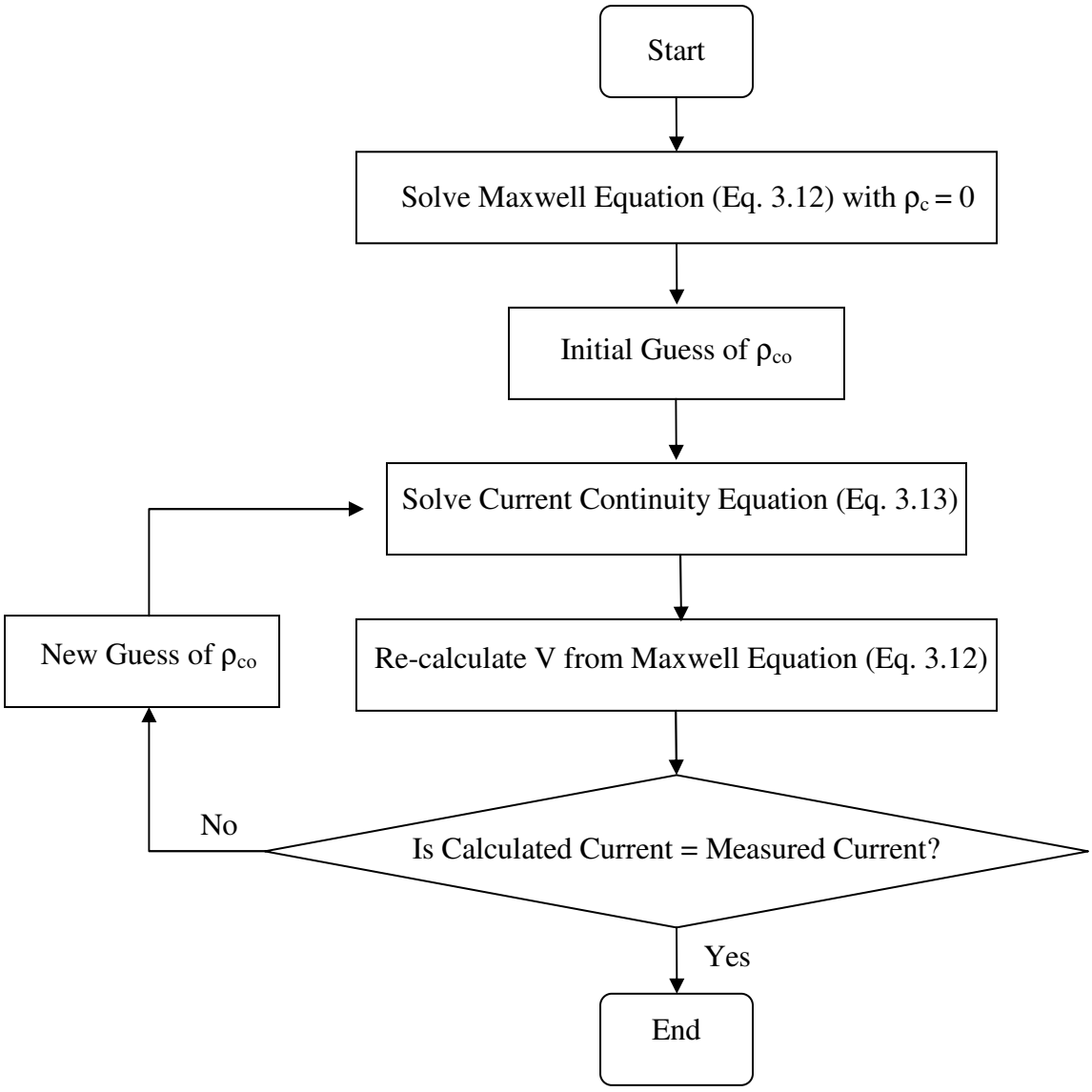

Figure 3.3 Flow chart of the numerical procedure for electric field

3.3.2 Flow and Temperature Fields

In Cartesian coordinates, the continuity, momentum, and energy equations for three-dimensional, steady, incompressible, laminar flows in a channel with constant properties are shown below in equations (3.25), (3.26-28), and (3.29), respectively.

$$\frac{\partial u}{\partial x}+\frac{\partial v}{\partial y}+\frac{\partial w}{\partial z}=0, \tag{3.25}$$

$$u\frac{\partial u}{\partial x}+v\frac{\partial u}{\partial y}+w\frac{\partial u}{\partial z}=-\frac{1}{\rho}\frac{\partial p}{\partial x}+\nu\left(\frac{\partial^2 u}{\partial x^2}+\frac{\partial^2 u}{\partial y^2}+\frac{\partial^2 u}{\partial z^2}\right)+\frac{\rho_c}{\rho}E_x, \tag{3.26}$$

$$u\frac{\partial v}{\partial x}+v\frac{\partial v}{\partial y}+w\frac{\partial v}{\partial z}=-\frac{1}{\rho}\frac{\partial p}{\partial y}+\nu\left(\frac{\partial^2 v}{\partial x^2}+\frac{\partial^2 v}{\partial y^2}+\frac{\partial^2 v}{\partial z^2}\right)+\frac{\rho_c}{\rho}E_y, \tag{3.27}$$

$$u\frac{\partial w}{\partial x}+v\frac{\partial w}{\partial y}+w\frac{\partial w}{\partial z}=-\frac{1}{\rho}\frac{\partial p}{\partial z}+\nu\left(\frac{\partial^2 w}{\partial x^2}+\frac{\partial^2 w}{\partial y^2}+\frac{\partial^2 w}{\partial z^2}\right)+\frac{\rho_c}{\rho}E_z, \tag{3.28}$$

$$u\frac{\partial T}{\partial x}+v\frac{\partial T}{\partial y}+w\frac{\partial T}{\partial z}=\alpha\left(\frac{\partial^2 T}{\partial x^2}+\frac{\partial^2 T}{\partial y^2}+\frac{\partial^2 T}{\partial z^2}\right). \tag{3.29}$$

The last terms in momentum equations (3.26-3.28) are the electric body forces, which can be calculated once the electric potential and charge density distribution are known. The above equations can be non-dimensionalized by introducing the following parameters,

$$\bar{x}=\frac{x}{D}, \qquad \bar{y}=\frac{y}{D}, \qquad \bar{z}=\frac{z}{D},$$

$$\bar{u}=\frac{u}{u_i}, \qquad \bar{v}=\frac{v}{u_i}, \qquad \bar{w}=\frac{w}{u_i}, \qquad \bar{p}=\frac{p-p_i}{\rho u_i^2}, \qquad Re=\frac{u_i D}{\nu},$$

$$u_e = \sqrt{\frac{\rho_{c0} V_0}{\rho}}, \quad \bar{\rho}_c = \frac{\rho_c}{\rho_{c0}}, \quad \bar{V} = \frac{V}{V_0}, \quad \theta = \frac{T - T_w}{T_i - T_w}, \quad P_r = \frac{\nu}{\alpha}, \quad (3.30)$$

where D is the hydraulic diameter, which is the width of the square channel in the current study. Also, u_i is the flow velocity at the inlet, and u_e is the characteristic corona wind velocity. With the above dimensionless parameters, the momentum and energy equations can be reformulated as shown below.

Continuity:

$$\frac{\partial \bar{u}}{\partial \bar{x}} + \frac{\partial \bar{v}}{\partial \bar{y}} + \frac{\partial \bar{w}}{\partial \bar{z}} = 0, \quad (3.31)$$

Momentum:

$$\bar{u}\frac{\partial \bar{u}}{\partial \bar{x}} + \bar{v}\frac{\partial \bar{u}}{\partial \bar{y}} + \bar{w}\frac{\partial \bar{u}}{\partial \bar{z}} = -\frac{\partial \bar{p}}{\partial \bar{x}} + \frac{1}{Re}\left(\frac{\partial^2 \bar{u}}{\partial \bar{x}^2} + \frac{\partial^2 \bar{u}}{\partial \bar{y}^2} + \frac{\partial^2 \bar{u}}{\partial \bar{z}^2}\right) + \frac{u_e^2}{u_i^2}\bar{\rho}_c\left(\frac{\partial \bar{V}}{\partial \bar{x}}\right), \quad (3.32)$$

$$\bar{u}\frac{\partial \bar{v}}{\partial \bar{x}} + \bar{v}\frac{\partial \bar{v}}{\partial \bar{y}} + \bar{w}\frac{\partial \bar{v}}{\partial \bar{z}} = -\frac{\partial \bar{p}}{\partial \bar{y}} + \frac{1}{Re}\left(\frac{\partial^2 \bar{v}}{\partial \bar{x}^2} + \frac{\partial^2 \bar{v}}{\partial \bar{y}^2} + \frac{\partial^2 \bar{v}}{\partial \bar{z}^2}\right) + \frac{u_e^2}{u_i^2}\bar{\rho}_c\left(\frac{\partial \bar{V}}{\partial \bar{y}}\right), \quad (3.33)$$

$$\bar{u}\frac{\partial \bar{w}}{\partial \bar{x}} + \bar{v}\frac{\partial \bar{w}}{\partial \bar{y}} + \bar{w}\frac{\partial \bar{w}}{\partial \bar{z}} = -\frac{\partial \bar{p}}{\partial \bar{z}} + \frac{1}{Re}\left(\frac{\partial^2 \bar{w}}{\partial \bar{x}^2} + \frac{\partial^2 \bar{w}}{\partial \bar{y}^2} + \frac{\partial^2 \bar{w}}{\partial \bar{z}^2}\right) + \frac{u_e^2}{u_i^2}\bar{\rho}_c\left(\frac{\partial \bar{V}}{\partial \bar{z}}\right), \quad (3.34)$$

Energy:

$$\bar{u}\frac{\partial \theta}{\partial \bar{x}} + \bar{v}\frac{\partial \theta}{\partial \bar{y}} + \bar{w}\frac{\partial \theta}{\partial \bar{z}} = \frac{1}{Pr\,Re}\left(\frac{\partial^2 \theta}{\partial \bar{x}^2} + \frac{\partial^2 \theta}{\partial \bar{y}^2} + \frac{\partial^2 \theta}{\partial \bar{z}^2}\right). \quad (3.35)$$

Finite difference method is used to solve the above equations. The computational domain is divided into discrete control volumes, and the discretized equations are derived by integrating the differential equations over a control volume. Each control volume is associated with a nodal point at the center where the dependent variables such as velocity, pressure, and temperature are to be calculated. However, there are unknown values on the surfaces of the control volume which are required for the calculation of convective terms in the discrete equations. These face-values can be either interpolated from the values at the centers of the neighboring control volumes or be assigned according to some special numerical scheme. An upwind scheme has been frequently used to ensure the stability of numerical calculations for many studies reported in the literature. In this scheme, the unknown face-values of a control volume take the values of the cell upstream, or upwind, relative to the direction of normal velocity [49]. For the current study, this up wind scheme is also employed to discretize the convective terms in the momentum and energy equations.

One of the challenges in solving momentum equations is dealing with the pressure gradient terms. As observed from the set of equations (3.32-3.34), the velocities cannot be solved until the pressure field is specified. If the pressure field were specified differently, it would lead to different solutions of the velocity fields for the momentum equations. The constraint that uniquely determines the pressure field is the continuity equation. One must have the correct pressure field while solving the momentum equations so that the resulting velocity field will satisfy the continuity equation. However, the pressure gradient terms cannot be explicitly expressed in terms of velocities. Therefore, an algorithm is needed for solving the flow field.

Pressure-velocity coupling is achieved by applying the SIMPLE algorithm [42], which stands for Semi-Implicit Method for Pressure-Linked Equations. In this algorithm, the momentum equations are initially solved using an estimated pressure field, p^*. In general, the resulting velocity field will not satisfy the continuity equation. Consequently, a pressure correction p' needs to be obtained by solving the so-called pressure-correction equation so that the resulting pressure ($p = p^* + p'$) can be used to solve for velocities. This process is repeated until the velocity components satisfy the continuity equation. This SIMPLE algorithm is proposed by Patankar and a more detailed description can be found in reference [49].

The diffusion terms in the momentum and energy equation are discretized by using a second-order central difference scheme. The convergence criteria for the continuity, momentum, and energy equations are that the residuals are reduced to 10^{-4}, 10^{-3}, and 10^{-6}, respectively.

Calculations of the flow and temperature fields are performed by using the commercial code Fluent 6.3.26 [43]. The Pressure-based segregated algorithm is used to solve equations (3.32-3.25). This algorithm requires that the governing equations be solved sequentially (i.e., segregated from one another), in other words, the individual governing equations for the variables (e.g., $\bar{u}$, $\bar{v}$, $\bar{w}$, $\bar{p}$, and $\bar{T}$) are solved one after another. Each governing equation, while being solved is "decoupled" or "segregated" from other equations, hence its name [50]. The procedure of this algorithm is outlined in Fig. 3.4. The segregated algorithm is memory-efficient since the discretized equations

need only be stored in the memory one at a time. However, the solution convergence is relatively slow, because the equations are solved in a decoupled manner.

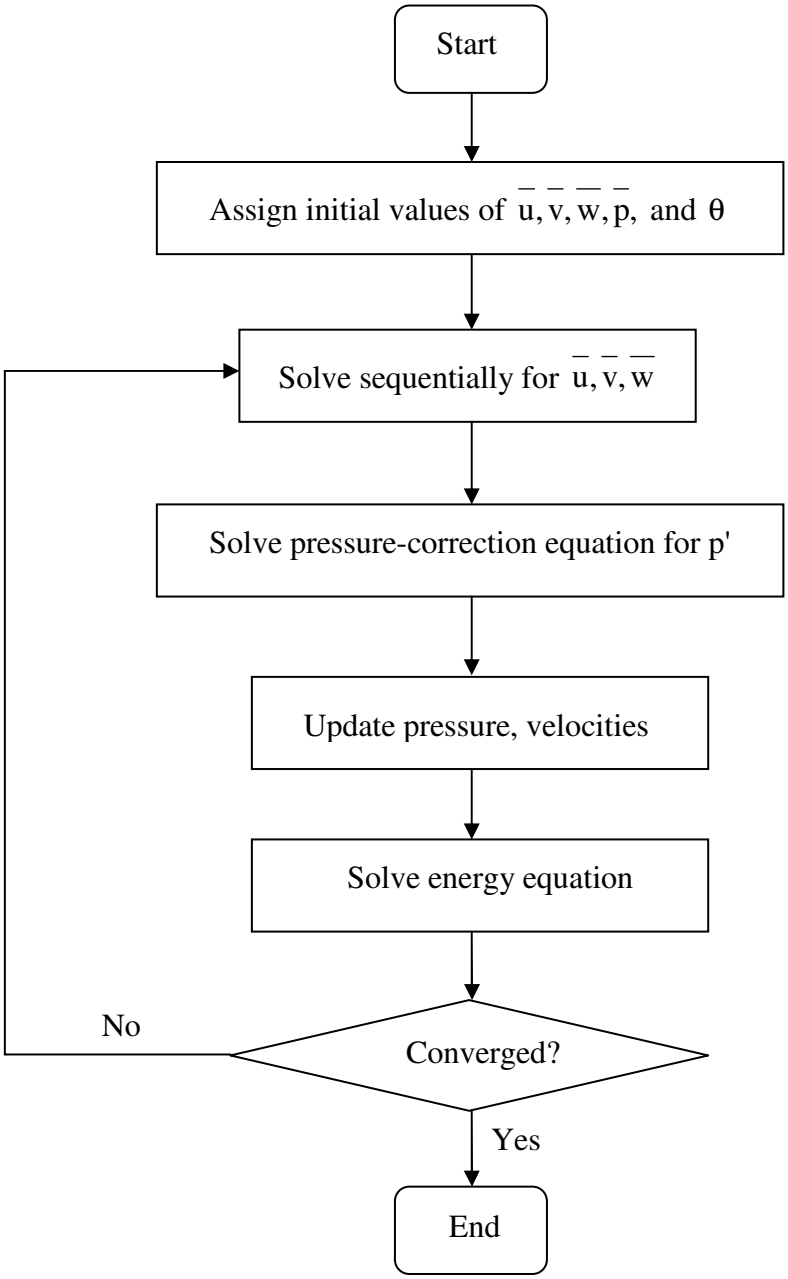

Figure 3.4 Flow chart for pressure-based segregated algorithm

3.4 Numerical Formulations and Procedures - Boundary Conditions

Solutions to the governing equations for the electric, flow, and temperature fields must be obtained subject to the existing boundary or initial conditions. A numerical model of an EHD gas pump with 12 electrode pins is shown in Fig. 3.5. To reduce the computational time, only a quarter of the model is considered as the computational domain, which is shown as the shaded region.

Boundary conditions for solving the electric potential are

At the wire electrodes, $V = V_0$. (3.36a)

At the grounded plate, $V = 0$. (3.36b)

On the channel walls, $x = 0$, $\frac{\partial V}{\partial x} = 0$. (3.36c)

$y = 0$, $\frac{\partial V}{\partial y} = 0$. (3.36d)

On the symmetric planes, $x = D/2$, $\frac{\partial V}{\partial x} = 0$. (3.36e)

$y = D/2$, $\frac{\partial V}{\partial y} = 0$. (3.36f)

At the inlet of the channel, $z = 0$, $\frac{\partial V}{\partial z} = 0$. (3.36g)

At the outlet of the channel, $z = H$, $\frac{\partial V}{\partial z} = 0$. (3.36h)

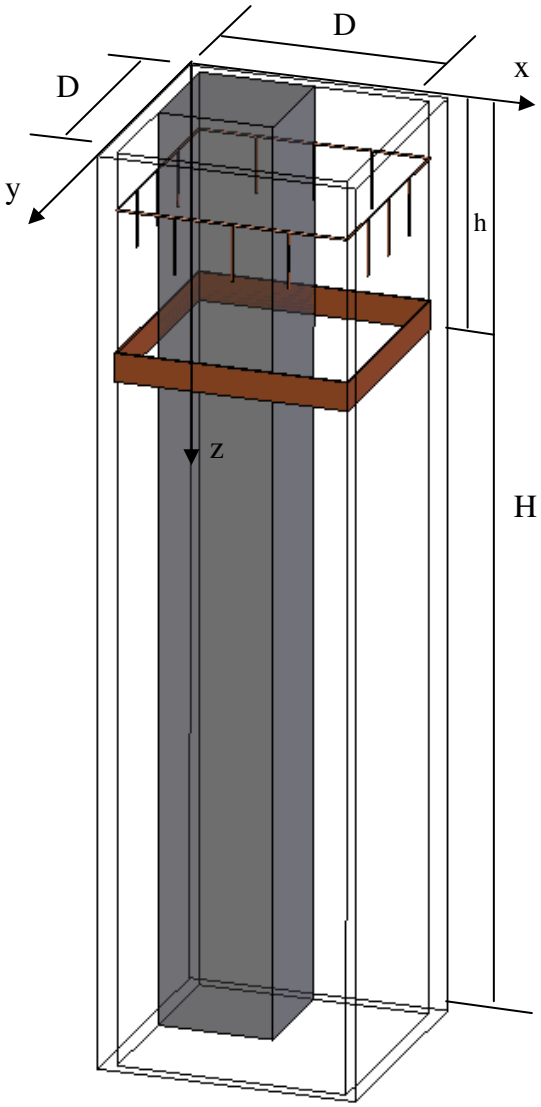

Figure 3.5 An EHD gas pump in a square channel and its computational domain

The boundary conditions for solving the momentum equations in dimensionless form are shown below.

On the channel walls: $\bar{x} = 0, \quad \bar{u} = 0, \quad \bar{v} = 0, \quad \bar{w} = 0,$ (3.37a)

$\bar{y} = 0, \quad \bar{u} = 0, \quad \bar{v} = 0, \quad \bar{w} = 0,$ (3.37b)

On the symmetric planes: $\bar{x} = D/2, \quad \bar{u} = 0, \quad \frac{\partial \bar{v}}{\partial \bar{x}} = 0, \quad \frac{\partial \bar{w}}{\partial \bar{x}} = 0,$ (3.37c)

$\bar{y} = D/2, \quad \frac{\partial \bar{u}}{\partial \bar{y}} = 0, \quad \bar{v} = 0, \quad \frac{\partial \bar{w}}{\partial \bar{y}} = 0,$ (3.37d)

At the inlet of the channel: $\bar{z} = 0, \quad \bar{u} = 1, \quad \bar{v} = 0, \quad \bar{w} = 0, \quad \bar{p} = 0.$ (3.37e)

At the outlet of the channel: $\bar{z} = H/D, \quad \frac{\partial \bar{u}}{\partial \bar{z}} = 0, \quad \frac{\partial \bar{v}}{\partial \bar{z}} = 0, \quad \frac{\partial \bar{w}}{\partial \bar{z}} = 0, \quad \bar{p} = \frac{p_{atm} - p_i}{\rho u_i^2}.$ (3.37f)

The boundary conditions for solving the energy equation in dimensionless form are shown below.

On the channel walls: $\bar{x} = 0 \text{ and } \bar{z} \le h / D, \quad \frac{\partial \theta}{\partial \bar{x}} = 0.$ (3.38a)

$\bar{x} = 0 \text{ and } \bar{z} \ge h / D, \quad \theta = 0.$ (3.38b)

$\bar{y} = 0 \text{ and } \bar{z} \le h / D, \quad \frac{\partial \theta}{\partial \bar{y}} = 0.$ (3.38c)

$$\bar{y} = 0 \text{ and } \bar{z} \geq h / D, \qquad \theta = 0. \tag{3.38d}$$

On the symmetric planes: $\bar{x} = D/2, \qquad \frac{\partial \theta}{\partial \bar{x}} = 0. \tag{3.38e}$

$$\bar{y} = D/2, \qquad \frac{\partial \theta}{\partial \bar{y}} = 0. \tag{3.38f}$$

At the inlet of the channel: $\bar{z} = 0, \qquad \theta = 1. \tag{3.38g}$

At the outlet of the channel: $\bar{z} = H/D, \qquad \frac{\partial \theta}{\partial \bar{z}} = 0. \tag{3.38h}$

The governing equations are solved using the above boundary conditions. A code written in Fortran 90 is used for solving the electric potential and the space charge density while the commercial code Fluent 6.3.26 is used for solving the flow and temperature fields. After the electric field becomes available, the electric body force is calculated and added the Fluent solver through a User-Defined Function (UDF), which is written in C programming language.

The model of the EHD gas pump shown in Fig. 3.5 has dimensions of 4 by 4 by 16 inches. However, for the electric field calculations, due to the fact that the electric field does not change further downstream of the grounded plate, a channel length of 7 inches is sufficient. A uniform grid of 51 x 51 x 251 has been used for the electric field computational domain of 2 by 2 by 10 inches. A non-uniform grid is used for calculating the flow and temperature fields, as shown in Fig. 3.6. Finer meshes are applied to the boundary layer region where the viscous and electric body forces dominate. Relatively

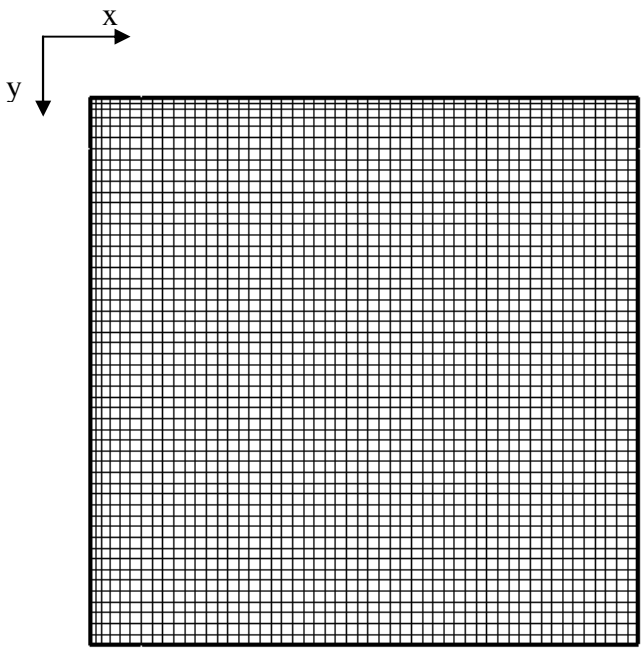

Figure 3.6 Cross-sectional view of computational grid in the x-y plane

coarse meshes are used in the regions far away from the boundary layer and far downstream. A total of 676,000 cells have been used in the computational domain of 2 by 2 by 16 inches. Further refinements of the mesh do not appear to produce more accurate results, but merely increase the computational time significantly.

Calculations are performed on a 64-bit workstation with a 2 GHz CPU and 8 Gb of RAM. A typical run takes about seven hours of CPU time for the solution of the electric field. However, the time required to solve for the flow and temperature field ranges from three hours to six hours, depending on the flow condition (i.e., the Reynolds number). In general, it takes more time for the solutions involving low Reynolds numbers than those with high Reynolds numbers.

CHAPTER FOUR

RESULTS AND DISCUSSIONS

Numerical simulations have been performed for the EHD gas pump with three electrode configurations: 4 electrode pins, 12 electrode pins, and 28 electrode pins. Positive corona discharge is considered for numerical study. Electric field results are presented first, followed by the flow and temperature fields.

4.1 Electric Field

The electric potential distributions inside the channel are shown in Fig. 4.1 for an EHD gas pump with 4 electrode pins, 12 electrode pins, and 28 electrode pins at an applied voltage of 24 kV. The potentials displayed in the figure are normalized with the voltage applied at the wire. It is observed that large potential gradients occur between the wire electrodes and the grounded plate. Below the grounded plate, voltage does not vary significantly. Hence, it is justifiable to use a shorter channel length for the electric field calculations. From Fig. 4.1, one can see that the electrode pins modify the electric field which would otherwise be uniformly stratified. This non-uniform electric field is an essential condition for the generation of corona wind. Therefore, it is important to include electrode pins to create corona wind in the square channel.

Figure 4.2 illustrates the electric potential contours at various cross-sections along the z direction for three electrode configurations considered at an applied voltage of 24 kV. On the cross-section at the wire-loop level ($\bar{z} = 1/4$), the contour lines of electric potentials are nearly concentric for all configurations. This concentric pattern is disrupted

by the presence of electrode pins. The influence by the electrode pins can be clearly seen from the cross-section at the electrode tip level ($\bar{z} = 1/2$). As the number of pins increases, the radius of influence from each pin decreases. It is also noticed that at this level, the configuration with 4 electrode pins has the lowest potential gradient. The disturbance by the presence of electrode pins is still clearly visible at the level midway between the electrode tips and the grounded plate ($\bar{z} = 11/16$) for the configuration with four electrode pins. However, for the configuration with 28 electrode pins, the electric potential becomes completely uniform at this level. As such, no contour line is observed. As one approaches the grounded plate, the electric potential distributions become concentric again as seen from the cross-sections at the levels which align with the top ($\bar{z} = 7/8$) and bottom edges ($\bar{z} = 1$) of the grounded plate.

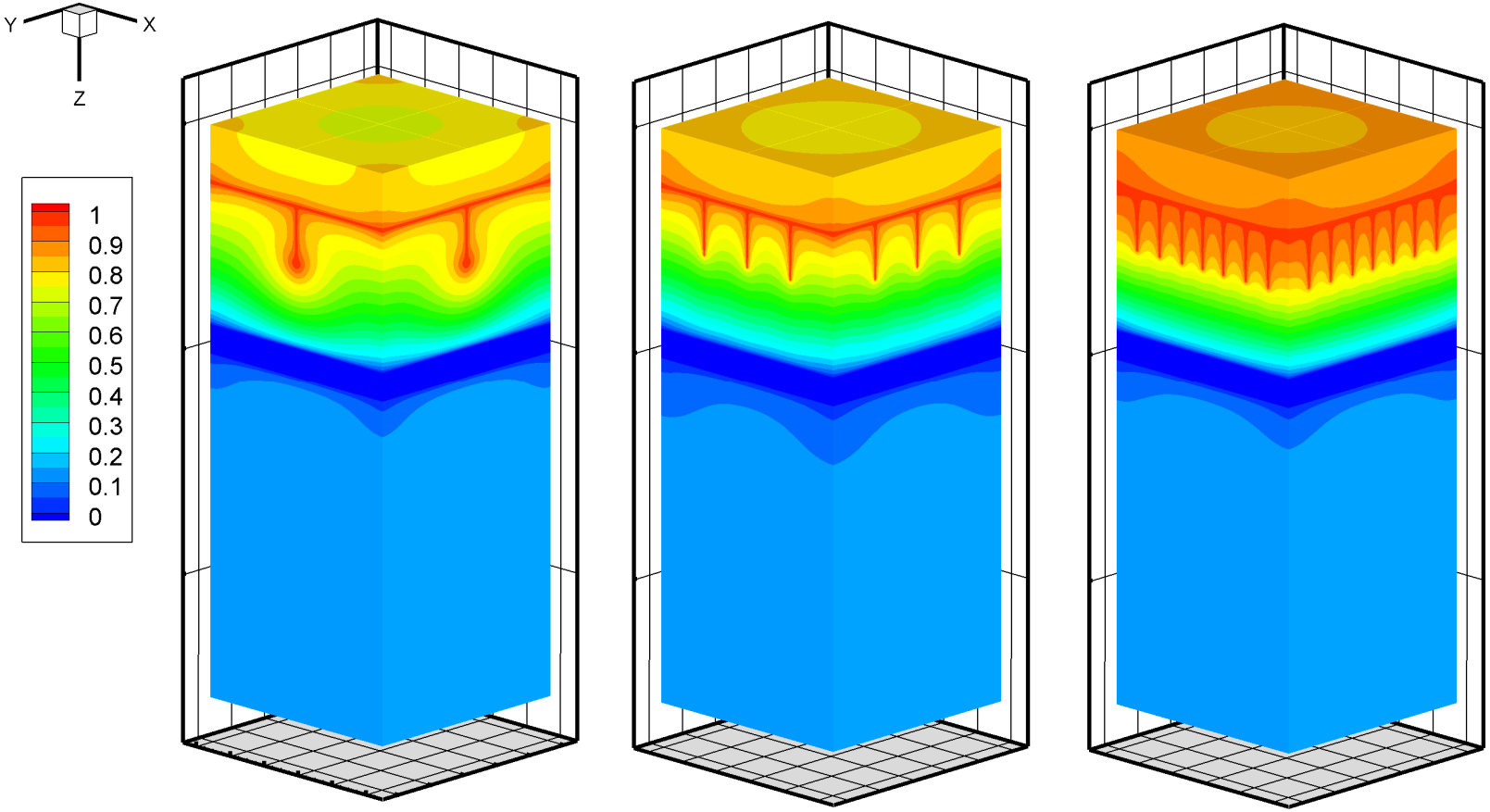

Figure 4.1 Electric potential distribution of an EHD gas pump ($V_0 = 24$ kV, $\Delta\overline{V} = 0.05$)
(a) 4 electrode pins, (b) 12 electrode pins, (c) 28 electrode pins

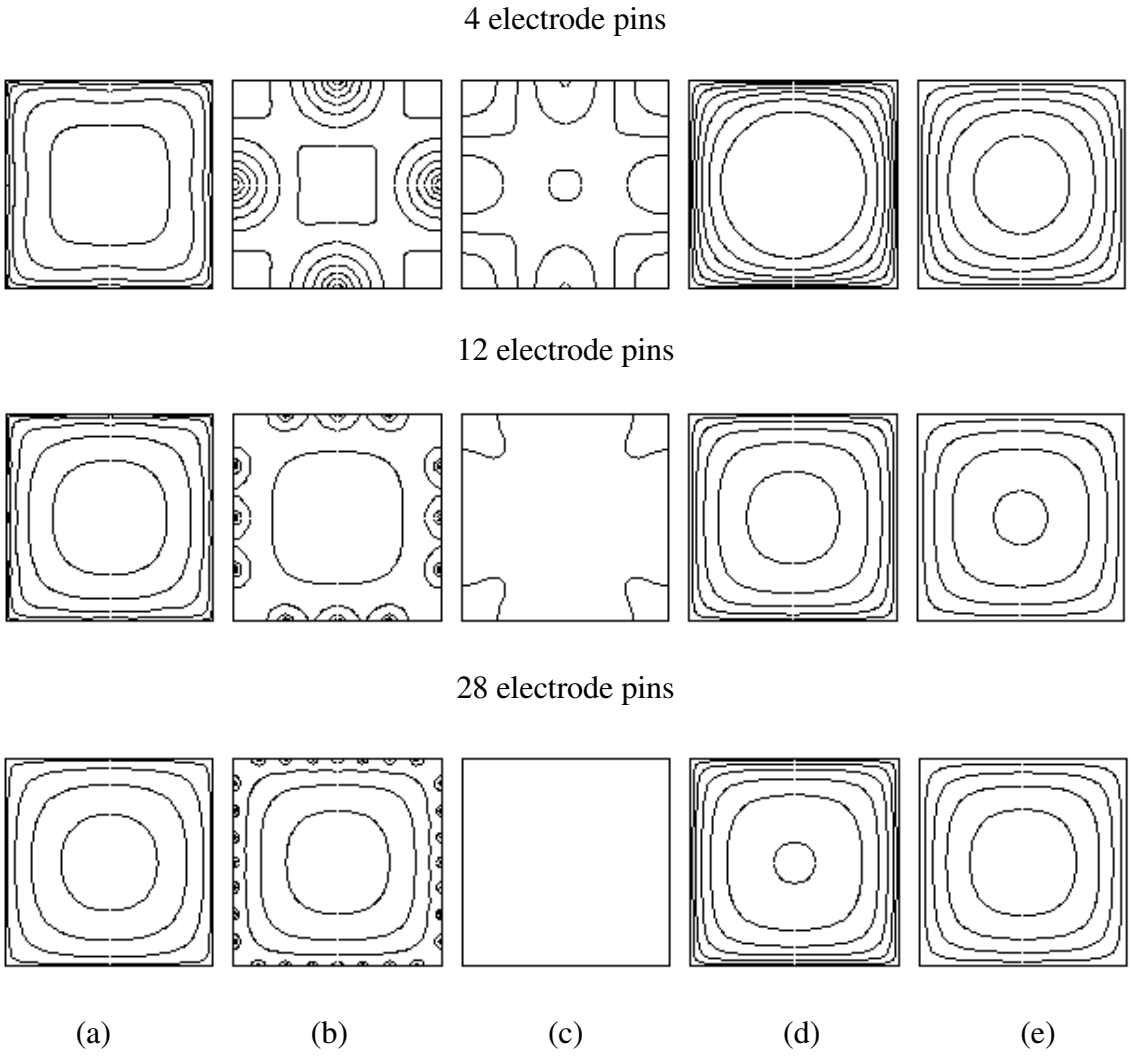

Figure 4.2 Electric potential distributions at various cross-sections ($V_0 = 24$ kV, $\Delta\bar{V} = 0.05$) (a) $\bar{z}=1/4$, (b) $\bar{z}=1/2$, (c) $\bar{z}=11/16$, (d) $\bar{z}=7/8$, (e) $\bar{z}=1$

To demonstrate the effect of applied voltage on the development of the electric potential inside the channel, the electric potential contours at various cross-sections are presented in Fig. 4.3 for the configuration with 12 electrode pins at different applied voltages. The electric potential intensifies as the applied voltage increases. At the applied voltage of 20 kV, the influence due to the presence of the electrode pins disappears at the level midway between the electrode tips and the grounded plate ($\bar{z} = 11/16$) whereas this influence can still be seen for the applied voltages at 24 kV and 28 kV. Near the grounded plate ($\bar{z} = 7/8$ and $\bar{z} = 1$), the potential gradient is much higher for the applied voltage at 28 kV than those at the lower voltages.

Space charge density distributions are shown in Fig. 4.4 for an EHD gas pump with 4 electrode pins, 12 electrode pins, and 28 electrode pins at an applied voltage of 24 kV. The charge density displayed is also normalized with its value at the electrode tips. As observed, space charges are centered around the electrode tips and spread downwards to the grounded plate. For the configuration with 4 electrode pins, space charges are highly concentrated around the electrode tips, and its density reduces dramatically within a short distance away from the tips. However, as the number of the electrode pins increases, space charges fill up the entire region between the electrode tips and the grounded plate.

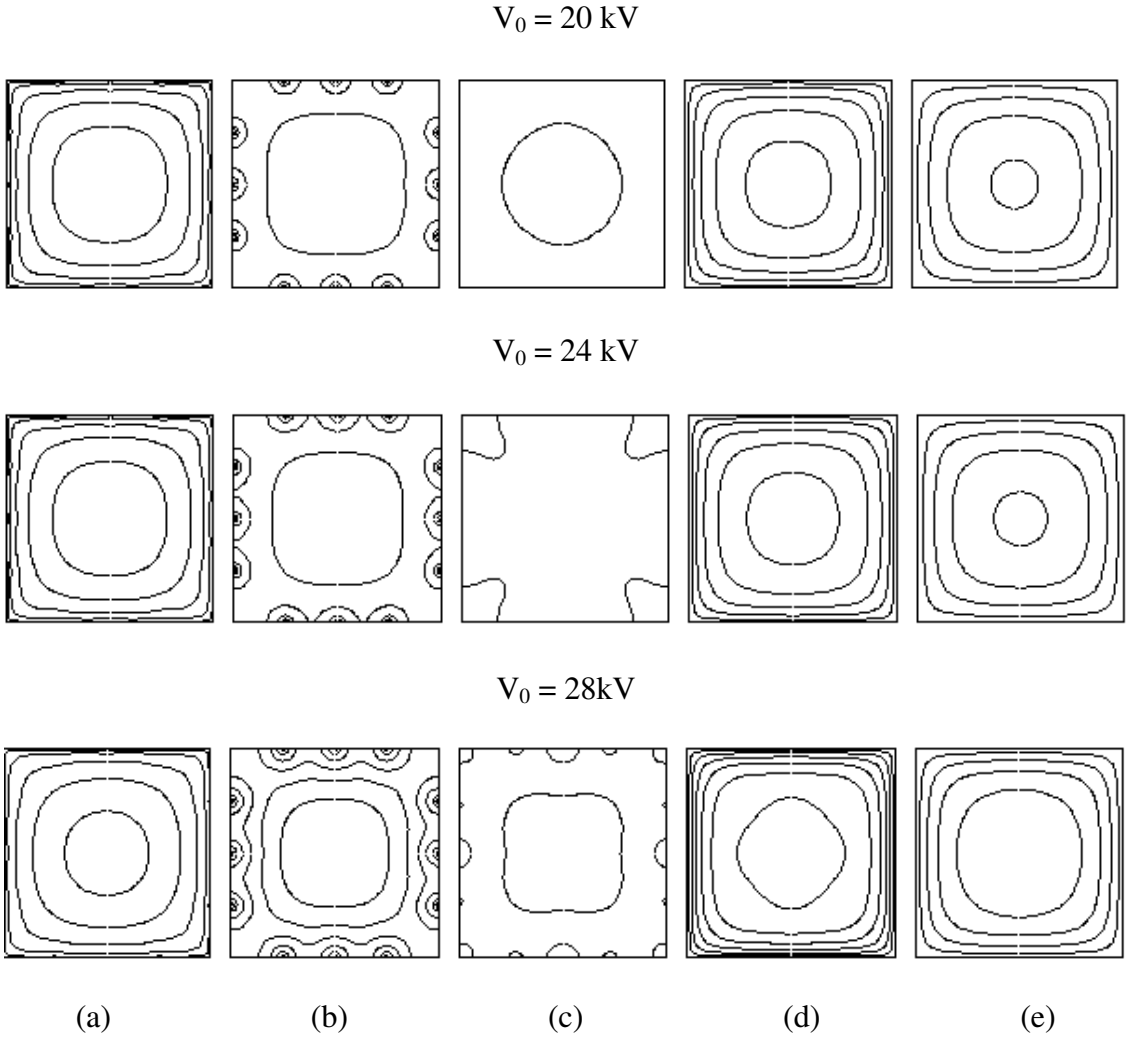

Figure 4.3 Electric potential distributions at various cross-sections (12 pins, $\Delta\overline{V} = 0.05$)
(a) $\overline{z}$=1/4, (b) $\overline{z}$=1/2, (c) $\overline{z}$=11/16, (d) $\overline{z}$=7/8, (e) $\overline{z}$=1

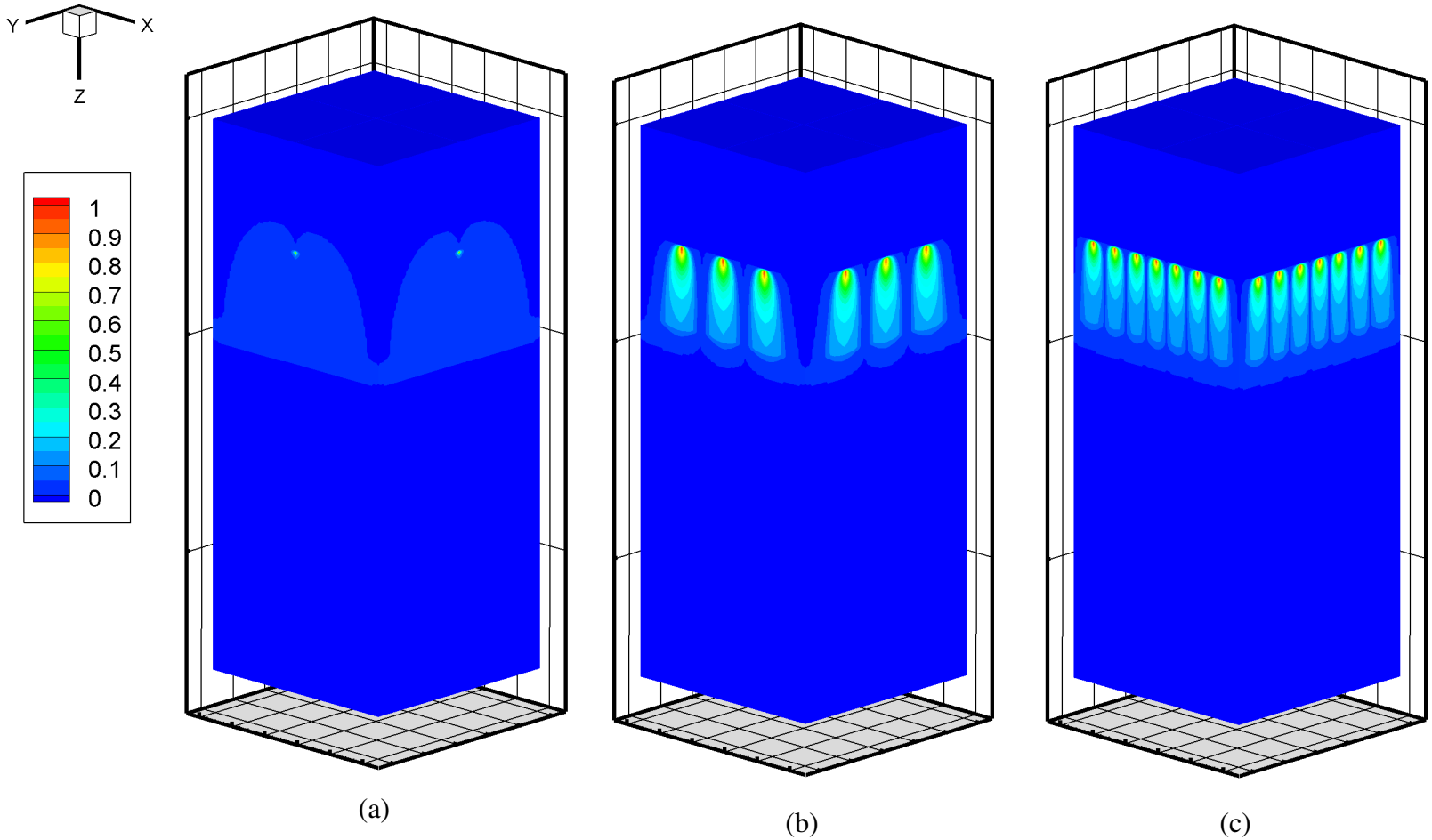

Figure 4.4 Space charge distribution of an EHD gas pump ($V_0 = 24$ kV, $\Delta\overline{\rho_c} = 0.05$)
(a) 4 electrode pins, (b) 12 electrode pins, (c) 28 electrode pins

To understand the reason why the space charges are highly concentrated around the electrode tips for the configuration of 4 electrode pins, it is useful to recall the definition of the corona current, Eq. 3.24. Given the same applied voltage for all configurations, the one with 4 electrode pins has the highest current. From the electric potential distribution (Fig. 4.2), the configuration with 4 electrode pins has the lowest potential gradient around the electrode tips among all the configurations considered. Therefore, it follows that the configuration with 4 electrode pins has the highest space charge concentration around the electrode tips.

Figure 4.5 illustrates the space charge density distributions for all the configurations on the same cross-sectional levels as shown in Fig. 4.2. No space charge is shown on the cross-section at the wire-loop level ($\bar{z} = 1/4$) since space charge propagates as a one-dimensional wave from the electrode tips towards the grounded plate. At the level of the electrode tips, space charges are confined to a small region near the tips, as seen from the cross-section $\bar{z} = 1/2$. At a cross-section downstream of the electrode tips ($\bar{z} = 11/16$), the space charge density decreases and spreads towards the center of the channel. For the configuration with 4 electrode pins, the charge density is too weak ($\overline{\rho_c} \le 0.05$) to show on the contour plots. Although the charge density decreases dramatically as it approaches the grounded plate, the space charge field seems to be the strongest for the configuration with 12 electrode pins than that with 28 pins, which can be seen from the cross-sectional contours at $\bar{z} = 11/16$ and $\bar{z} = 7/8$. No space charges exist below the level of the grounded plate.

.

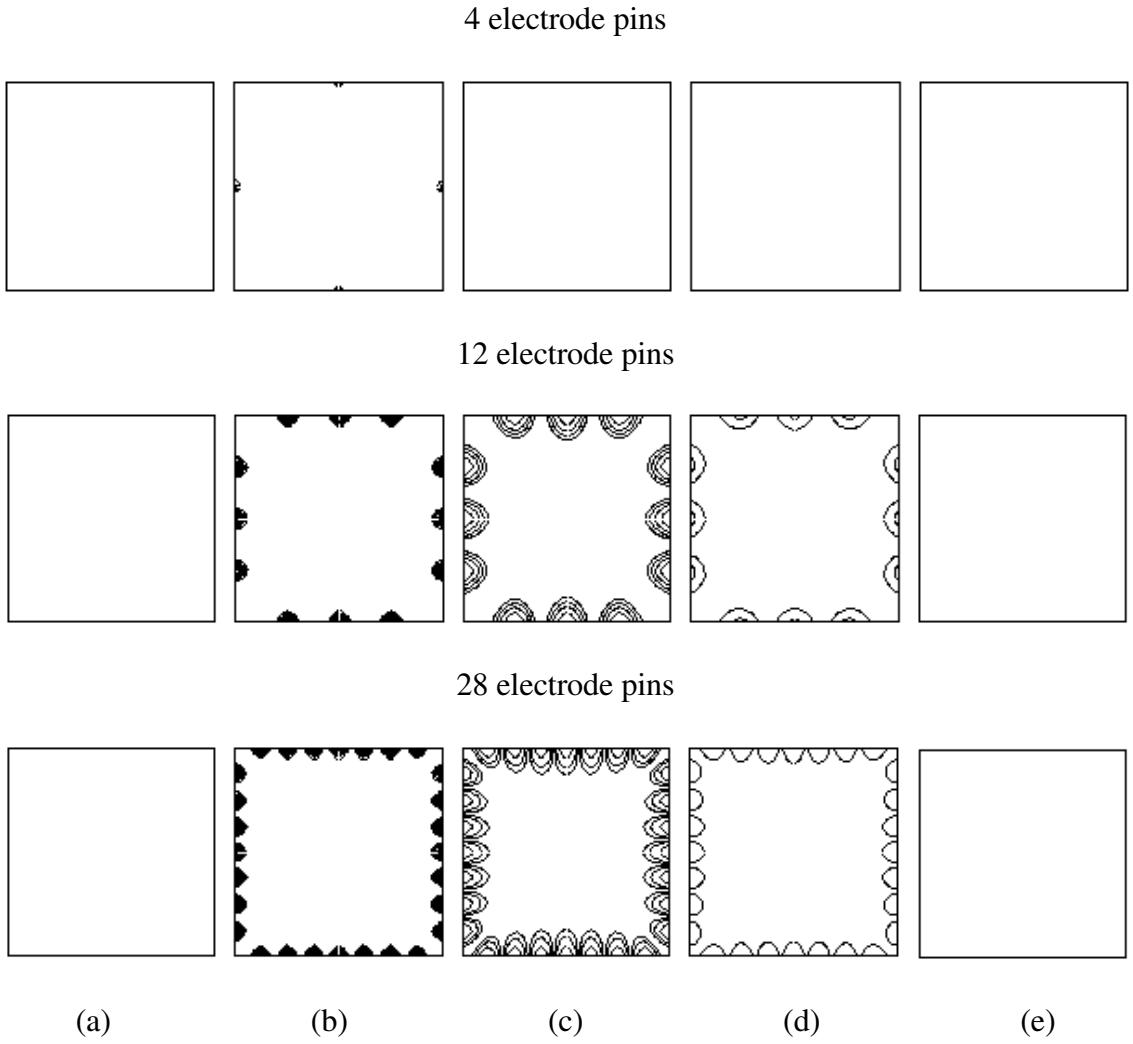

Figure 4.5 Space charge distributions at various cross-sections, (V_0 = 24 kV, $\Delta\overline{\rho_c}$ = 0.05)
(a) $\bar{z}$=1/4, (b) $\bar{z}$=1/2, (c) $\bar{z}$=11/16, (d) $\bar{z}$=7/8, (e) $\bar{z}$=1

To examine the effect of applied voltage on the space charge field, the space charge distributions of the configuration with 12 electrode pins at various cross-sections are shown in Fig. 4.6. It is observed that space charge densities at lower voltages are higher than those at higher voltages, which may seem contradictory to one's intuition that higher voltages should produce larger space charges. For any configuration, higher voltages do produce higher currents. However, as discussed earlier, higher currents do not necessarily result in larger space charge densities. The potential gradients need to be taken into account as well. Also noticed that at the applied voltage of 28 kV, space charge density at the cross-section midway between the electrode tips and the grounded plate ($\bar{z} = 11/16$) is too weak ($\overline{\rho_c} \leq 0.05$) to show on the contour plots.

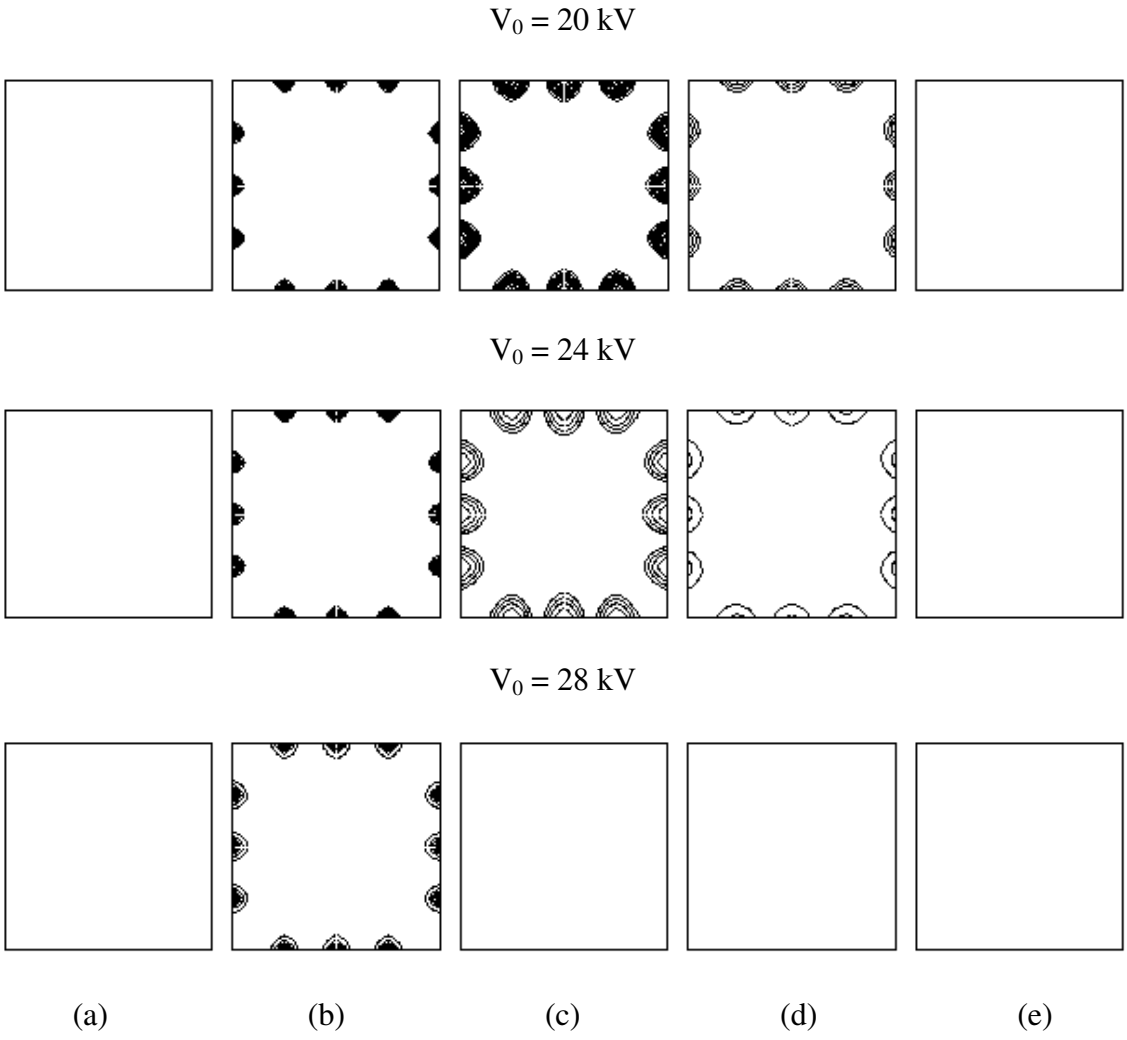

Figure 4.6 Space charge distributions at various cross-sections (12 pins, $\Delta\overline{\rho_c} = 0.05$)
(a) $\bar{z}$=1/4, (b) $\bar{z}$=1/2, (c) $\bar{z}$=11/16, (d) $\bar{z}$=7/8, (e) $\bar{z}$=1

4.2 EHD-Induced Flows

After the solutions of the electric field converge, electric potential and space charge density are available for use in the calculation of the electric body force. The flow field, driven by the electric body force, can then be calculated and compared with the experimental results to validate the computational code.

One is to be reminded that the present experimental results have large uncertainties involved. First, the corona discharge is very sensitive to the ambient conditions, mainly the temperature and relative humidity [17]. The latter is particularly difficult to control in the lab. Secondly, the device used in the present study for measuring velocity is not ideal. Since the diameter of the probe, which is inserted into the flow, is relatively large, it might partially block the flow. These two factors are not accounted for in the uncertainty calculation. The present uncertainty analysis is based on the ASME guidelines on the reporting of uncertainties in experimental measurements [51-52]. The precision error, P_x, for each measured parameter, is based on 95% confidence interval. The bias error, B_x, for measured velocity, can be estimated to be $\pm$ 2.7% of the full scale. The bias error for current is negligible. The theory of propagation of uncertainty is applied to evaluate the total errors in the final results as $W_x = (P_x^2 + B_x^2)^{1/2}$ [53]. The uncertainty is presented by error bars affixed to the experimental data to be shown in the following discussion.

Figure 4.7 shows the velocity profile inside the channel from both experimental results and numerical simulations for the EHD gas pump with 12 electrode pins. As recalled from Chapter two, the velocity measurements are made at nine points at each

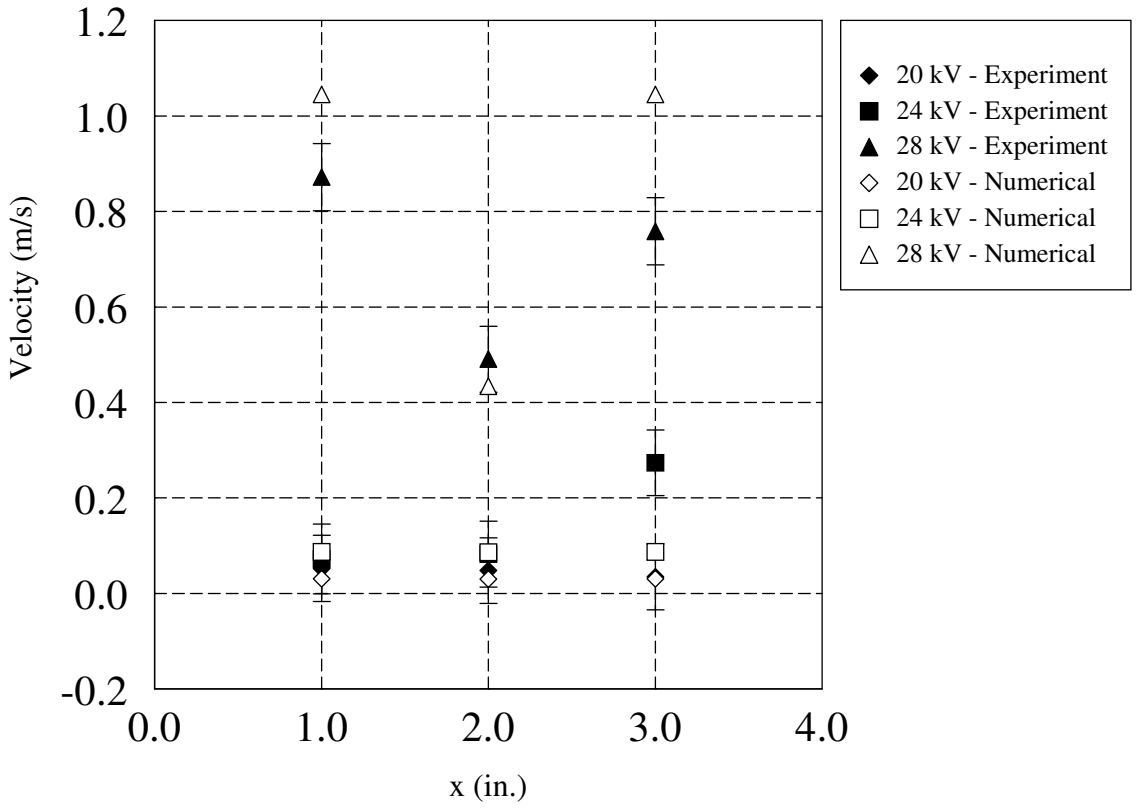

Figure 4.7 Velocity profile comparison, 12 pins

cross-section on three levels, which can provide an approximate velocity profile inside the channel. The x axis represents the channel width with x = 0 and x = 4 referring to the channel walls. As seen from Fig. 4.7, at a low voltage ($V_0 = 20$ kV), the velocity profile appears quite uniform , and there is good agreement between the experimental results and numerical simulations. As the applied voltage increases to 24 kV, the velocity predictions from the numerical simulation are still within the experimental uncertainty range, except for the location at x = 3 inches. It is suspected that the insertion of the velocity probe may affect the flow field to a certain extent. The velocity profiles at this applied voltage are still fairly uniform across the channel. When the applied voltage is further increased to 28 kV, there are some discrepancies between the experimental results and numerical

simulations. Nevertheless, they both present an inverted parabolic velocity profile with the maximum velocities occurring near the walls. This unique shape of the velocity profile reveals that the corona wind issued from the electrode pins behaves like a wall jet, which can be put to good use in the control of boundary layer development. In addition, note that the error bars for the experimental data of 20 kV have extended over the zero velocity line, which indicates that the uncertainties are greater than the measured data themselves. This is because at lower voltages (i.e., weaker corona winds), the bias error is relatively large compared to the measured velocity.

The other two configurations, with 4 electrode pins and 28 electrode pins, show similar characteristics in the velocity profile. The comparisons between their experimental results and numerical simulations also show consistency. The comparison of velocity profiles for these two configurations is included in the Appendix.

Figure 4.8 shows the comparison of volume flow rate between the numerical calculations and experimental results for the three configurations of the EHD gas pump considered. In the experiments, velocities are measured at nine points in a cross-section inside the channel (refer to Fig. 2.5). Each velocity measurement point is assigned a representative portion of the cross-sectional area. The volume flow rate is calculated by summing the products of each velocity and its assigned representative area. Due to the small number of velocity measurement points, this calculation may underestimate the actual volume flow rate. This is because high velocities which are induced close to the wall are not well accounted for. This is especially true at higher applied voltages. As seen from Figure 4.8, at a lower applied voltage ($V_0 = 20$ kV), both configurations with 4 electrode pins and 12 electrode pins have a good agreement between the experimental

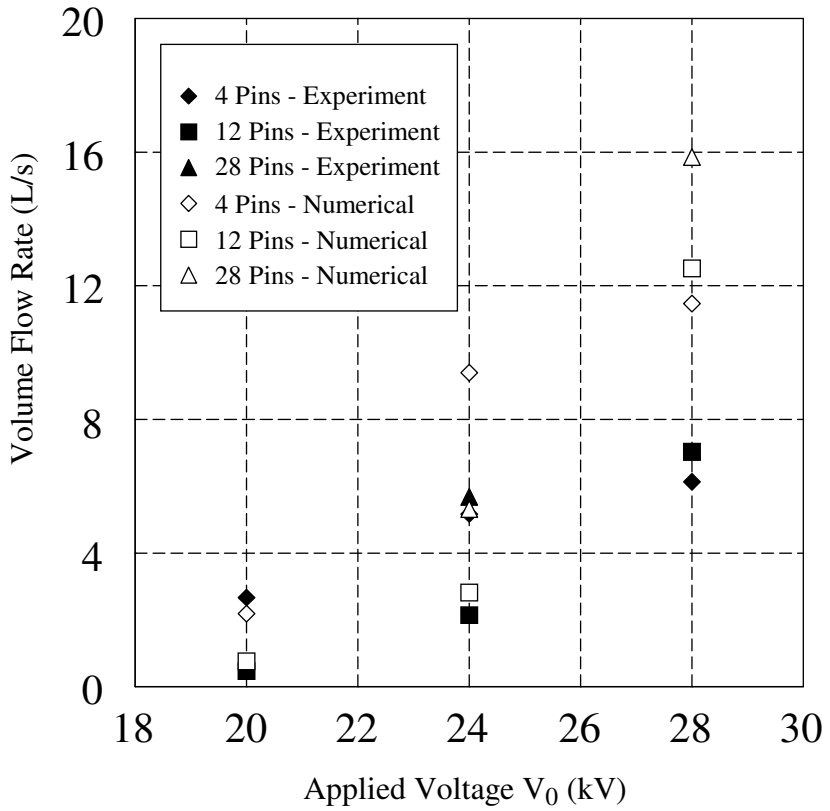

Figure 4.8 Comparison of volume flow rates (positive corona discharge)

results and numerical simulations. The configuration with 28 electrode pins does not produce any volume flow rate at an applied voltage of 20 kV since the onset voltage of corona wind for this particular case is about 21 kV.

When the applied voltage increases to 24 kV, the agreement between the experimental and numerical results is still good except for the configuration with 4 electrode pins. At a higher applied voltage ($V_0 = 28$ kV), the measured volume flow rates are all smaller than the numerical values due to the reasons given before. Note that the configurations with 12 electrode pins and 28 pins produce the same volume flow rate at 28 kV in the experiments. This might be due to the experimental uncertainty involved. In

general, numerical results show the same trend as that of the experiments, that is, the volume flow rate increases with an increase in the applied voltage for any configuration.

The experimental measurements can only provide limited information about the flow field inside the channel with an EHD gas pump. This is because a hot-wire anemometer (an intrusive measuring device) is used for velocity measurements in the present study. In fact, even with non-intrusive devices such as laser doppler velocimetry (LDV) or particle image velocimetry (PIV), it is difficult to obtain accurate velocity measurement in these experiments due to the fact that the seeding particles can be charged by the imposing electric field. This could interfere with what would otherwise be the normal performance of the corona wind within the channel. As such, numerical simulations not only provide velocity data for verification, but also provide means for flow visualization.

Figure 4.9 shows an overview of velocity contours from the numerical simulation of the EHD gas pump with a configuration of 12 electrode pins. It is clearly observed that higher velocities occur near the electrode pins where the electric field is most intense. Also observed are some low-velocity regions at each corner of the channel. At the applied voltage of 28 kV, the maximum velocity inside the channel is about 5 m/s. This EHD gas pump induces a fairly uniform flow with a magnitude of 1 m/s at the inlet of the channel. This figure gives a general idea of EHD-induced flow in a channel with electrode pins mounted on the channel walls. To better understand the flow characteristics, it is necessary to examine the flow field at various cross-sections inside the channel.

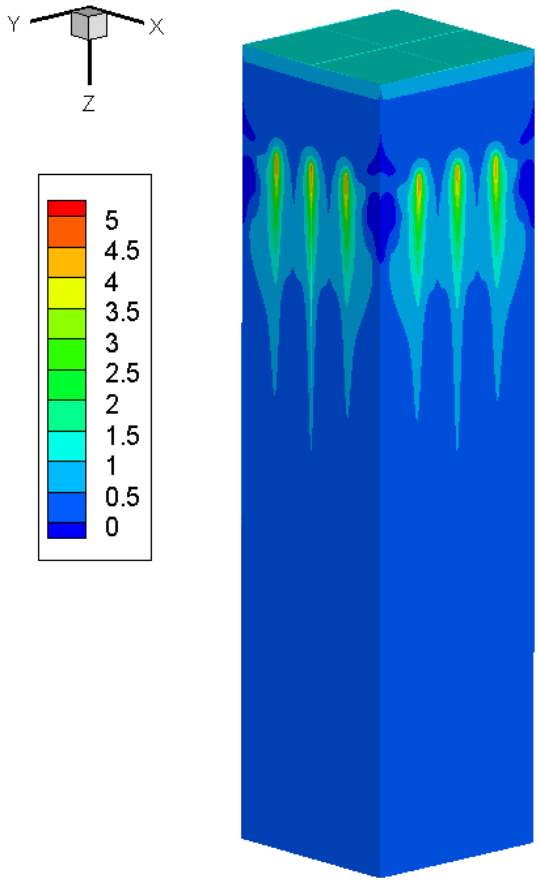

Figure 4.9 EHD-induced flow (12 pins ,V_0 = 28 kV)

Figure 4.10 depicts the EHD-induced flow field in the form of velocity contours at the cross-section of $\bar{x} = 1/2$ (a mid-plane of the channel) for the EHD gas pump with 12 electrode pins. The velocity contours at this cross-section show the flow development in z-direction inside the channel. These velocity contours are in the range between 0 and 5 m/s and they are plotted in the increment of 0.2 m/s. The maximum velocities observed at this cross-section for the applied voltages of 20 kV, 24 kV, and 28 kV are about 1 m/s, 2 m/s, and 5 m/s, respectively. It is also observed that the flow is initiated from the electrode tips and develops downwards. Furthermore, the high-velocity stream is turned away slightly from the channel walls, which can be clearly seen from Fig. 4.10 (a). When

the applied voltage increases, the induced flow not only develops further downstream but also expands towards the center of the channel. The velocity gradient near the electrode tips is much greater for a higher applied voltage. In addition, Fig. 4.10 (c) clearly shows an inverted parabolic velocity profile with the maximum velocity close to the channel walls, which is the opposite of the velocity profile for a fully-developed channel flow. It is this flow characteristic that makes the surface-corona a potential tool for the heat transfer enhancement.

To demonstrate the effect of the number of electrode pins on the flow field, velocity contours are shown in Fig. 4.11 for an applied voltage of 24kV at the cross-section of $\bar{x} = 1/2$ for all three electrode configurations. The contour plots in this figure have the same range as before (0 to 5 m/s) and are plotted with an increment of 0.2 m/s. The maximum velocities for the configurations with 4 pins, 12 pins, and 28 pins are 4 m/s, 1.9 m/s, and 2.2 m/s, respectively. At the applied voltage of 24 kV, the EHD gas pump with 4 electrode pins produces the highest velocity among all three configurations. With an increase in the number of electrode pins, the flow field becomes mostly confined to a small region close to the channel walls due to the interactions between neighboring electrodes.

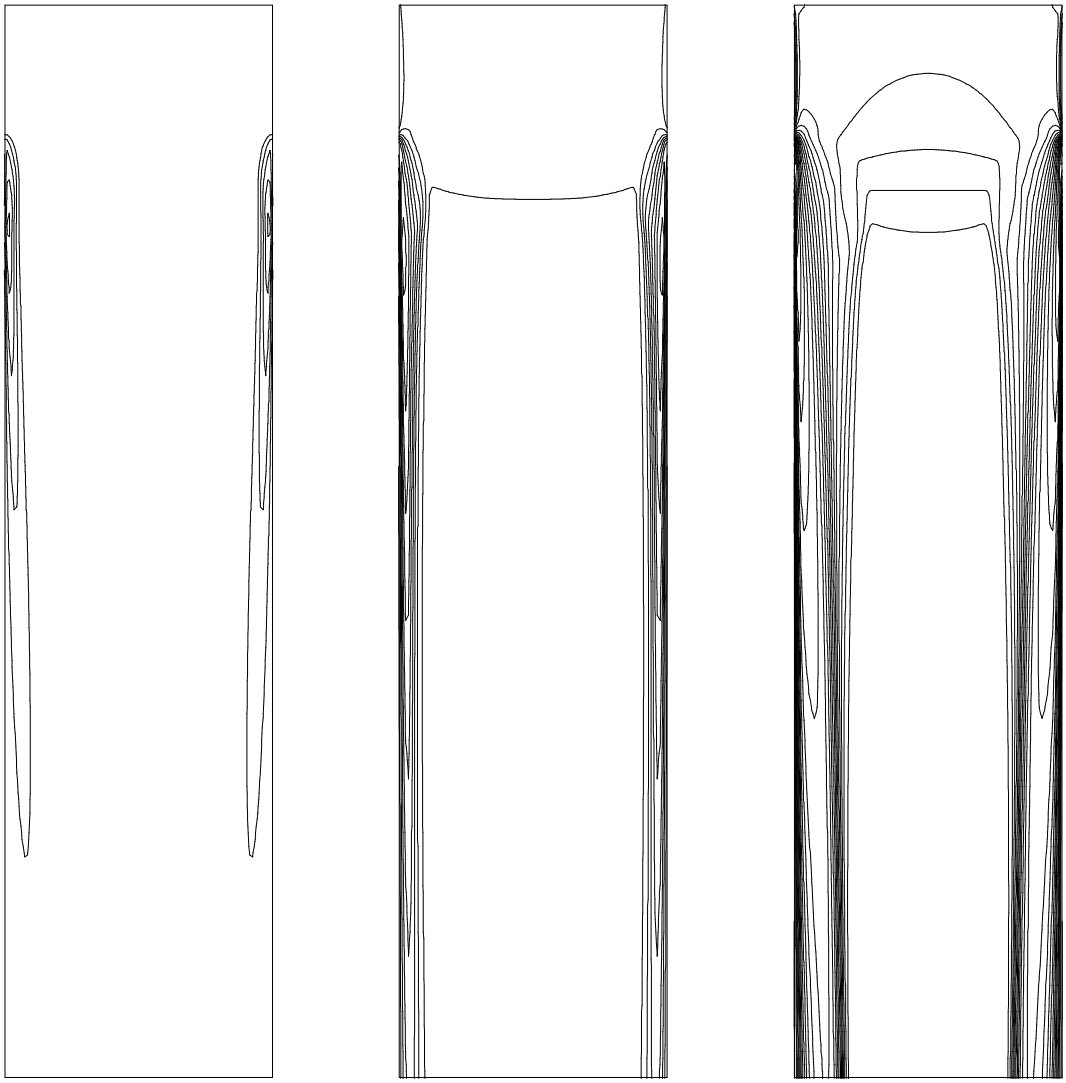

(a) (b) (c)

Figure 4.10 EHD-induced flow field at $\bar{x}$ =1/2 (12 pins)
(a) V_0 =20 kV, (b) V_0 =24 kV, (c) V_0 =28 kV

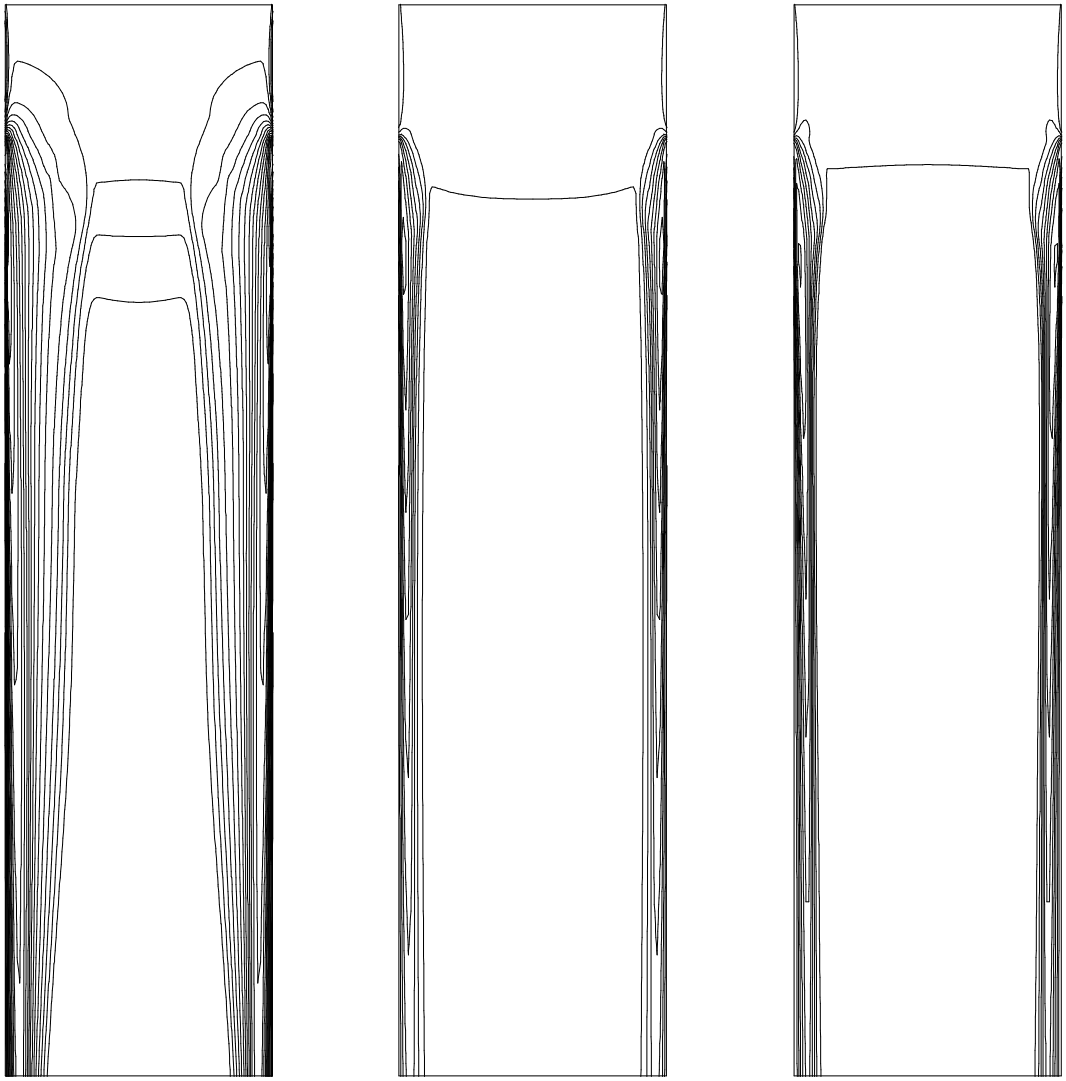

(a) (b) (c)

Figure 4.11 EHD-induced flow field at $\bar{x} = 1/2$ ($V_0 = 24$ kV)
(a) 4 pins, (b) 12 pins, (c) 28 pins

Figures 4.12 - 4.14 show the EHD-induced flow field at various cross-sections along the z axis for the EHD gas pump with 12 electrode pins. In these figures, cross-section (a) is located at the level of the electrode wire loop ($\bar{z} = 1/4$). Cross-section (b) is located at the level of the electrode tips ($\bar{z} = 1/2$). Cross-section (c) is located in between the electrode tips and the grounded plate ($\bar{z} = 3/4$). Cross-section (d) aligns with the bottom edge of the grounded plate ($\bar{z} = 1$). Both two-dimensional and three-dimensional renderings of the velocity contours are shown at each cross-sectional level. The magnitude of the velocity can be identified from the color scale shown in the legend.

For all applied voltages, the velocity is uniform (and thus the profile is flat) at the electrode wire loop level. The boundary layer development is much faster at a higher applied voltage (Fig. 4.14 (a)) than that at a lower applied voltage (Fig. 5.12 (a)).The corona wind effect becomes more visible downstream as seen from the cross-section at the electrode wire tips. Although the highest charge density occurs at the wire tips, the highest velocity occurs below the wire tips. While the corona wind develops downwards, it also expands towards the center of the channel, which has also been observed in Figure 4.10. These developments are more pronounced at a higher applied voltage than at a lower applied voltage. These renderings clearly illustrate that the corona wind issued from the electrode tip behaves like a wall jet, producing a high velocity gradient near the channel walls and a relatively uniform profile in the center. These three-dimensional displays of velocity profiles have provided excellent support for the experimental data shown in Figure 2.12.

In general, good agreements are observed between the numerical results and experimental data. Numerical simulations have successfully revealed the flow characteristics of the EHD-induced flows in a square channel. In addition, the three-dimensional renderings of the flow field from the numerical study have provided another means of direct flow visualization.

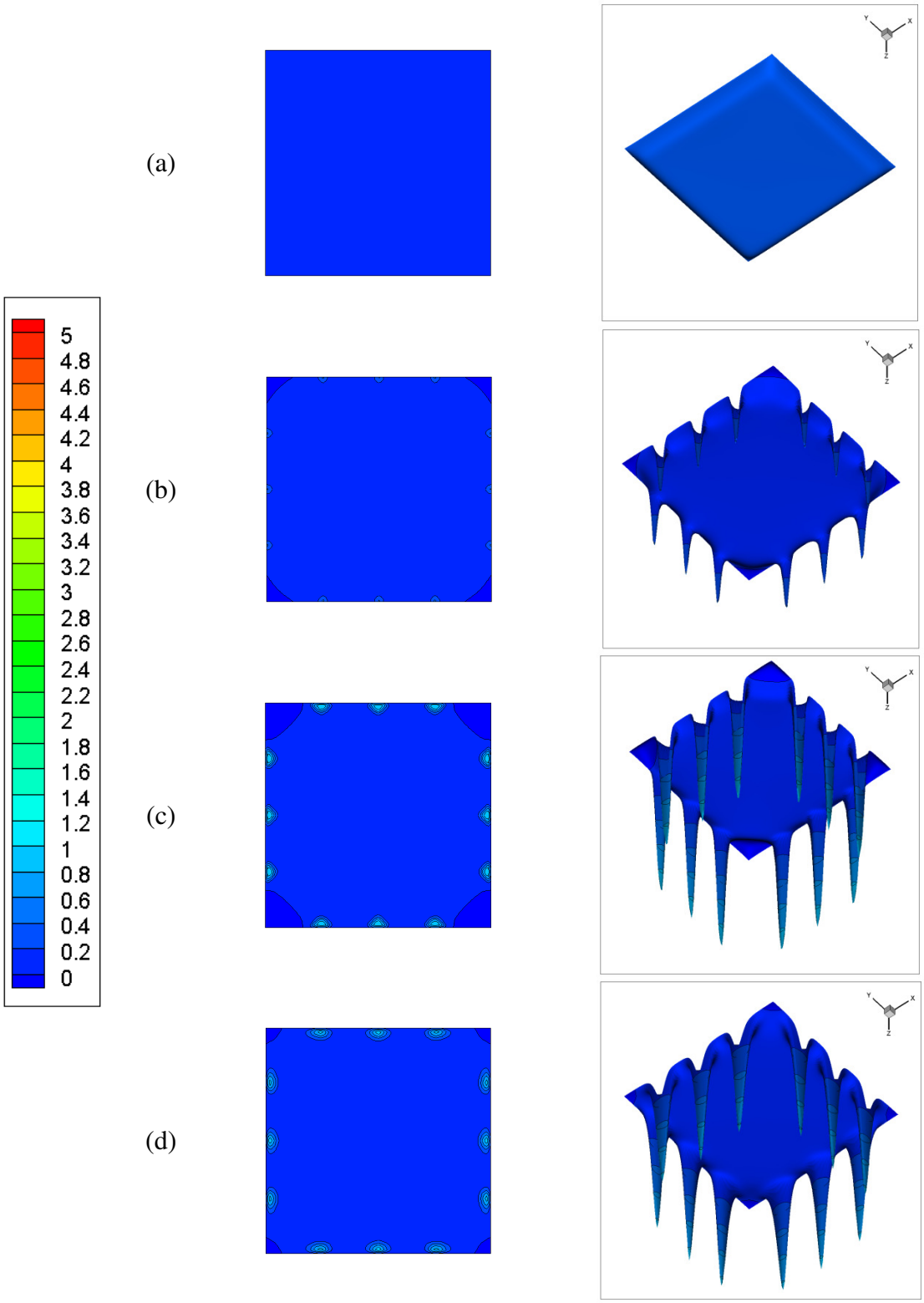

Figure 4.12 EHD-induced flow field at various cross-sections (V_0 = 20 kV)
(a) $\bar{z}$=1/4, (b) $\bar{z}$=1/2, (c) $\bar{z}$=3/4, (d) $\bar{z}$=1

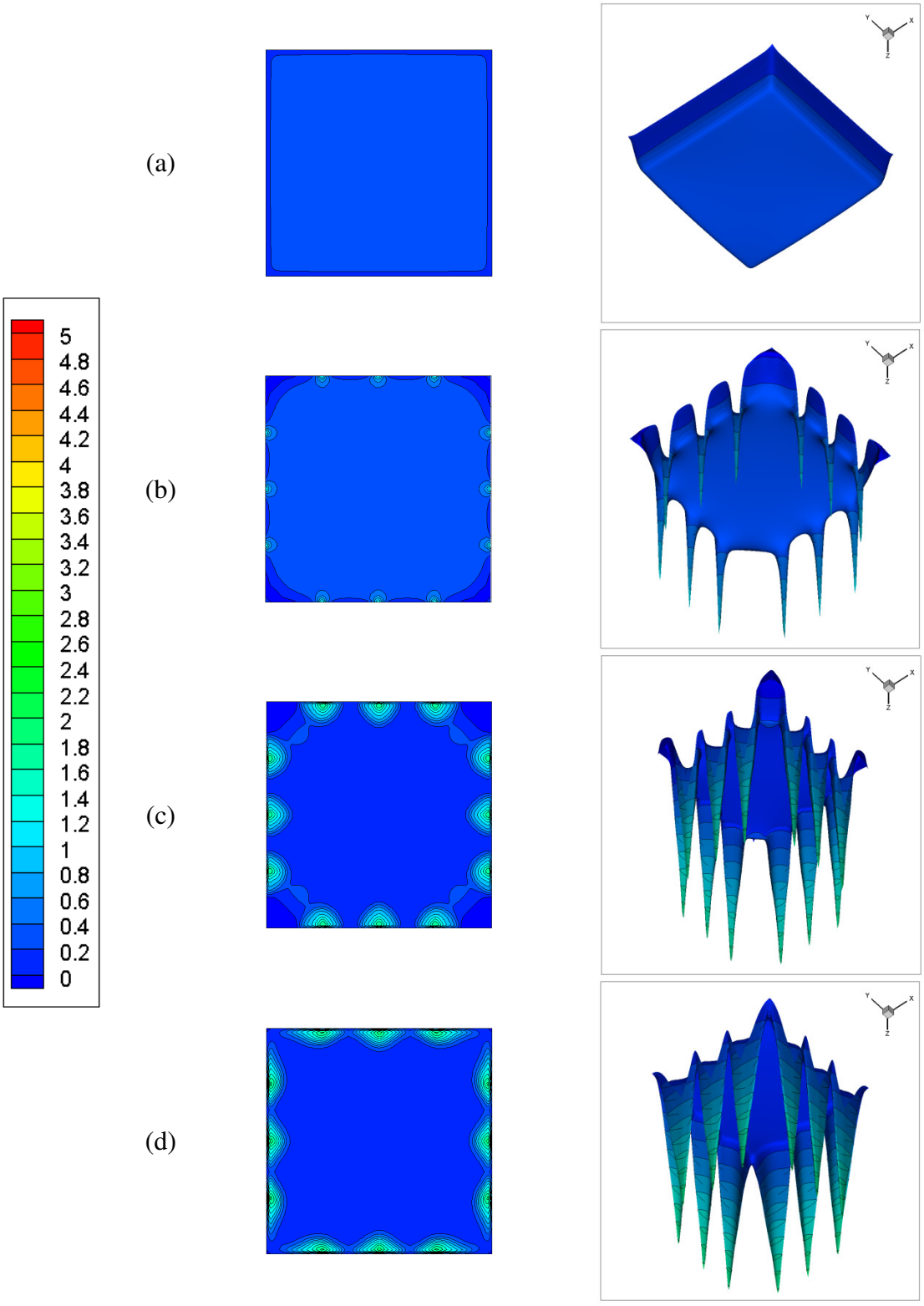

Figure 4.13 EHD-induced flow field at various cross-sections (V_0 = 24 kV)
(a) $\bar{z}$=1/4; (b) $\bar{z}$=1/2; (c) $\bar{z}$=3/4; (d) $\bar{z}$=1

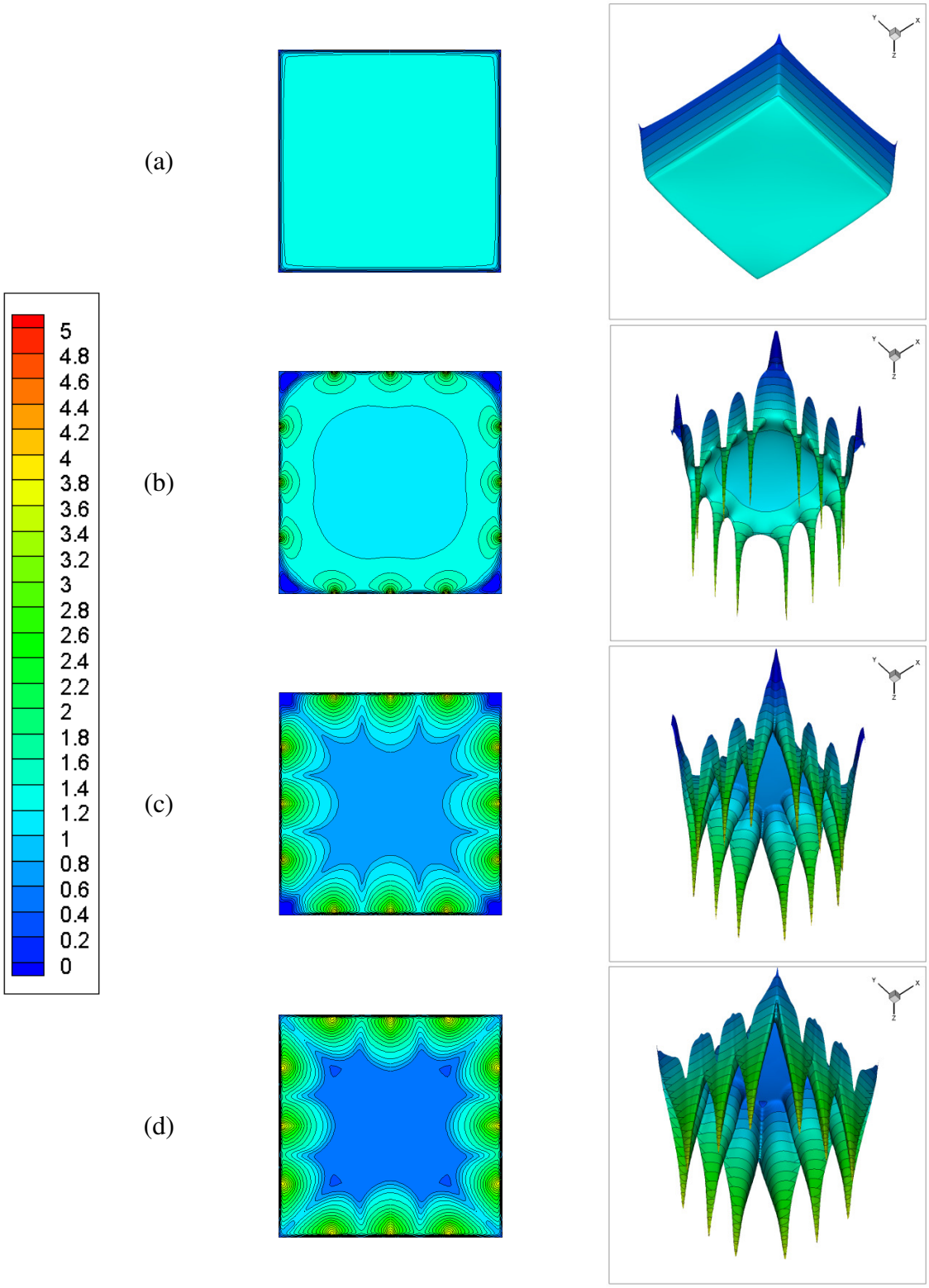

Figure 4.14 EHD-induced flow field at various cross-sections (V_0 = 28 kV)
(a) $\bar{z}$=1/4, (b) $\bar{z}$=1/2, (c) $\bar{z}$=3/4, (d) $\bar{z}$=1

4.3 Forced Convection

To study the effect of corona wind on the heat transfer enhancement, numerical simulations with forced convection are performed with and without the presence of an electric field. The nondimensionlized Navier-Stokes equations along with the energy equation are solved for a wide range of Reynolds numbers.

From the literature review, one learns that the best performance of heat transfer enhancement by EHD occurs in the laminar flow regime. In this study, the range of Reynolds numbers considered varies from 200 to 2000. The Reynolds number is defined based on the hydraulic diameter, which is the channel width for the present case. To examine the interactions between the flow and electric fields, a dimensionless number, N_{EHD}, is used which represents the ratio of the electric body force to the flow inertia. In the present study, the EHD number being utilized was proposed by Davidson and Shaughnessy [54] and it is defined as

$$N_{EHD} = \frac{Id}{\rho u_i^2 bA}, \tag{4.1}$$

where I is the total current, d is the distance between the electrode tip and the grounded plate, and A is the surface area of the grounded plate. When $N_{EHD} \to 0$, the flow inertia is dominant, and the air flow is not affected by the corona wind. On the other hand, when $N_{EHD} \to \infty$, the flow field is dominated by the electric body force, and the air flow is modified by the corona wind.

To examine the heat transfer performance, the heat transfer coefficient is calculated by

$$h = \frac{q}{T_w - T_m}, \tag{4.2}$$

where T_m is the mean fluid temperature. The temperature difference between the wall and the fluid, $T_w - T_m$, is calculated using the logarithmic mean temperature difference (LMTD) [55], which is defined as

$$T_w - T_m = \Delta T_{ln} = \frac{T_i - T_o}{\ln[(T_w - T_o)/(T_w - T_i)]}. \tag{4.3}$$

The heat flux, q, is obtained from Fourier's law by $q = -k\left.\frac{\partial T}{\partial y}\right|_{y=0}$.

The local Nusselt number is defined by

$$Nu_x = \frac{hD}{k} = \frac{(-k\left.\frac{\partial T}{\partial y}\right|_{y=0})\cdot D}{\Delta T_{ln}\cdot k} = -\frac{D}{\Delta T_{ln}}\left(\left.\frac{\partial T}{\partial y}\right|_{y=0}\right), \tag{4.4}$$

where D is the hydraulic diameter. The average Nusselt number is defined in a similar fashion and is given by

$$Nu = -\frac{\ln\theta_0}{1-\theta_0}\cdot\frac{1}{A_s}\iint_{A_s}\left(\left.\frac{\partial\theta}{\partial\bar{y}}\right|_{\bar{y}=0}\right)dA_s. \tag{4.5}$$

where A_s is the heat transfer surface area, θ_0 is the dimensionless temperature at the outlet, and is given by $\theta_0 = (T_0 - T_w)/(T_i - T_w)$.

For a forced flow, the pressure drop across the channel is directly related to the power requirement of a fan or pump to maintain the flow. In practice, it is convenient to express the pressure drop for all internal flows as

$$\Delta p = f \frac{L}{D} \frac{\rho u_m^2}{2}, \tag{4.6}$$

where the dimensionless quantity f is the friction factor [55]. In this formula, the pressure drop Δp is defined as $\Delta p = p_i - p_o$, and L refers to the channel length. In the current study, the friction factor is used to evaluate the power consumption for any given flow and can be calculated by rearranging Eq. (4.6) to give

$$f = \frac{D(\Delta p / L)}{\frac{1}{2}\rho u_m^2}. \tag{4.7}$$

In order to evaluate the effect of the EHD-induced flows, two scenarios are considered. One is forced convection alone without any electric field applied, and the other is forced convection with the presence of electric field. The former case serves as the basis for comparison.

From Figure 4.15, it is evident that for forced convection without an electric field, the Nusselt number increases with an increase in the Reynolds number. However, the Nusselt number presented is an averaged value, which includes the thermal entrance length where the heat transfer coefficient is usually higher. For a flow with a lower Reynolds number, the thermal entrance length is shorter, resulting in an average Nusselt number closer to the value of a fully developed flow, which is 2.98 for a channel with a square cross-section [55].

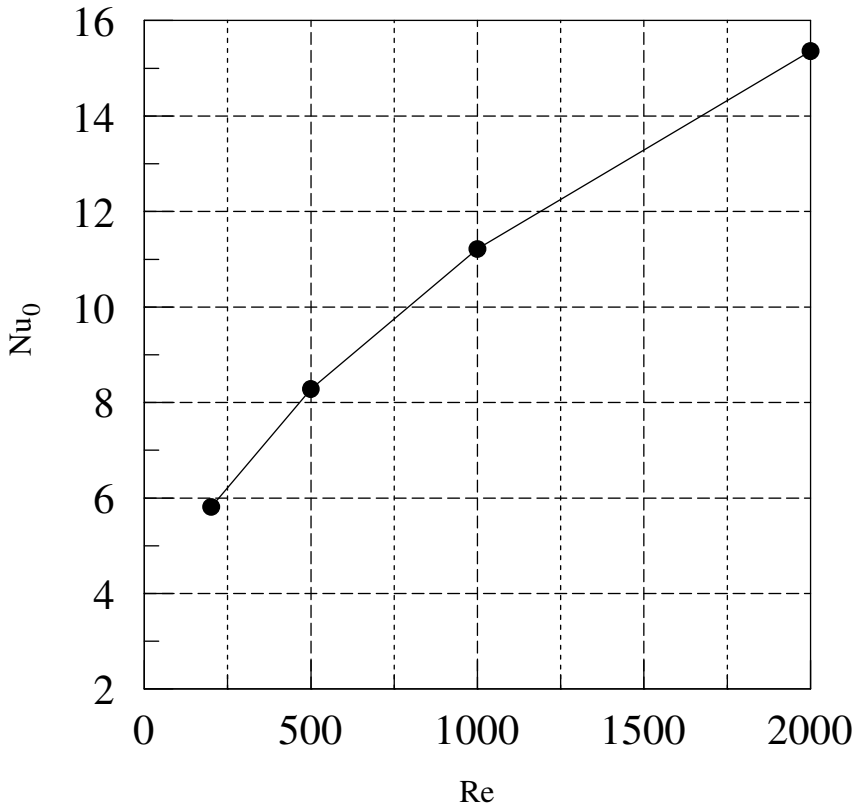

Figure 4.15 Variation of Nusselt number as a function of Reynolds number ($V_0 = 0$ kV)

Forced convection with the presence of an electric field is considered for three electrode configurations with various applied voltages. Figure 4.16 shows the flow field of forced convection with Re = 200 for the configuration with 12 electrode pins at the mid-plane of the channel. When the applied voltage is 0 kV, it refers to the case of pure forced convection, and the flow field displays the normal channel flow pattern. Air enters the channel with a uniform velocity. Due to the fluid viscosity and thus the no-slip condition on the wall, a low velocity region forms along the channel wall, which is the so-called boundary layer. To maintain the same mass flow rate throughout the channel, the fluid velocity at the midsection of the channel must increase. Hence, it leads to a parabolic velocity profile with the maximum velocity at the center. The thickness of the

boundary layer increases until the flow becomes fully developed. The distance from the channel entrance to the point where the flow becomes fully developed, which is called the hydrodynamic entrance length L_h, can be estimated by [56]

$$L_{h,laminar} \approx 0.05 \, Re \, D. \tag{4.8}$$

For Re = 200, the hydrodynamic entrance length is about ten times the hydraulic diameter. However, the length of the current channel is only four times the hydraulic diameter, so the flow is still developing at the exit.

When an electric field is added to the flow field, the fluid around the electrode tips is accelerated by the electric body force. Since the electrodes are mounted on the channel wall, the accelerated fluid disrupts the development of the boundary layer, which can be seen from Fig. 4.16 (b), (c), and (d). The development of the boundary layer resumes again at the electrode tips, and it starts to grow downstream. In a sense, this disruption delays the boundary layer development and extends the hydrodynamic entrance length. At low applied voltages ($V_0 \leq 24$ kV), the velocity profile below the tip level displays a parabolic shape. However, when the applied voltage is very high, for instance $V_0 = 28$ kV, the fluid at the electrode tip is accelerated so much that it even exceeds the flow velocity at the center of the channel, which can be seen from Fig. 4.16 (d). In addition, the high-velocity stream issued from the electrode tip thins the boundary layer, leading to an increase in the velocity gradient near the channel wall below the electrode tips. As the flow develops further downstream, the effect of this disturbance diminishes, the boundary layer grows thicker, and the parabolic velocity profile begins to appear again in the center of the channel.

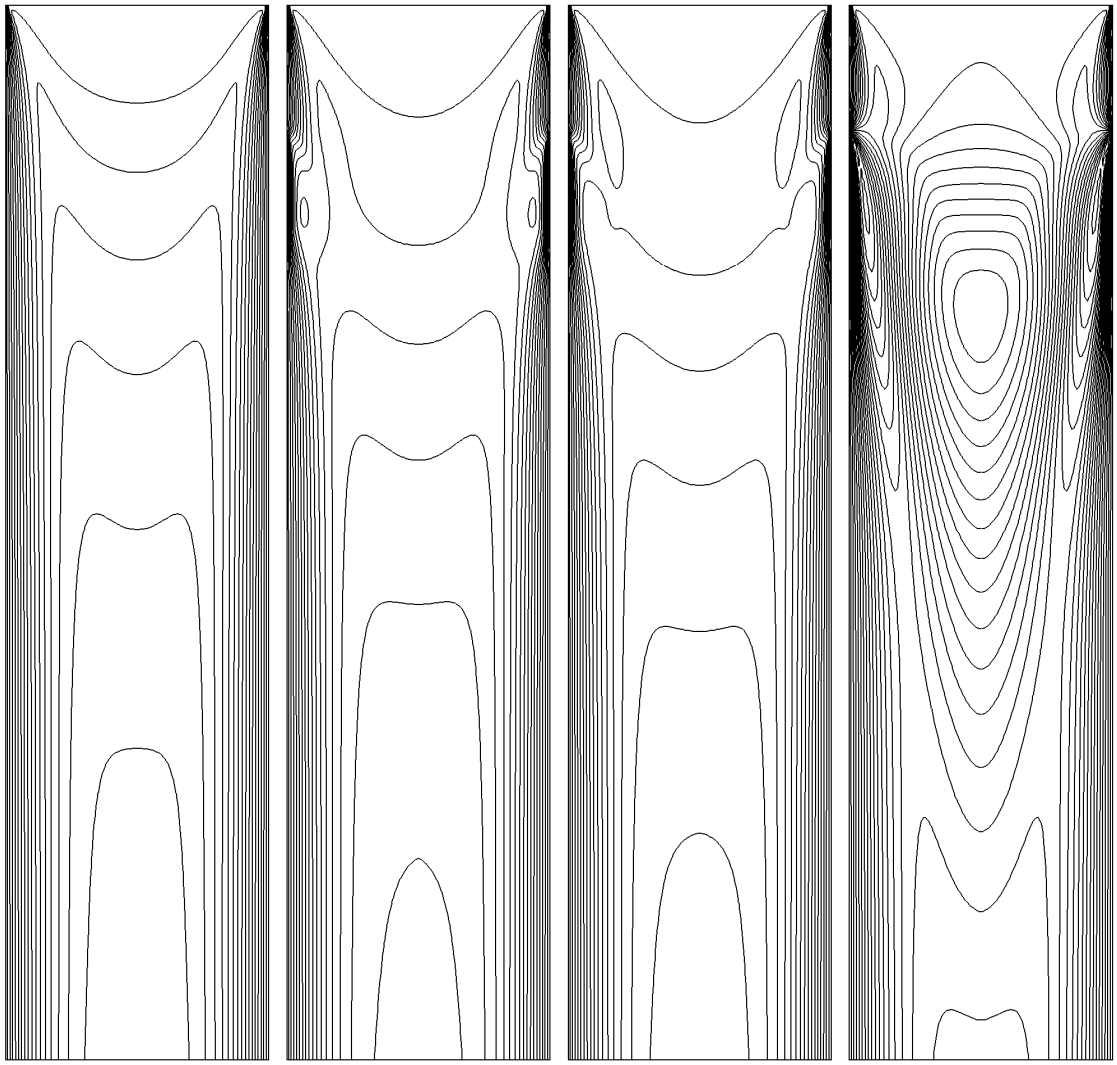

Figure 4.16 Flow field for forced convection with Re = 200, 12 pins ($\bar{x} = 1/2$, $\Delta\bar{w} = 0.1$)
(a) $V_0 = 0$ kV, (b) $V_0 = 20$ kV, (c) $V_0 = 24$ kV, (d) $V_0 = 28$ kV

To better understand the flow development inside the channel, flow fields at various cross-sections along the flow direction are shown in Figs. 4.17 - 4.20 for the configuration of 12 electrode pins at Re = 200. In these figures, cross-section (a) is located at the level of the electrode tips ($\bar{z} = 0.5$). Cross-section (b) is aligned with the bottom edge of the grounded plate ($\bar{z} = 1$) where the constant wall temperature boundary condition applies. Cross-sections (c) and (d) are located further downstream ($\bar{z} = 1.5$ and $\bar{z} = 2$). The velocity contour plot is shown at each cross-section along with its three-dimensional velocity surface plot. The magnitude of velocity can be identified using the color scale shown in the legend. The velocity shown in these figures has been normalized by the velocity at the inlet. For Re = 200, a nondimensional velocity of 2.5 is corresponding to the dimensional velocity of 0.07436 m/s.

Figure 4.17 shows the flow field with no electric field, which serves as a reference for the evaluation of the effect of electric field on the flow field. In this case, air flow develops following the regular pattern of a channel flow. High velocity gradients appear inside the boundary layer where the velocity changes from zero to the free stream velocity. The thickness of the boundary layer increases in the flow direction, as seen from Fig. 4.17 (a) - (d). The flow field near the entrance displays some corner effect (Fig. 4.17 (a)) which diminishes as the flow develops further downstream.

When an electric field is applied to the flow field, fluid around the electrodes is accelerated under the electric body force. Since the electrodes are mounted on the surface of the channel wall, this acceleration disrupts the development of the boundary layer. At the applied voltages of 20 kV (Fig. 4.18) and 24 kV (Fig. 4.19), small disturbances can be

seen on the cross-section at the tip level ($\bar{z} = 0.5$). These disturbances originating from the surface develop inwards and expand downstream, which can be clearly seen from Fig. 4.18 (b) and Fig. 4.19 (b). Further downstream, these disturbances have gradually dissipated and are not visible anymore. However, the boundary layer thickness is thinner compared to that of the case with no electric field at the same location. At a low applied voltage, the influence of electric field to the flow field is only limited to a short distance downstream from the electrode tips. However, when the applied voltage is increased to 28 kV, this influence can extend over a region much further downstream. The high electric intensity has produced a large acceleration in fluid flow. Hence, high velocity gradients are observed at the electrode tips (Fig. 4.20 (a)). Although the largest accelerations occur at the electrode tips, the highest velocities actually appear below the electrodes (Fig. 4.20 (b)). To maintain the same mass flow rate at any cross-section, the high velocities close to the wall result in a low velocity region at the center of the channel. In the three-dimensional surface plots, a familiar profile of wall-jet reveals the effect of electric field. As these high-speed streams develop downwards and inwards, those adjacent to a corner eventually merge, as seen from Fig. 4.20 (c) and (d).

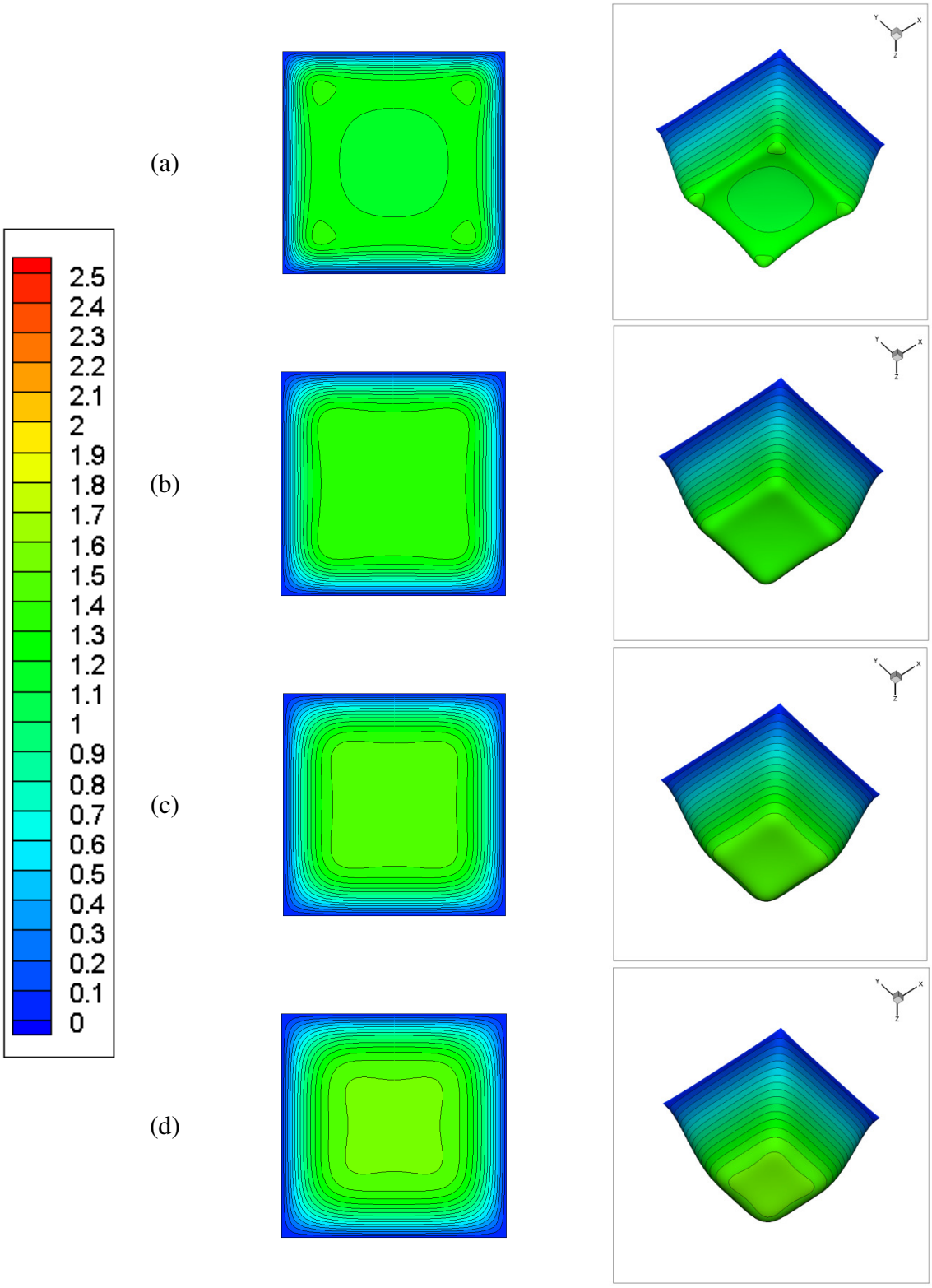

Figure 4.17 Flow field for forced convection with Re = 200 at 0 kV (12 pins, $\Delta\overline{w}$ =0.1)
(a) $\overline{z}$ = 0.5, (b) $\overline{z}$ = 1, (c) $\overline{z}$ = 1.5, (d) $\overline{z}$ = 2

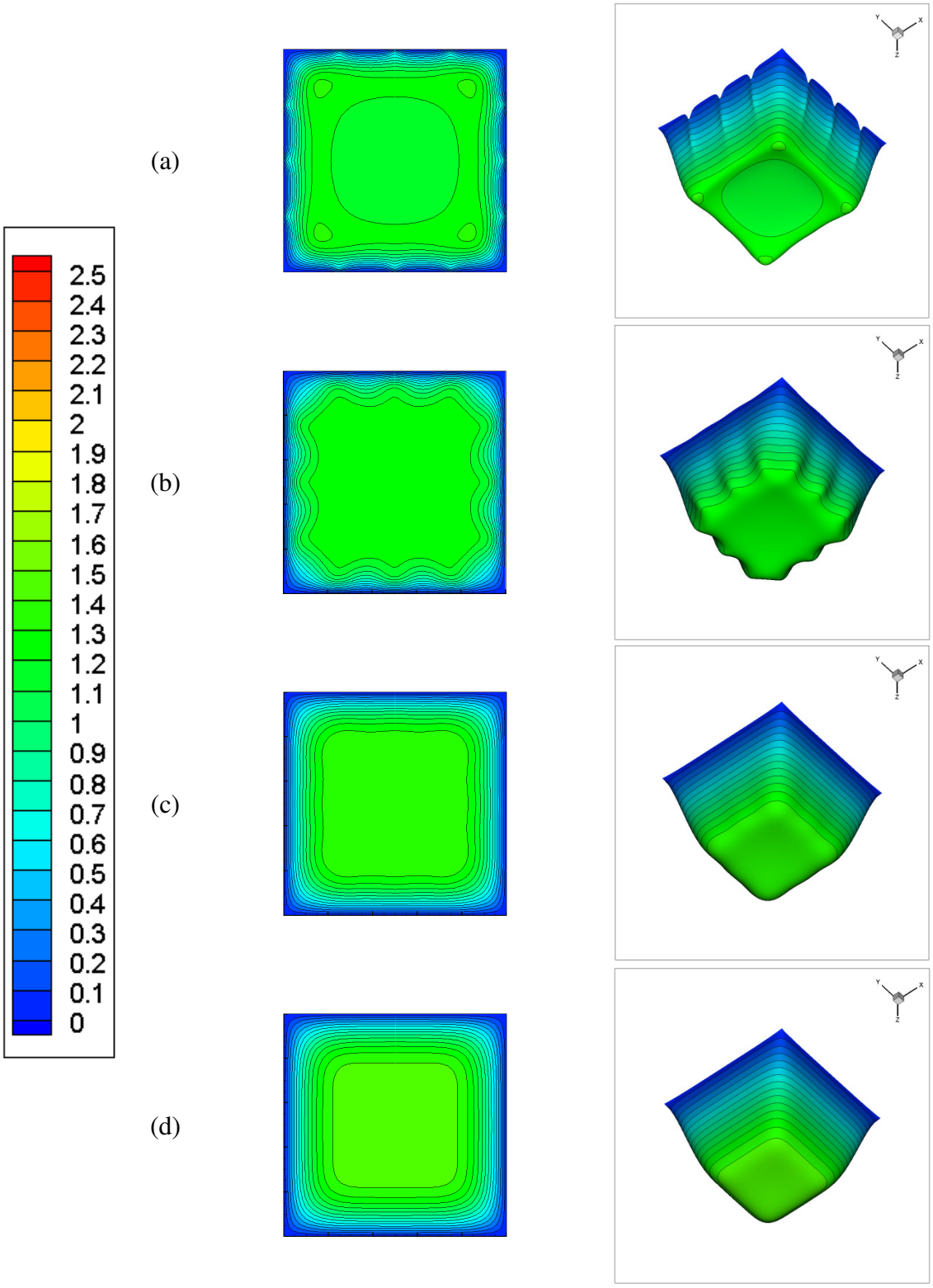

Figure 4.18 Flow field for forced convection with Re = 200 at 20 kV (12 pins, $\Delta\overline{w}$ =0.1) (a) $\overline{z}$ = 0.5, (b) $\overline{z}$ = 1, (c) $\overline{z}$ = 1.5, (d) $\overline{z}$ = 2

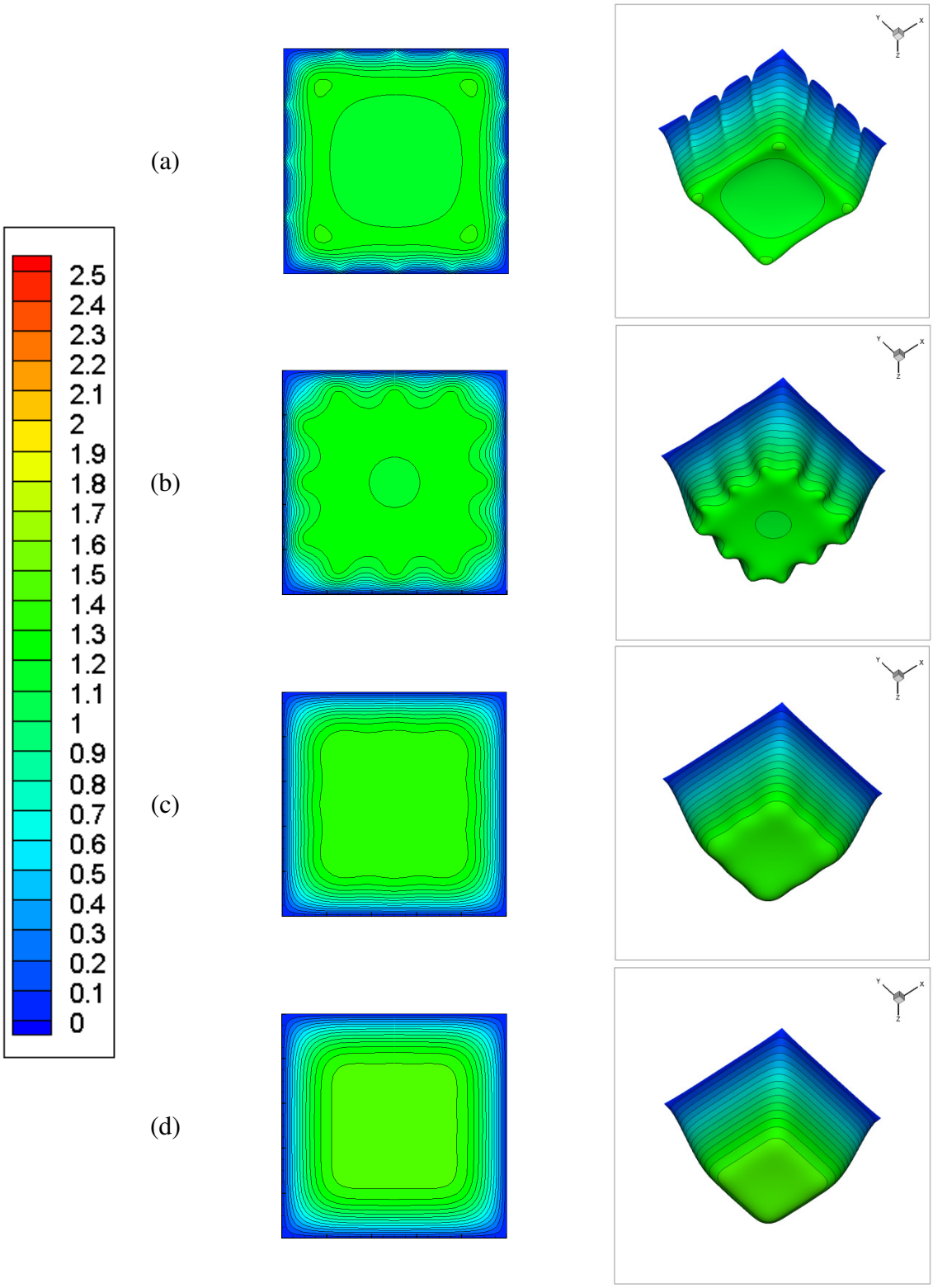

Figure 4.19 Flow field for forced convection with Re = 200 at 24 kV (12 pins, $\Delta\overline{w}$ =0.1)
(a) $\overline{z}$ = 0.5, (b) $\overline{z}$ = 1, (c) $\overline{z}$ = 1.5, (d) $\overline{z}$ = 2

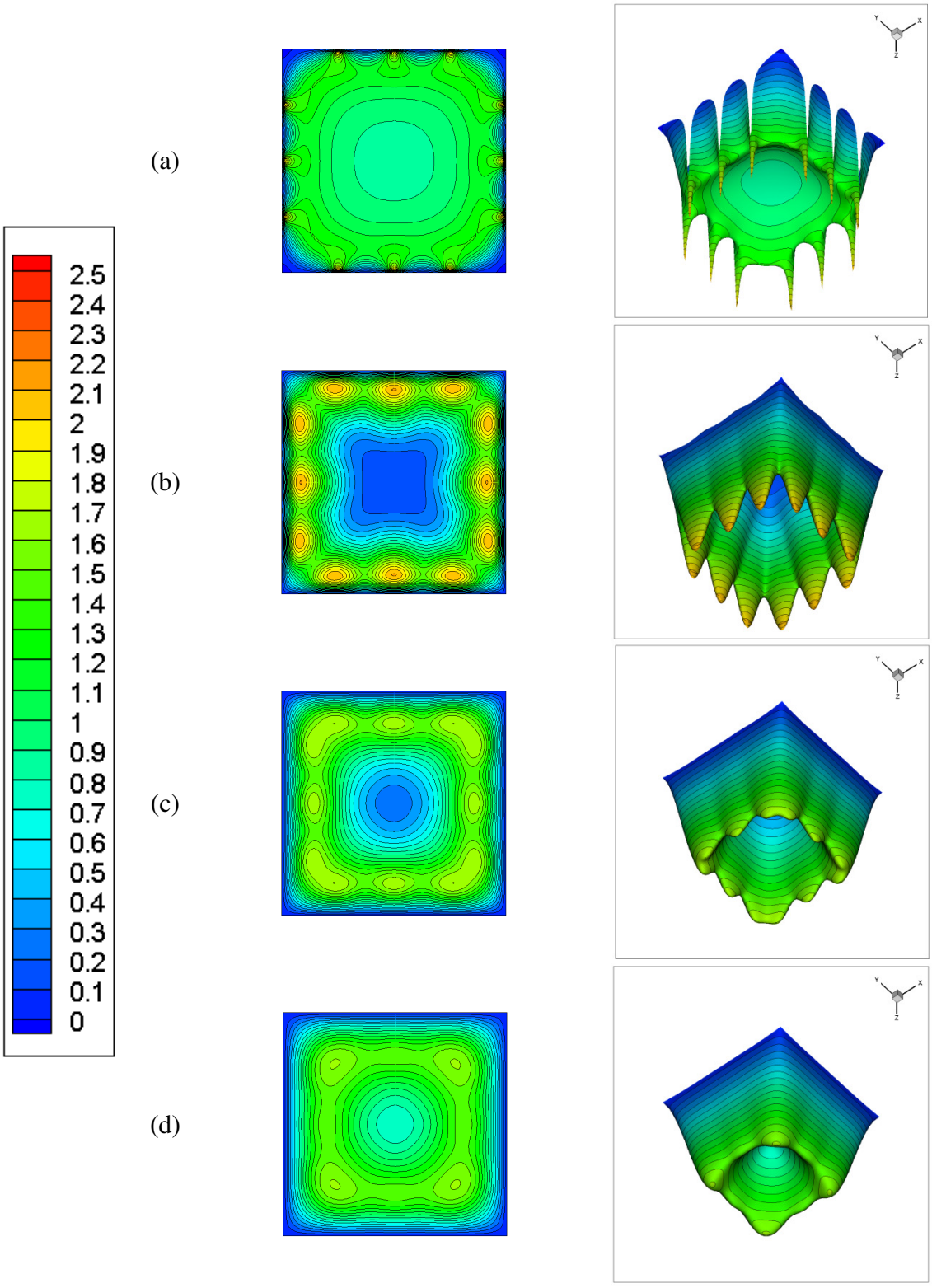

Figure 4.20 Flow field for forced convection with Re = 200 at 28 kV (12 pins, $\Delta\overline{w}$ =0.1)
(a) $\overline{z}$ = 0.5, (b) $\overline{z}$ = 1, (c) $\overline{z}$ = 1.5, (d) $\overline{z}$ = 2

For heat transfer calculations, it is assumed that the top part of the channel (from the channel inlet down to the bottom edge of the grounded plate) is thermally insulated, and below the grounded plate the channel wall is maintained at a constant temperature. Figure 4.21 shows the temperature field at the mid-plane of the channel with Re = 200 for the configuration of 12 electrode pins. Air enters the channel with a constant temperature. Since the top part of the channel wall is thermally insulated, the fluid temperature does not change until it reaches the lower part of the wall. When the fluid in contact with the surface wall, it initiates the convection heat transfer and a thermal boundary layer develops along the channel wall. As seen from Fig. 4.21, this boundary layer starts at the location where the constant wall temperature boundary condition applies, and develops downstream. The thickness of these thermal boundary layers increases until they reach the center of the channel. The distance from where the thermal boundary layer starts to the point downstream where it reaches the center of the channel is called the thermal entrance length L_t, which can be estimated by [56]

$$L_{t,laminar} \approx 0.05\,Re\,Pr\,D. \tag{4.9}$$

For Re = 200, the thermal entrance length for an air flow in a square channel is about seven times the hydraulic diameter. So in the current case, the thermal boundary layer is still developing at the channel exit.

Comparison between the temperature fields with and without the electric field in Fig. 4.21 shows that no significant change occurs when an electric field is imposed. Although the electric field modifies the flow field (from Fig. 4.16), this modification either is confined to a small region near the electrode tips, or moves away from the

channel wall downstream. Hence, it does not produce much of an effect on the thermal boundary layer.

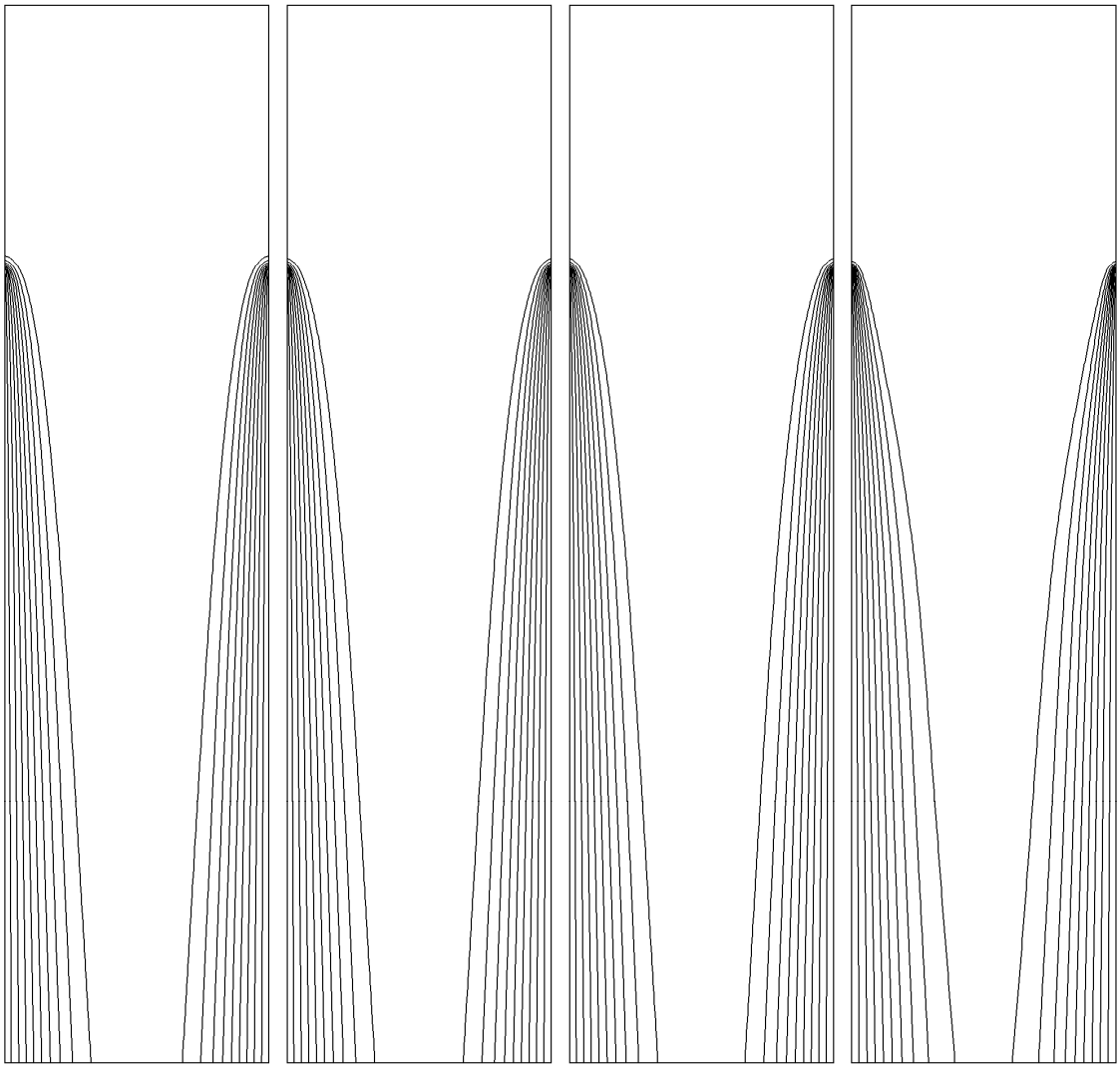

Figure 4.21 Temperature field for forced convection with Re = 200, 12 pins ($\bar{x} = 1/2$, $\Delta\theta = 0.1$) (a) $V_0 = 0$ kV, (b) $V_0 = 20$ kV, (c) $V_0 = 24$ kV, (d) $V_0 = 28$ kV

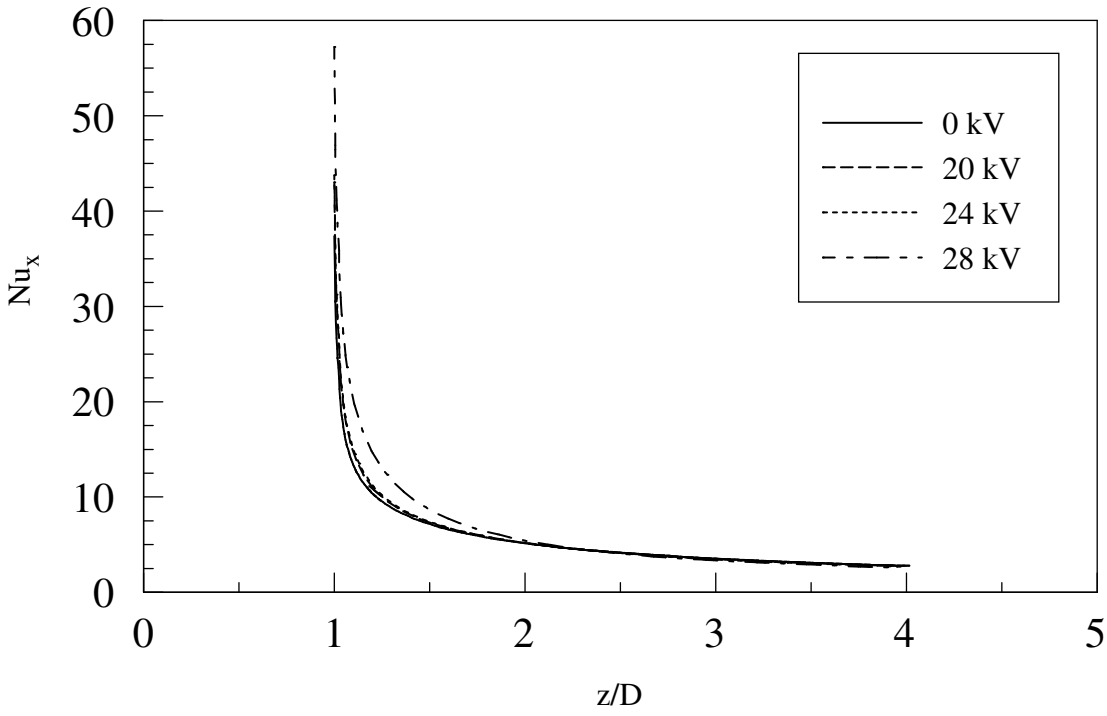

Figure 4.22 Variation of local Nusselt number (Re = 200, 12 pins)

To examine the effect of the electric field on heat transfer, the corresponding local Nusselt number distributions for temperature fields shown in Fig. 4.21 is presented in Fig. 4.22. The location of $z/D=1$ refers to the origin of the thermal boundary layer. As observed, the local Nusselt number decreases dramatically downstream and approaches the value of a fully developed flow. For a higher applied voltage, the Nusselt number curve shifts upwards, however, this increase in the Nusselt number mainly occurs in the region between $z/D=1$ and $z/D=2$. Thus, it is clear that a higher applied voltage increases the heat transfer, but this enhancement in heat transfer is confined to a limited region.

To examine the effect of pin number, flow fields for different configurations of electrode pins with Re = 200 at an applied voltage of 24 kV are shown in Fig. 4.23. The

case with 0 electrode pin refers to the channel flow with no electric field, which is the same as Fig. 4.16 (a) and has been discussed earlier. With the same applied voltage, the configuration with fewer pins produces a higher electric intensity at the electrode tips. As seen from Fig. 4.23, the configuration with 4 electrode pins has the largest effect on the velocity profile inside the channel. For the configurations with 12 and 28 electrode pins, the familiar parabolic velocity profile gradually recovers at the core region below the electrode tips. As seen in Fig. 4.23 (b), the high velocity close to the wall results in a lower velocity region at the center, and this high speed stream turns away from the channel wall while developing downwards. Additional velocity contour plots at various cross-sections along with three-dimensional surface plots can be found in the Appendix.

The corresponding temperature fields are shown in Fig. 4.24. No significant change is observed in the temperature field for all configurations when an electric field is applied. Although the flow field is modified by the electric field, this modification is either limited to a small region near the electrode tips or away from the channel wall, and hence has no obvious effect on the development of thermal boundary layer downstream. This can be further verified from the distribution of local Nusselt number along the length of the channel, which is shown in Fig. 4.25. When an electric field is applied, the local Nusselt number is shifted upwards slightly, and this upward shifting occurs in the region upstream of $\bar{z} = 1.5$. The number of electrode pins makes no significant influence on the heat transfer result at Re = 200 for an applied voltage of 24 kV.

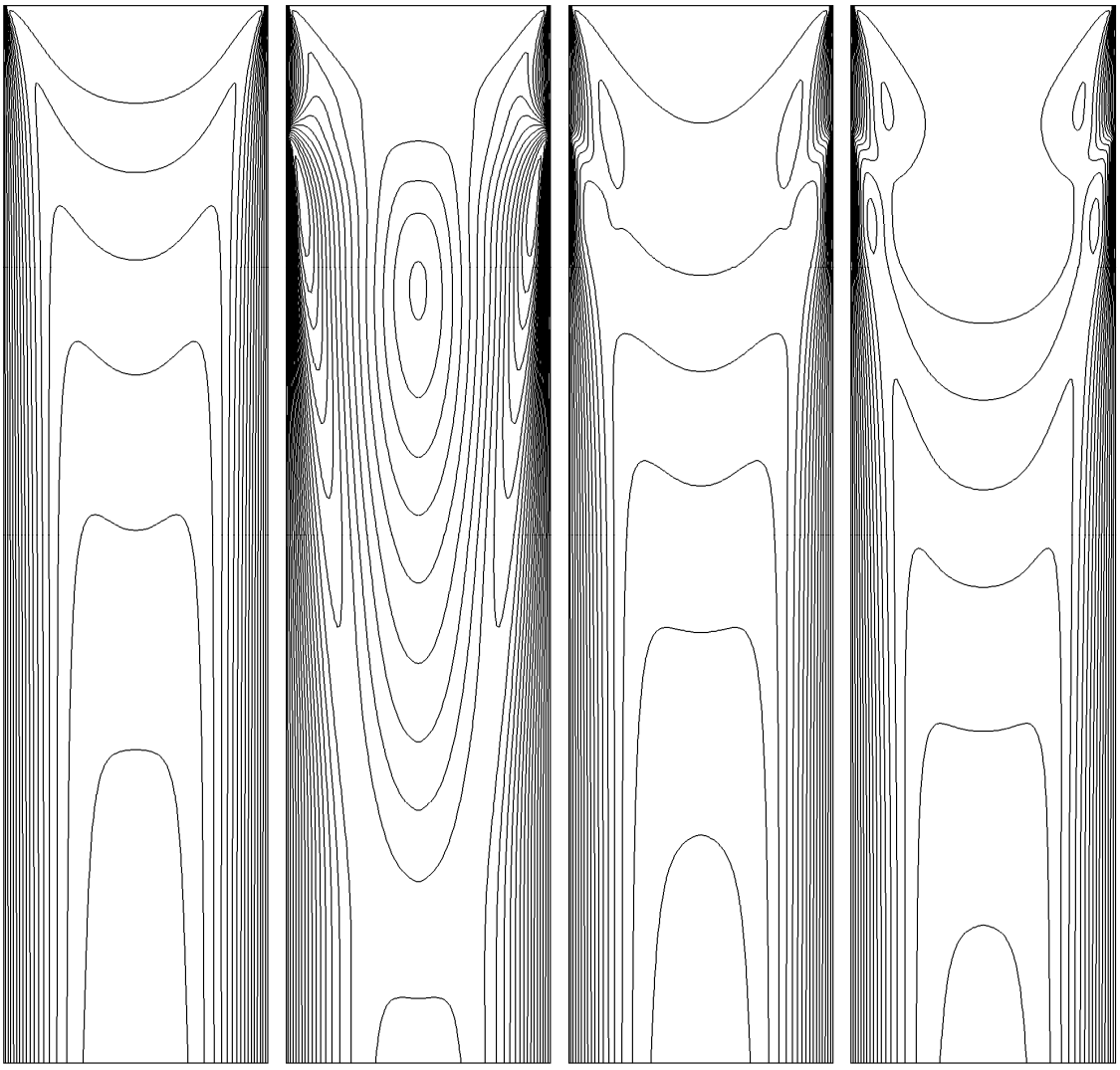

Figure 4.23 Flow field for forced convection with Re = 200 at V_0 = 24 kV ($\bar{x}$ = 1/2, $\Delta\overline{w}$ = 0.1) (a) 0 pins, (b) 4 pins, (c) 12 pins, (d) 28 pins

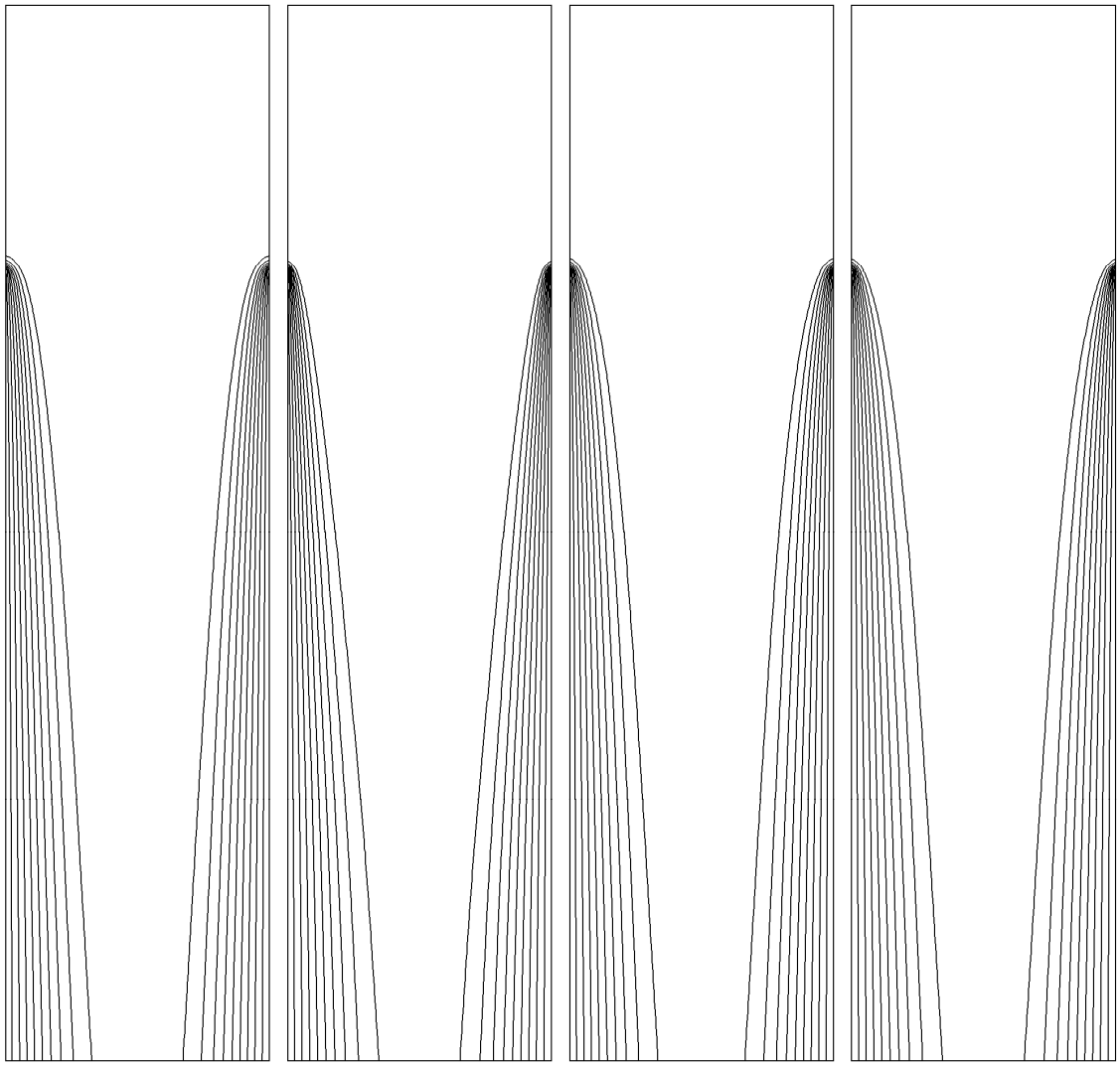

Figure 4.24 Temperature field for forced convection with Re = 200 at V_0 = 24 kV ($\bar{x} = 1/2,\ \Delta\theta = 0.1$) (a) 0 pins, (b) 4 pins, (c) 12 pins, (d) 28 pins

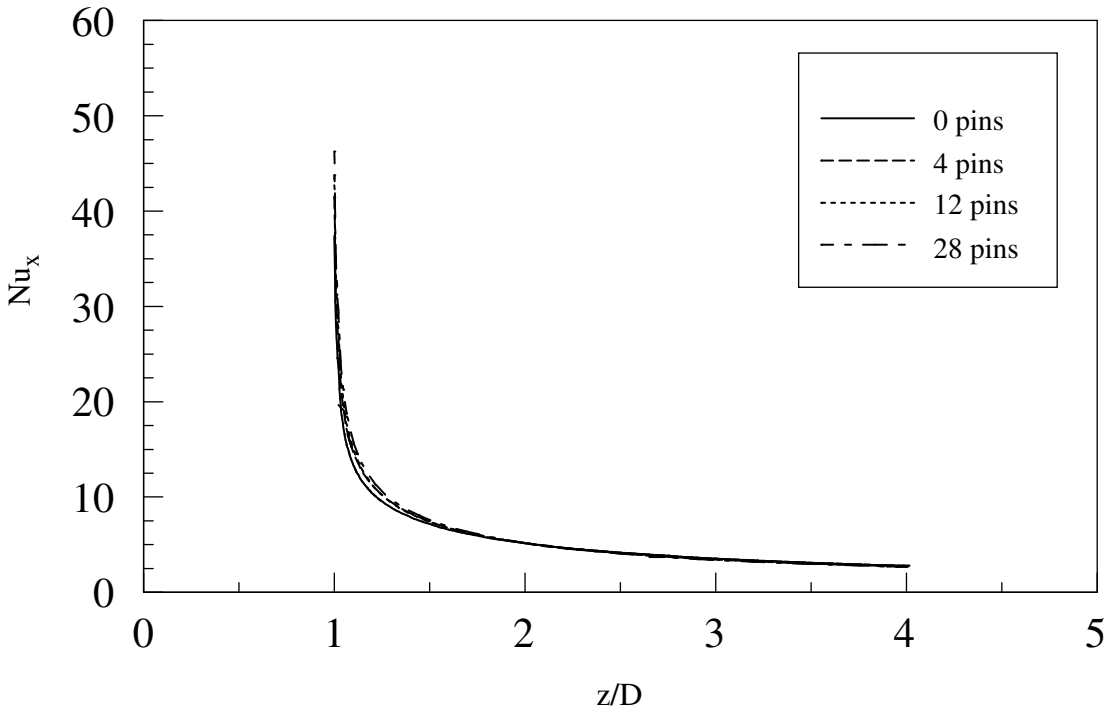

Figure 4.25 Variation of local Nusselt number (Re = 200, V_0 = 24 kV)

To investigate the effect of inlet flow velocity on the heat transfer, the variation of local Nusselt number at various Reynolds numbers is shown in Fig. 4.26 for the configuration with 12 pins at an applied voltage of 28 kV. It should be mentioned that similar trends have been observed for other Reynolds numbers and therefore they are not repeated here for brevity. Starting with a large value, the local Nusselt number decreases significantly in the flow direction and approaches the fully-developed value. A higher Reynolds number results in a larger starting value of the local Nusselt number. Also, when the Reynolds number increases, the curve shifts upwards, leading to a larger Nusselt number at the entrance region. This is consistent with one's expectation that flows with a higher Reynolds number produces a better heat transfer result.

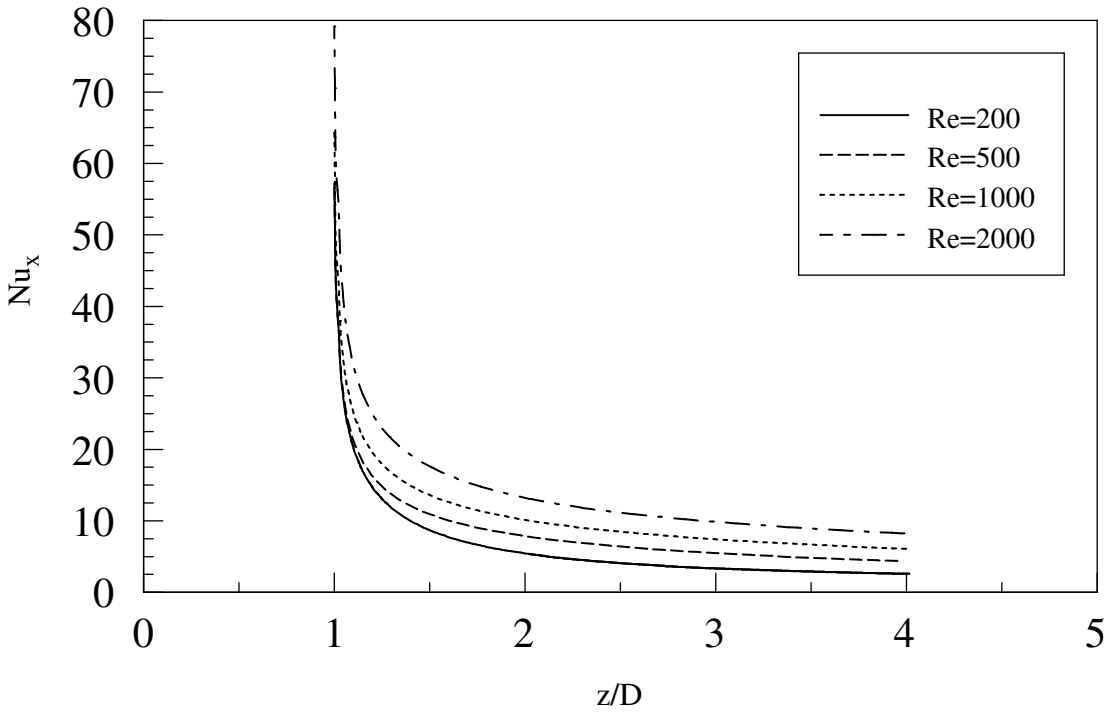

Figure 4.26 Variation of local Nusselt number (12 pins, V_0 = 28 kV)

For the present study, it is more interesting to evaluate the heat transfer enhancement by an electric field. In Fig. 4.27, the variation of local Nusselt number at various Reynolds numbers for the configuration with 12 electrode pins at V_0 = 28 kV is normalized with the value of forced convection alone, Nu_{x0}. This value, Nu_x/Nu_{x0}, represents the heat transfer enhancement by the application of an electric field. For Re = 200, the local heat transfer enhancement as high as 58% ($Nu_x / Nu_{x0} = 1.58$) is observed to occur at the leading edge of the thermal boundary layer. However, this enhancement decreases rapidly in the flow direction. At the downstream further than $z/D = 2.3$, the ratio of local Nusselt numbers becomes less than unity. For higher Reynolds numbers, i.e., Re = 500, 1000, and 2000, a good amount of heat transfer enhancement is also achieved in the leading edge of thermal boundary layer. Although this enhancement

becomes less significant downstream, the ratio of local Nusselt numbers remains above unity.

It may be useful to consider the EHD number, N_{EHD}, for a better understanding of Fig. 4.27. Recalling the definition of the EHD number, which represents the ratio of electric body force to flow inertia. For the configuration of 12 electrode pins at an applied voltage of 28 kV, the EHD numbers are calculated to be 5420, 867, 216, and 54 for Reynolds numbers of 200, 500, 1000, and 2000, respectively. At a low Reynolds number, say 200, the electric field has a large influence on the flow field, thus greatly enhancing heat transfer. At a higher Reynolds number, the secondary flow produced by the electric field is suppressed by the overwhelming influence of the primary flow, thus diminishing the heat transfer enhancement.

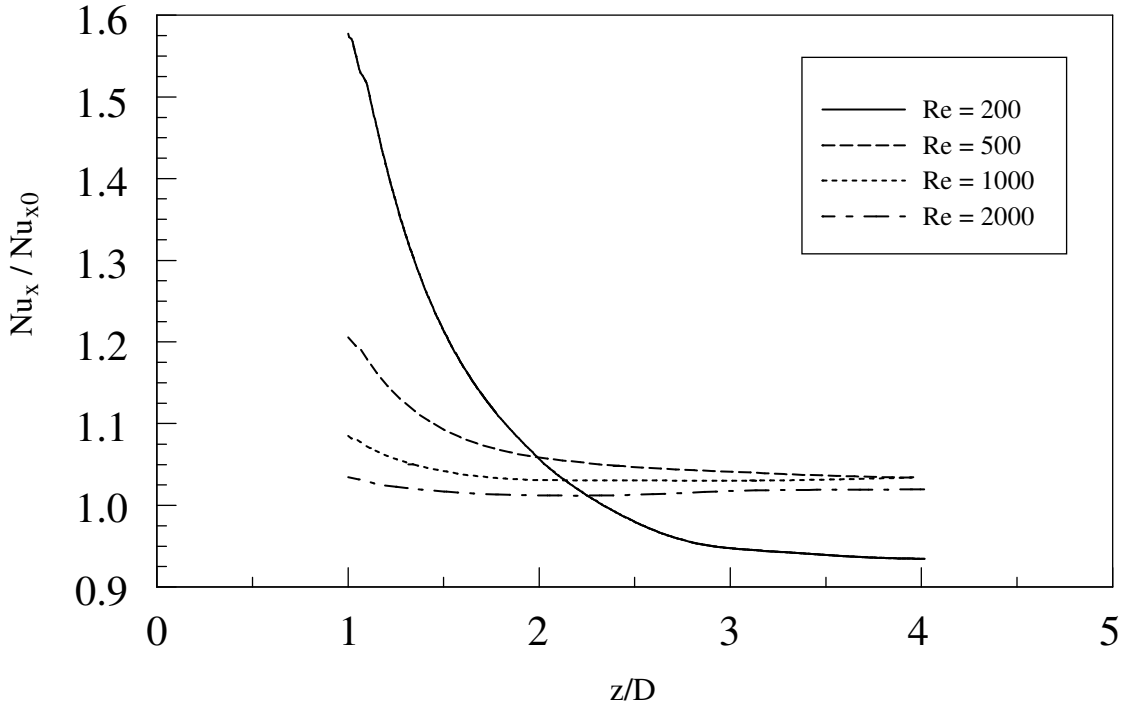

Figure 4.27 Variation of local Nusselt number (12 pins, V_0 = 28 kV)

Figure 4.28 shows the variation of average Nusselt number as a function of the Reynolds number for the configuration of 12 electrode pins at various applied voltages. Again, the average Nusselt number is normalized by the value of forced convection alone, thus it represent the average heat transfer enhancement. At a given applied voltage, the heat transfer enhancement by the electric field decreases with an increase in the Reynolds number, as explained earlier. This Reynolds number dependency is a well-known trend in the field of heat transfer enhancement by corona wind [10-11]. It is also noticed that a higher applied voltage produces better heat transfer enhancement. Although local Nusselt number can be increased as high as 58% at the applied voltage of 28 kV with Re = 200 (Fig. 4.27), the average Nusselt number for this case is only increased by 15%.

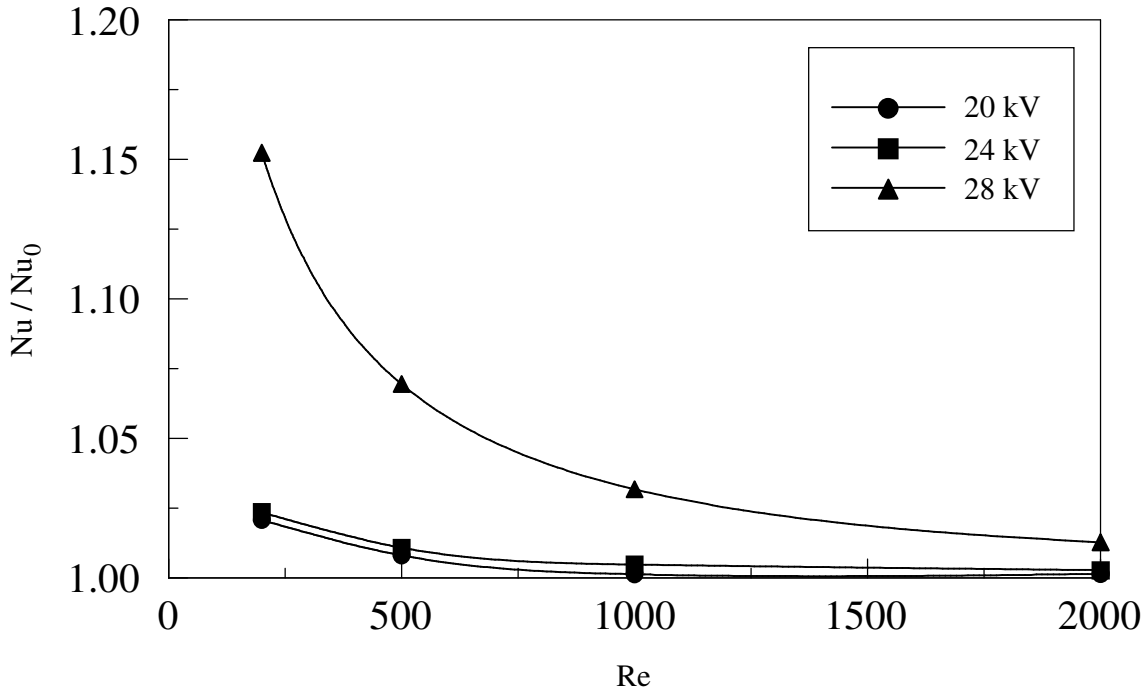

Figure 4.28 Average Nusselt number vs. Reynolds number (12 pins)

To examine the effect of the electrode pin number, the normalized average Nusselt numbers for three electrode configurations at an applied voltage of 24 kV are shown in Fig. 4.29 as a function of Reynolds number. As observed, the effect of electrode pin number on the heat transfer enhancement is more pronounced at low Reynolds numbers than that at high Reynolds numbers. The configuration with 28 pins produces the best heat transfer enhancement among all three configurations. As the Reynolds number increases, the effect of electric field on the heat transfer enhancement is suppressed by the flow inertia of the primary flow, resulting in little to no distinction among various pin numbers considered. Therefore, one can conclude that more electrode pins produce better results in the heat transfer enhancement, particularly in the low Reynolds numbers flow regime.

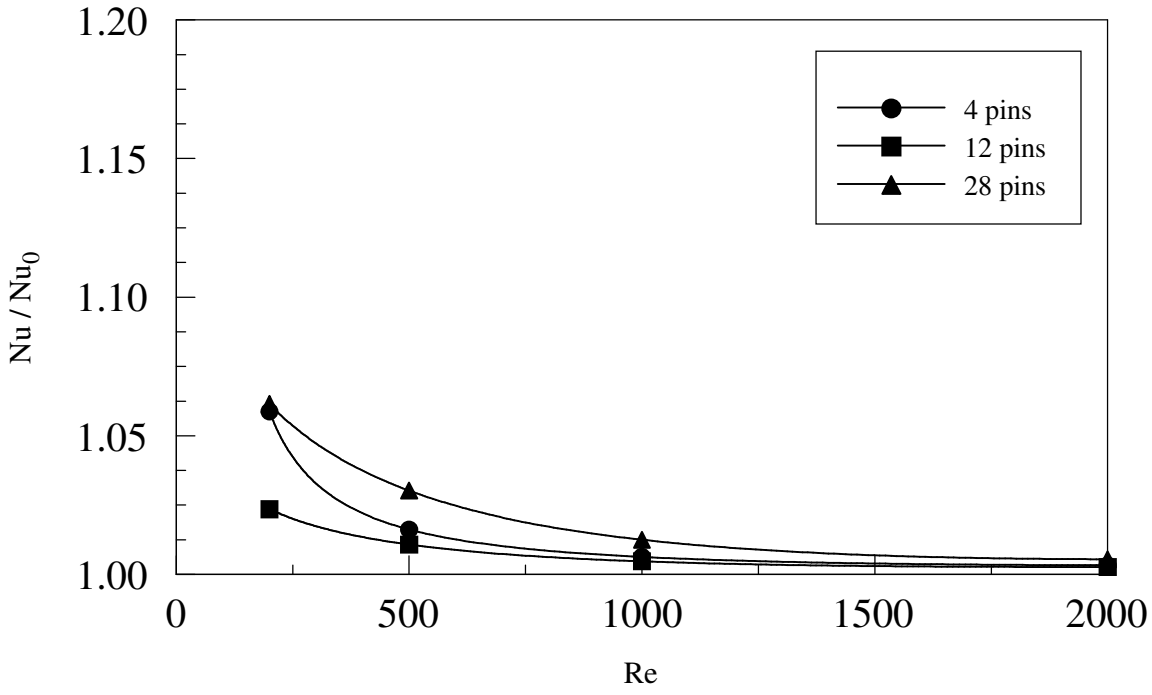

Figure 4.29 Average Nusselt number vs. Reynolds number (V_0 = 24 kV)

To investigate the penalty (i.e., the increased pressure drop) which may be imposed by the EHD-induced flows, the friction factors as a function of Reynolds number is depicted in Fig. 4.30 for three electrode configurations at various applied voltages. The friction factor is normalized by the value of forced convection alone to show the effect of electric field. As seen from Fig. 4.30, the ratios of friction factors are all less than unity, which indicates that the pressure drop for a normal channel flow is actually reduced by the application of electric field. This can be attributed to the effect of entrainment brought about by the corona wind. Thus, the amount of work required from an external fan/pump is reduced. Moreover, for a given electrode configuration, a higher applied voltage produces a stronger corona jet stream (and thus a larger amount of entrained flow), resulting in a lower ratio of the friction factors. At a given applied

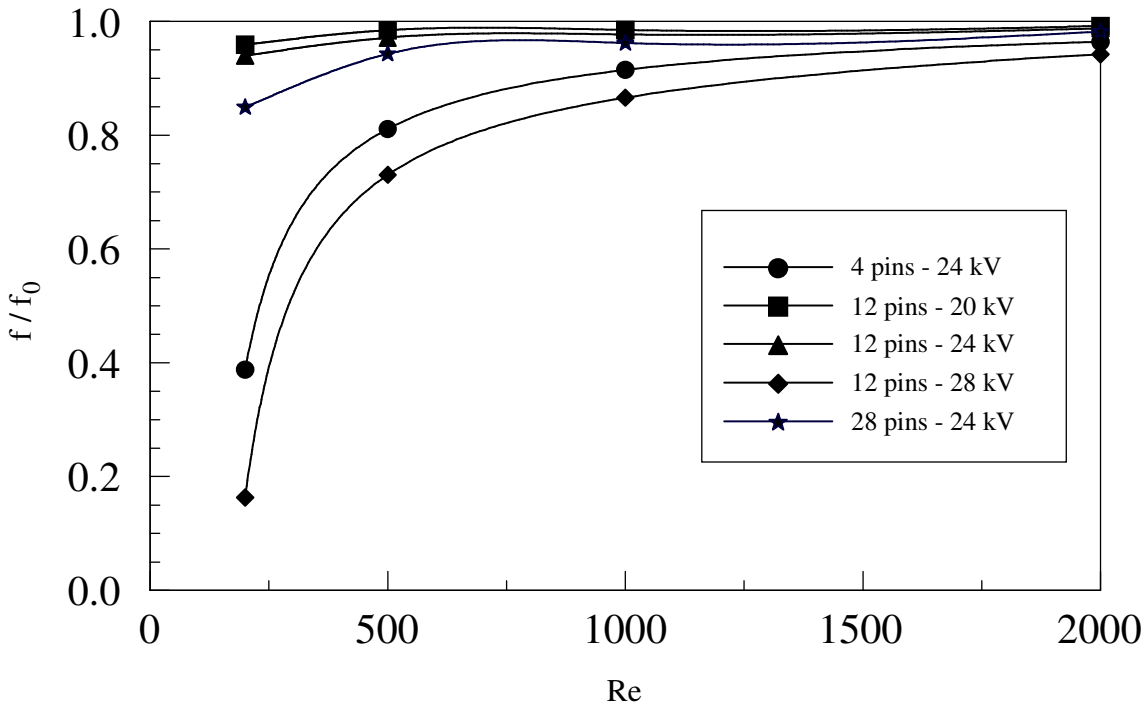

Figure 4.30 Friction factor vs. Reynolds number

voltage, the configuration with 4 electrode pins has the lowest friction factor ratio, followed in order by 28 pins and 12 pins. This is consistent with the experimental results (Fig. 2.13) that show 4-pin configuration produces the highest volume flow rate. Lastly, but not the least, friction factor ratios approach unity as the Reynolds number increases. This is due to the fact that the effect of electric field is undermined by the influence of the primary flow at higher Reynolds numbers.

The ratio of the Nusselt number to the friction factor is used to evaluate the thermal hydraulic performance. Figure 4.31 shows the evaluation of this parameter for three electrode configurations at various applied voltages. From earlier discussions, the configuration with 12 pins at the applied voltage of 28 kV produces the best heat transfer enhancement and the least pressure drop, hence, resulting in the best thermal hydraulic performance. However, the performance for this configuration at lower applied voltages (i.e., 20 kV and 24 kV) is nearly the same, which remains relatively low for all Reynolds numbers considered. At the applied voltage of 24 kV, the configuration with 4 pins has a better thermal hydraulic performance than those with 12 pins and 28 pins. Also observed, the flow with low Reynolds number has a better performance than that with high Reynolds number. Most importantly, Fig. 4.31 shows that the values of $(Nu / Nu_0) / (f / f_0)$ are all greater than unity. Since this parameter for most heat transfer enhancement techniques has a value generally less than unity [12], the EHD technique is thus very promising, particularly for flows with low Reynolds numbers.

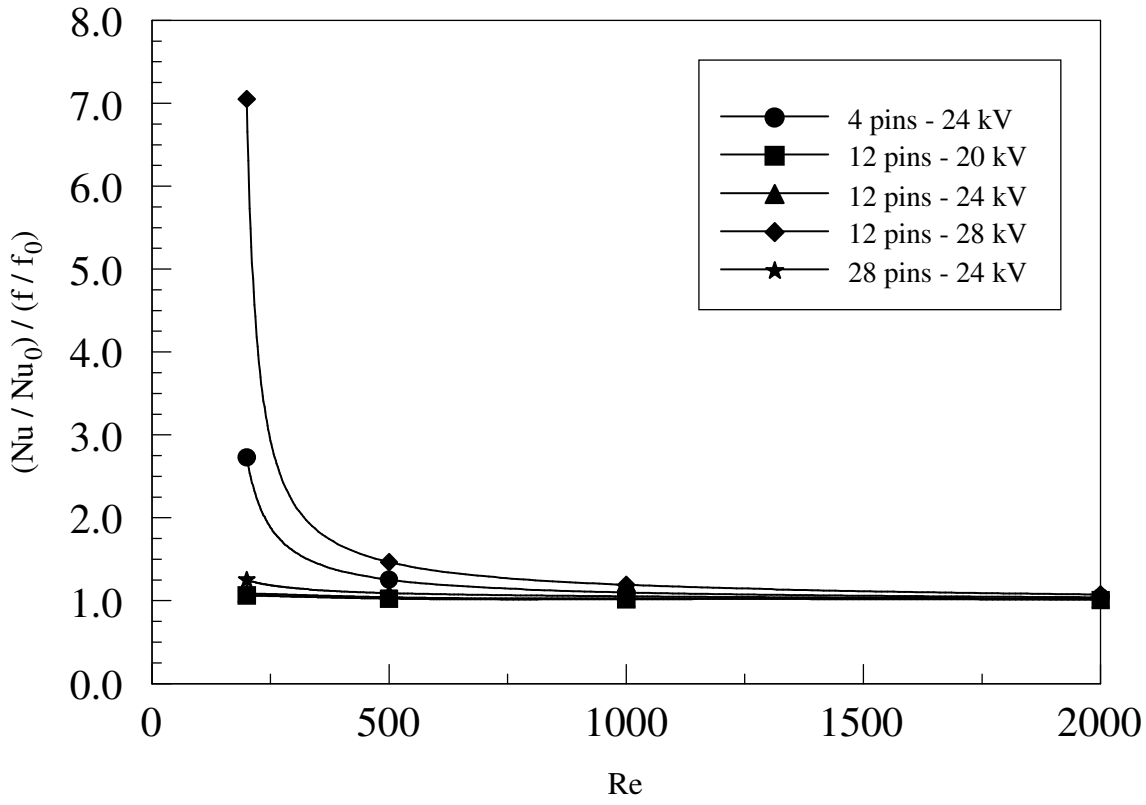

Figure 4.31 Evaluation of thermal hydraulic performance

CHAPTER FIVE

CONCLUSIONS AND FUTURE WORK

Electrohydrodynamic (EHD) flows have a great potential for a wide range of engineering applications. The present study has focused on the EHD-induced flows in a square channel with different electrode configurations. Experimental results provide important information for the optimal design of an EHD gas pump. Numerical methods have been employed to investigate the influence of corona wind on forced convection and its effectiveness in the heat transfer enhancement.

5.1 Experimental Study

Experiments have been performed for an EHD gas pump with three electrode configurations. The results show that corona current undergoes an initial transient phase before reaching a stable value. The corona wind velocity fluctuates around an average value, and this fluctuation reduces as the applied voltage increases. Since the electrode pins are mounted on the inner surface of the channel wall, corona wind issued from the electrodes behaves like a set of wall jets, resulting in a parabolic velocity profile at the center of the channel with the maximum velocity close to the channel wall. It is this flow characteristic that has the potential to alter the boundary layer and improve the heat transfer coefficient. At low applied voltages, negative corona discharge produces higher velocity and volume flow rate than those of positive one. However, this trend is reversed at high applied voltages. The EHD gas pump with 4 electrode pins induces more air flow than that with 12 or 28 pins at low applied voltages. However, as the applied voltage increases, the configurations with more electrode pins produce a higher volume flow rate.

Therefore, depending on the application, an appropriate configuration and applied voltage can be selected to achieve the desired outcome. For example, if a low volume flow rate is required, an EHD gas pump with a low number of electrode pins can be used at a low applied voltage with negative polarity. If a large volume flow rate is desired, an EHD gas pump with high number of electrode pins should be used at a high applied voltage with positive polarity. In addition, as far as the performance is concerned, it has been shown that the EHD gas pump proposed is more effective than most conventional fans.

5.2 Numerical Study

Numerical simulations have been carried out for the EHD gas pump based on the experimental model. The electric potential and space charge distributions have been visually examined for three electrode configurations at various applied voltages. Numerical results of the EHD-induced flows were compared with the experimental data, and a good agreement was found. Flow visualizations from numerical results reveal that corona wind issued from the electrodes behaves like a set of wall jets, leading to high velocity gradients near the channel walls. With forced convection, it is found that the electric field accelerates the fluid flow close to the wall, which reduces the boundary layer thickness and, in turn, increases the heat transfer coefficient. This influence of the electric field is more pronounced in the low Reynolds number flow regime. At high Reynolds numbers, the electric field effect is suppressed by the primary flow. In this study, the local Nusselt number can be increased as high as 58% at Re = 200 with the configuration of 12 electrode pins at an applied voltage of 28 kV, whereas the average Nusselt number in this case is only increased by 15%. In addition, it has been shown that

the thermal hydraulic performance parameter, $(Nu / Nu_0) / (f / f_0)$, is always greater than unity. Since the values of this parameter for most heat transfer enhancement techniques are generally less than unity, thus this EHD enhancement technique has shown great promise.

5.3 Recommended Future Work

The current study has successfully revealed the characteristics of an EHD-induced flow in a square channel both experimentally and numerically, as well as its influence on heat transfer. However, several improvements can be considered for the future study.

In the current experimental study, the air velocity inside the channel is measured by inserting a hot wire anemometer through the compression fittings on the wall. However, the diameter of the probe which is inserted into the flow is relatively large, which can disturb or partially block the flow. Thus, a velocity measuring device with a smaller diameter is recommended for the future study so that the uncertainty of velocity measurements can be greatly reduced. In addition, only nine velocity sampling points are used at each cross-section to examine the velocity profile and calculate the volume flow rate inside the channel. It is expected that more sampling points will produce more accurate results. Since the electrodes are flush mounted on the channel wall, sampling points close to the wall are especially preferred to capture the high speed flows. Last, but not the least, the current study evaluates various configurations of an EHD gas pump in terms of its number of electrode pins. Other factors, such as the electrode diameters and the spacing between the electrodes and the grounded plate, can also be considered for the optimal design of an EHD gas pump.

Numerical simulations have shown that the increase in the local Nusselt number mostly occurs at the region close to the electrodes. Further downstream, the fluid accelerated by the electric body force turns away from the channel wall, resulting in little influence on the boundary layer. One approach that could potentially solve this problem is to extend the grounded plate downward to the end of the channel. It is speculated that the accelerated fluid flow will remain close to the channel wall, causing a greater disturbance to the boundary layer and increasing the overall heat transfer effect.

REFERENCES

[1] M. Robinson, "Movement of air in the electric wind of the corona discharge," *Transactions of the American Institute of Electrical and Electronic Engineers,* vol. 80, pp. 143-150, 1961.

[2] F. C. Lai and K. W. Lai, "EHD-enhanced drying with wire electrode," *Drying Technology,* vol. 20, pp. 1393-1405, 2002.

[3] A. Alem-Rajabi and F. C. Lai, "EHD-enhanced drying of partially wetted glass beads," *Drying Technology,* vol. 23, pp. 597-609, 2005.

[4] T. I. J. Goodenough, P. W. Goodenough, and S. M. Goodenough, "The efficiency of corona wind drying and its application to the food industry," *Journal of Food Engineering,* vol. 80, pp. 1233-1238, 2007.

[5] L. Leger, E. Moreau, G. Artana, and G. Touchard, "Influence of a DC corona discharge on the airflow along an inclined flat plate," *Journal of Electrostatics,* vol. 51, pp. 300-306, 2001.

[6] R. Vilela Mendes and J. Dente, "Boundary-layer control by electric fields: A feasibility study," *Journal of Fluids Engineering-Transactions of the ASME,* vol. 120, pp. 626-629, 1997.

[7] E. Moreau, G. Artana, and G. Touchard, "Surface corona discharge along an insulating flat plate in air applied to electrohydrodynamically airflow control: electrical properties," *Electrostatics Conference*, vol. 178, pp. 285-290, 2004.

[8] E. Moreau, L. Léger, and G. Touchard, "Effect of a DC surface-corona discharge on a flat plate boundary layer for air flow velocity up to 25 m/s," *Journal of Electrostatics,* vol. 64, pp. 215-225, 2006.

[9] P. Magnier, D. Hong, A. Leroy-Chesneau, J. M. Pouvesle, and J. Hureaua, "A DC corona discharge on a flat plate to induce air movement," *Journal of Electrostatics,* vol. 65, pp. 655-659, 2007.

[10] M. M. Ohadi, D. A. Nelson, and S. Zia, "Heat-transfer enhancement of laminar and turbulent pipe-flow via corona discharge," *International Journal of Heat and Mass Transfer,* vol. 34, pp. 1175-1187, 1991.

[11] M. Molki, M. M. Ohadi, B. Baumgarten, M. Hasegawa, and A. Yabe, "Heat transfer enhancement of airflow in a channel using corona discharge," *Journal of Enhanced Heat Transfer,* vol. 7, pp. 411-425, 2000.

[12] M. Molki and P. Damronglerd, "Electrohydrodynamic enhancement of heat transfer for developing air flow in square ducts," *Heat Transfer Engineering,* vol. 27, pp. 35-45, 2006.

[13] T. Yamamoto and H. R. Velkoff, "Electrohydrodynamics in an electrostatic precipitator," *Journal of Fluid Mechanics,* vol. 108, pp. 1-18, 1981.

[14] A. Richter, A. Plettner, K. A. Hofmann, and H. Sandmaier, "A micromachined electrohydrodynamic (EHD) pump," *Sensors and Actuators a-Physical,* vol. 29, pp. 159-168, 1991.

[15] N. Jewell-Larsen, "Optimization and miniaturization of electrostatic air pumps for thermal management," M.S. Thesis, University of Washington, 2004.

[16] L. Tanasomwang and F. Lai, "Long-term ozone generation from electrostatic air cleaners," *Conference Records of the 1997 IEEE Industry Applications Society 32nd IAS Annual Meeting*, vol. 3, pp. 2037-2044, 1997.

[17] L. Fouad and S. Elhazek, "Effect of humidity on positive corona discharge in a 3-electrode system," *Journal of Electrostatics,* vol. 35, pp. 21-30, 1995.

[18] M. Goldman, A. Goldman, and R. S. Sigmond, "The corona discharge, Its properties and specific uses," *Pure and Applied Chemistry,* vol. 57, pp. 1353-1362, 1985.

[19] M. Rickard, D. Dunn-Rankin, F. Weinberg, and F. Carleton, "Characterization of ionic wind velocity," *Journal of Electrostatics,* vol. 63, pp. 711-716, 2005.

[20] J. S. Chang, D. Brocilo, K. Urashima, J. Dekowski, J. Podlinski, J. Mizeraczyk, and G. Touchard, "On-set of EHD turbulence for cylinder in cross flow under corona discharges," *Journal of Electrostatics,* vol. 64, pp. 569-573, 2006.

[21] H. Tsubonea, J. Ueno, B. Komeili, S. Minami, G. D. Harvel, K. Urashima, C. Y. Ching, and J. S. Chang, "Flow characteristics of wire-non-parallel plate electrohydrodynamic gas pumps," *Journal of Electrostatics,* vol. 66, pp. 115-121, 2008.

[22] J. S. Chang, H. Tsubone, Y. N. Chun, A. A. Berezin, and K. Urashima, "Mechanism of electrohydrodynamically induced flow in a wire-non-parallel plate electrode type gas pump," *Journal of Electrostatics,* vol. 67, pp. 335-339, 2009.

[23] B. Komeili, J. S. Chang, G. D. Harvel, C. Y. Ching, and D. Brocilo, "Flow characteristics of wire-rod type electrohydrodynamic gas pump under negative corona operations," *Journal of Electrostatics,* vol. 66, pp. 342-353, 2008.

[24] N. Takeuchi, K. Yasuoka, and J. S. Chang, "Effect of discharge electrode parameters on the flow velocity profile of the wire-rod type electrohydrodynamic gas pump exit," *IEEE Transactions on Dielectrics and Electrical Insulation,* vol. 16, pp. 615-621, 2009.

[25] E. Moreau and G. Touchard, "Enhancing the mechanical efficiency of electric wind in corona discharges," *Journal of Electrostatics,* vol. 66, pp. 39-44, 2008.

[26] M. Robinson, "Convective heat transfer at surface of a corona electrode," *International Journal of Heat and Mass Transfer,* vol. 13, pp. 263-274, 1970.

[27] H. Velkoff, "Investigation of the effects of electrostatic fields on heat transfer and boundarylasers," in *Technical Documentary Report ASD-TDR-62-650*, Wright-Patterson Air Force Base, Ohio, 1962.

[28] H. Kalman and E. Sher, "Enhancement of heat transfer by means of a corona wind created by a wire electrode and confined wings assembly," *Applied Thermal Engineering,* vol. 21, pp. 265-282, 2001.

[29] D. Go, R. Maturana, T. Fisher, and S. Garimella, "Enhancement of external forced convection by ionic wind," *International Journal of Heat and Mass Transfer,* vol. 51, pp. 6047-6053, 2008.

[30] D. Go, S. Garimella, T. Fisher, and R. Mongia, "Ionic winds for locally enhanced cooling," *Journal of Applied Physics,* vol. 102, p. 053302, 2007.

[31] J. Chang, F. Pontiga, P. Atten, and A. Castellanos, "Corona discharge characteristics of narrow coaxial wire-pipe discharge tubes with gas flow," *IEEE Transactions on Industry Applications*, vol. 32, pp. 1887-1887, 1993.

[32] J. Chang, F. Pontiga, P. Atten, and A. Castellanos, "Hysteresis effect of corona discharge in a narrow coaxial wire-pipedischarge tube with gas flow," *IEEE Transactions on Industry Applications,* vol. 32, pp. 1250-1256, 1996.

[33] M. Molki and K. L. Bhamidipati, "Enhancement of convective heat transfer in the developing region of circular tubes using corona wind," *International Journal of Heat and Mass Transfer,* vol. 47, pp. 4301-4314, 2004.

[34] A. Shooshtari, M. Ohadi, and F. Franca, "Experimental and numerical analysis of electrohydrodynamic enhancement of heat transfer in air laminar channel flow," *19th IEEE SEMI-THERM Symposium*, pp. 48-52, 2003.

[35] S. O. Ahmedou and M. Havet, "Analysis of the EHD enhancement of heat transfer in a flat duct," *IEEE Transactions on Dielectrics and Electrical Insulation,* vol. 16, pp. 489-494, 2009.

[36] F. C. Lai, P. J. McKinney, and J. H. Davidson, "Oscillatory electrohydrodynamic gas flows," *Journal of Fluids Engineering,* vol. 117, pp. 491-497, 1995.

[37] F. C. Lai and J. Mathew, "Heat transfer enhancement by EHD-induced oscillatory flows," *Journal of Heat Transfer*, vol. 128, pp. 861-869, 2006.

[38] F. C. Lai and K. Tay, "Electrohydrodynamically-Enhanced Forced Convection in a Horizontal Channel with Oscillatory Flows," *Heat Transfer Engineering,* vol. 31, pp. 147-156, 2010.

[39] L. Leger, E. Moreau, and G. Touchard, "Electrohydrodynamic airflow control along a flat plate by a DC surface corona discharge—velocity profile and wall pressure measurements," *1st AIAA Flow Control Conference,* pp. 2002-2833, 2002.

[40] Y. N. Chun, J. S. Chang, A. A. Berezin, and J. Mizeraczyk, "Numerical modeling of near corona wire electrohydrodynamic flow in a wire-plate electrostatic precipitator," *IEEE Transactions on Dielectrics and Electrical Insulation,* vol. 14, pp. 119-124, 2007.

[41] T. Yamamoto, Y. Morita, H. Fujishima, and M. Okubo, "Three-dimensional EHD simulation for point corona electrostatic precipitator based on laminar and turbulent models," *Journal of Electrostatics,* vol. 64, pp. 628-633, 2006.

[42] R. Moss and J. Grey, "Heat transfer augmentation by steady and alternating electric fields," *Proc. 1966 Heat Transfer and Fluid Mechanics lnstitute, Stanford University Press, Stanford, California,* pp. 210-235, 1966.

[43] J. Chang, A. Kelly, and J. Crowley, *Handbook of Electrostatic Processes*, Marcel Dekker, New York, 1995.

[44] N. E. Jewell-Larsen, I. A. Krichtafovitch, and A. V. Mamishev, "Design and optimization of electrostatic fluid accelerators," *IEEE Transactions on Dielectrics and Electrical Insulation,* vol. 13, pp. 191-203, 2006.

[45] M. Huang and F. C. Lai, "Numerical study of EHD-enhanced forced convection using two-way coupling," *Journal of Heat Transfer,* vol. 125, pp. 760-764, 2003.

[46] F. C. Lai, "Effects of buoyancy on EHD-enhanced forced convection in a horizontal channel," *Journal of Thermophysics and Heat Transfer,* vol. 12, pp. 431-436, 1998.

[47] F. C. Lai and S. S. Kulkarni, "Effects of buoyancy on EHD-enhanced forced convection in a vertical channel," *Journal of Thermophysics and Heat Transfer,* vol. 21, pp. 730-735, 2007.

[48] M. Huang and F. C. Lai, "Effects of Joule heating on EHD-enhanced natural convection in an enclosure," *Journal of Thermophysics and Heat Transfer,* vol. 20, pp. 939-945, 2006.

[49] S. Patankar, *Numerical Heat Transfer and Fluid Flow*, Hemisphere Publishing Corporation, New York, 1980.

[50] *FLUENT 6.3 user's guide*, Fluent Inc., Lebanon, NH, 2006.

[51] S. Kline and F. McClintock, "Describing uncertainties in single-sample experiments," *Mechanical engineering,* vol. 75, pp. 3-8, 1953.

[52] R. J. Moffat, "Using uncertainty analysis in the planning of an experiment," *Journal of Fluids Engineering,* vol. 107, pp. 173-178, 1985.

[53] H. Coleman and W. Steele, *Experimentation and Uncertainty Analysis for Engineers*, 2nd ed., Wiley-Interscience, New York, 1999.

[54] J. H. Davidson and E. J. Shaughnessy, "Turbulence generation by electric body forces," *Experiments in Fluids,* vol. 4, pp. 17-26, 1986.

[55] Y. Cengel, *Heat Transfer: A Practical Approach*, 2nd ed., McGraw-Hill, New York, 2003.

[56] W. Kays, M. Crawford, and B. Weigand, *Convective Heat and Mass Transfer*, 3rd ed., McGraw-Hill, New York, 1993.

APPENDIX A

EXPERIMENTAL RESULTS

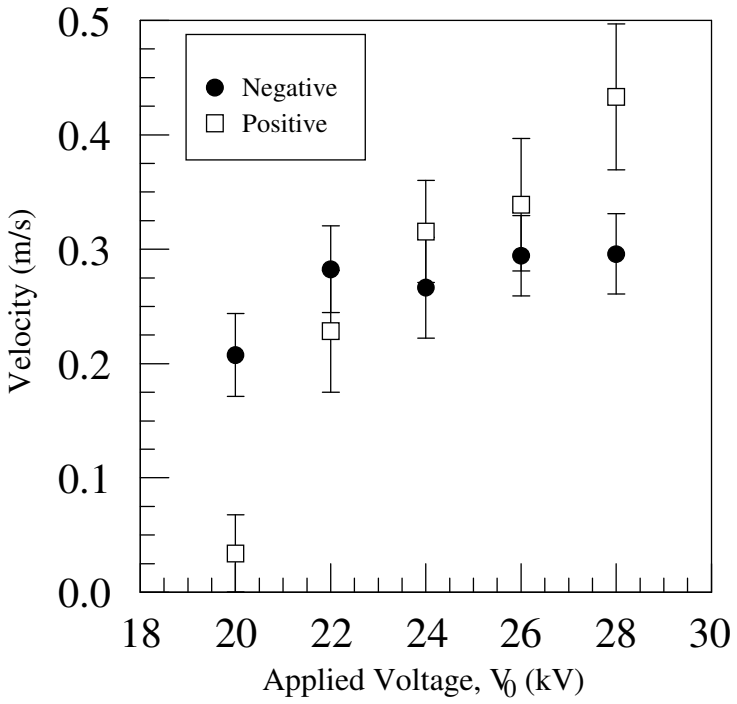

Figure A.1 Average velocity vs. applied voltage (4 pins)

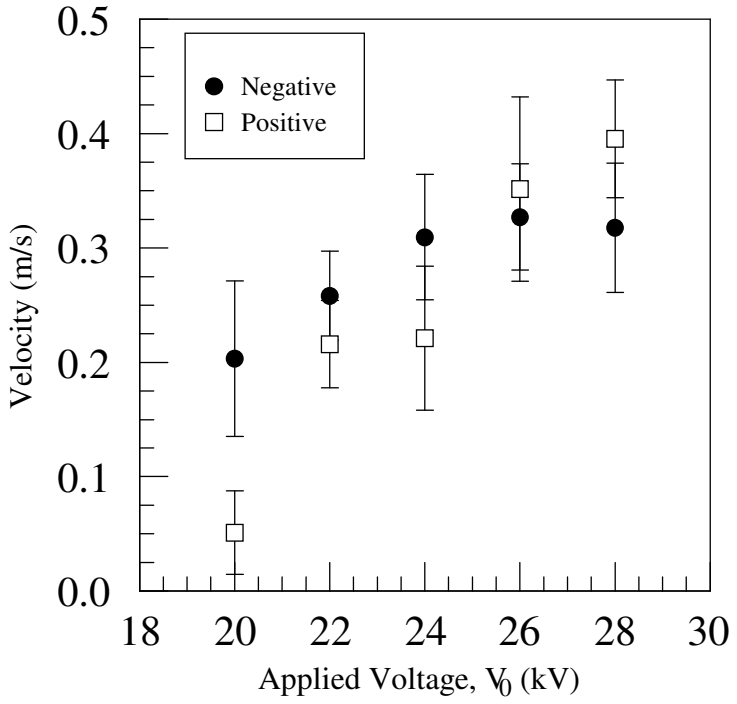

Figure A.2 Average velocity vs. applied voltage (12 pins)

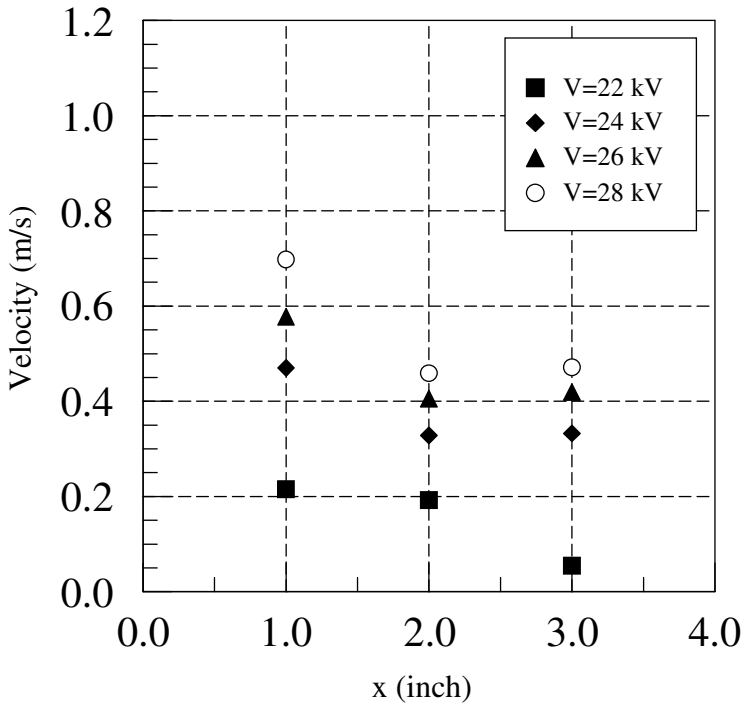

Figure A.3 Velocity profile inside channel, 28 pins, positive polarity (z=1 in.)

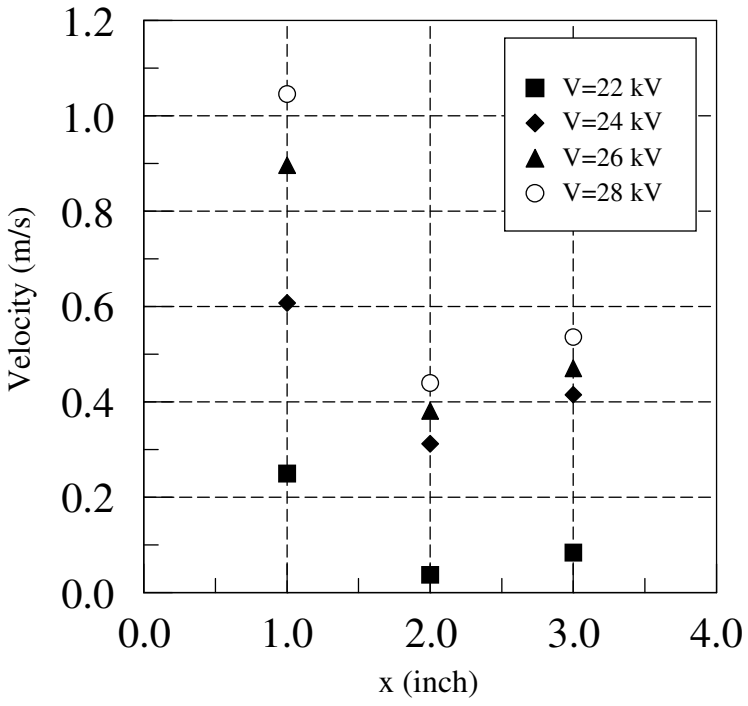

Figure A.4 Velocity profile inside channel, 28 pins, positive polarity (z=2.5 in.)

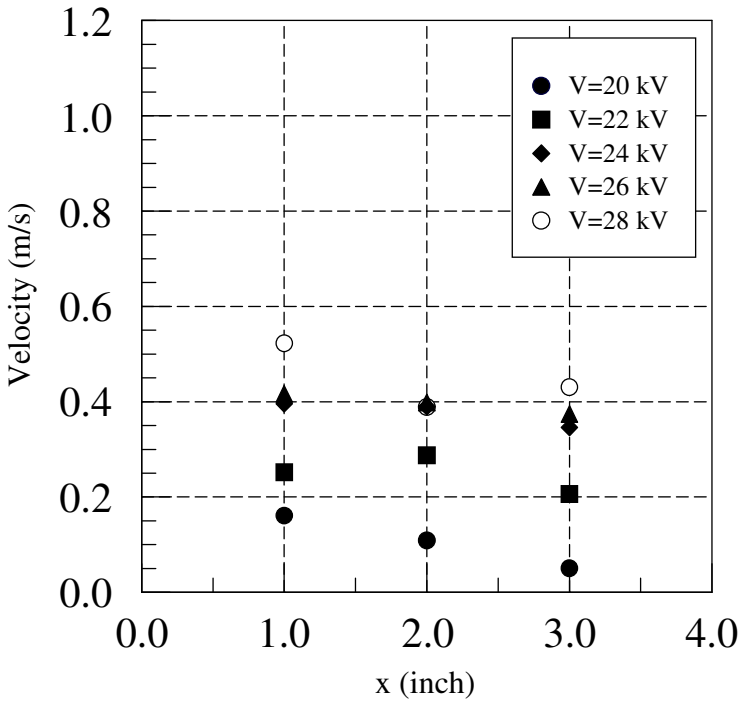

Figure A.5 Velocity profile inside channel, 28 pins, negative polarity (z=1 in.)

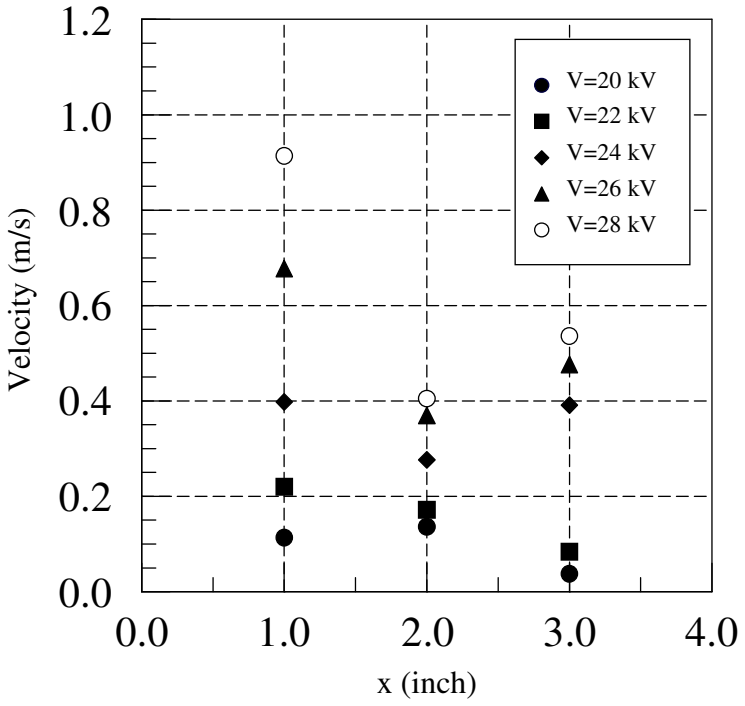

Figure A.6 Velocity profile inside channel, 28 pins, negative polarity (z=2.5 in.)

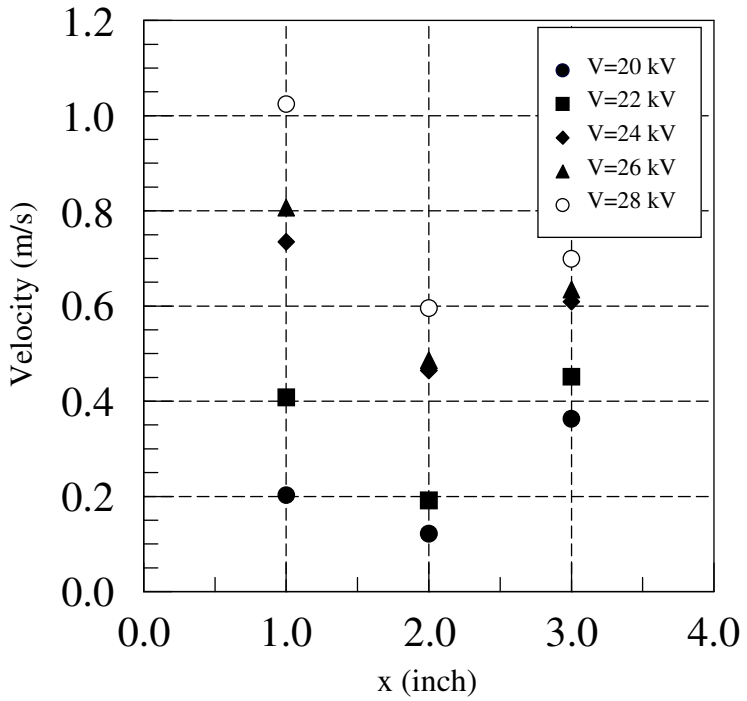

Figure A.7 Velocity profile inside channel, 28 pins, negative polarity (z=4 in.)

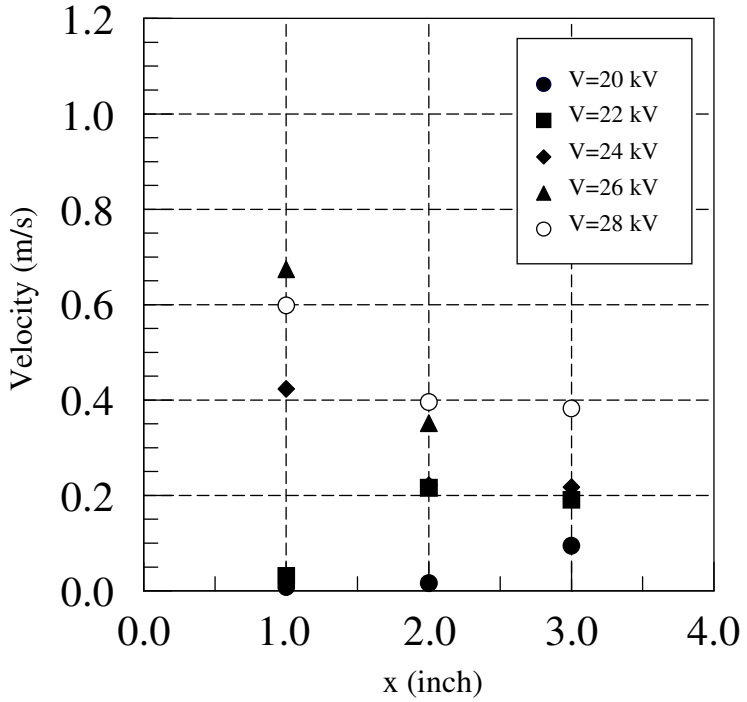

Figure A.8 Velocity profile inside channel, 12 pins, positive polarity (z=1 in.)

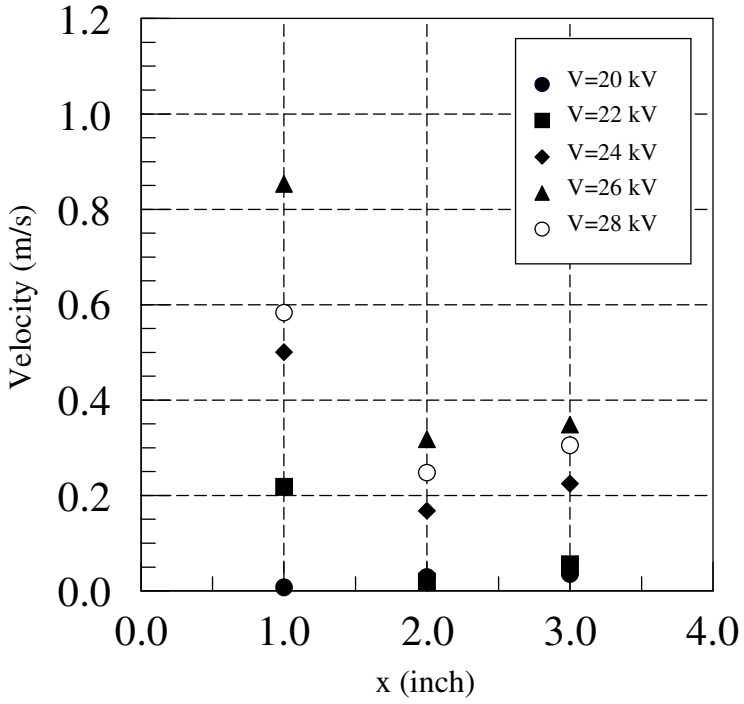

Figure A.9 Velocity profile inside channel, 12 pins, positive polarity (z=2.5 in.)

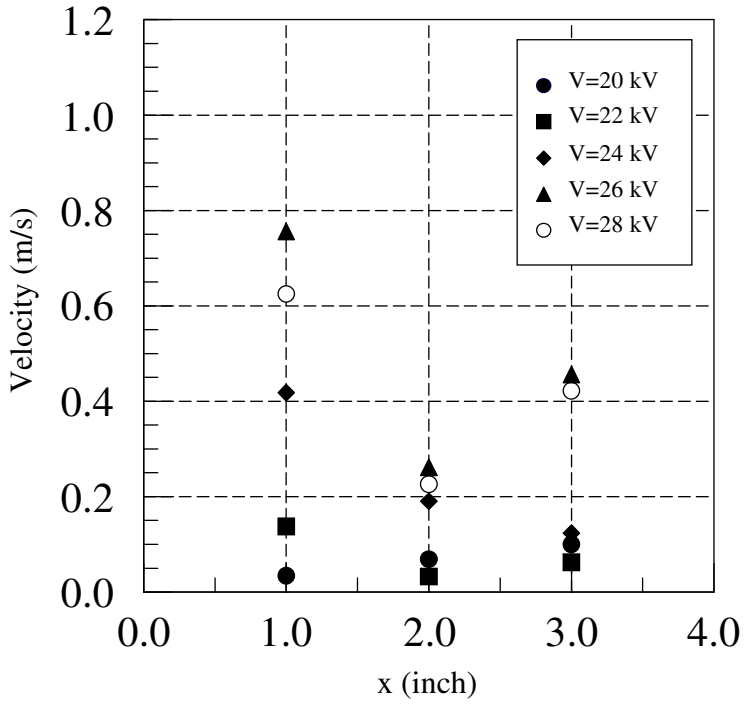

Figure A.10 Velocity profile inside channel, 12 pins, positive polarity (z=4 in.)

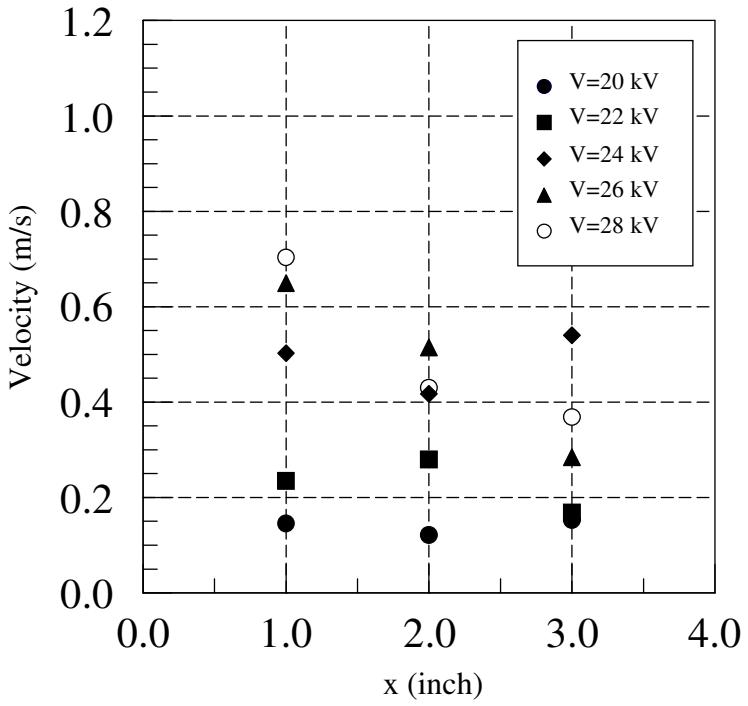

Figure A.11 Velocity profile inside channel, 12 pins, negative polarity (z=1 in.)

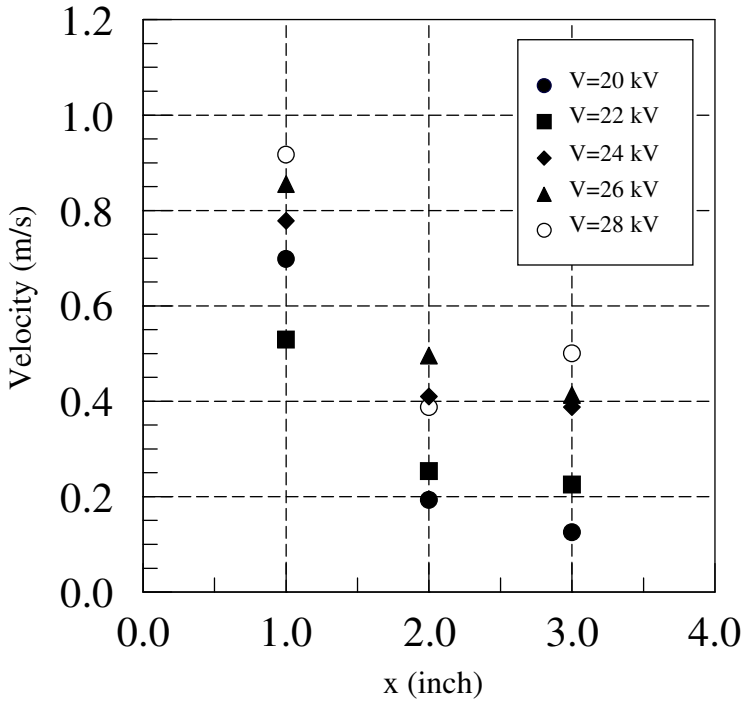

Figure A.12 Velocity profile inside channel, 12 pins, negative polarity (z=2.5 in.)

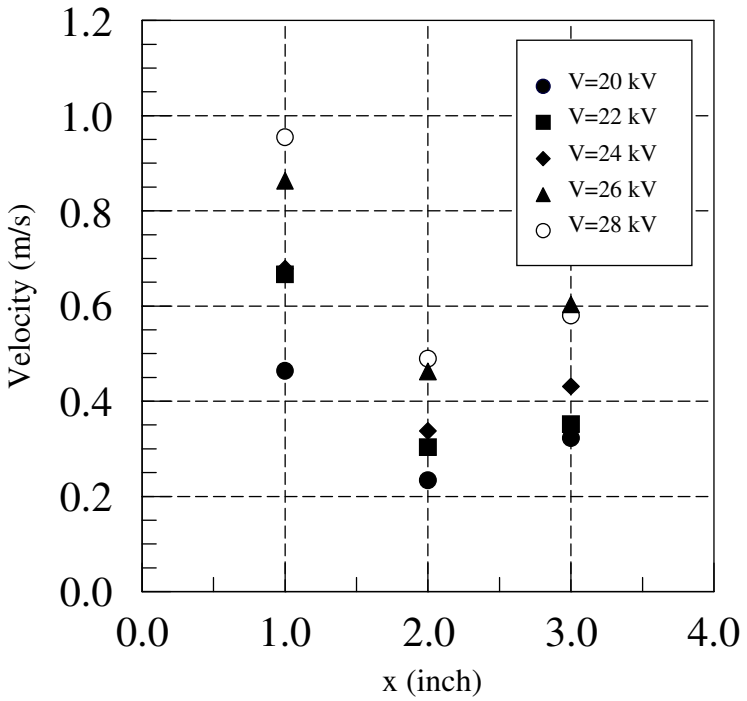

Figure A.13 Velocity profile inside channel, 12 pins, negative polarity (z=4 in.)

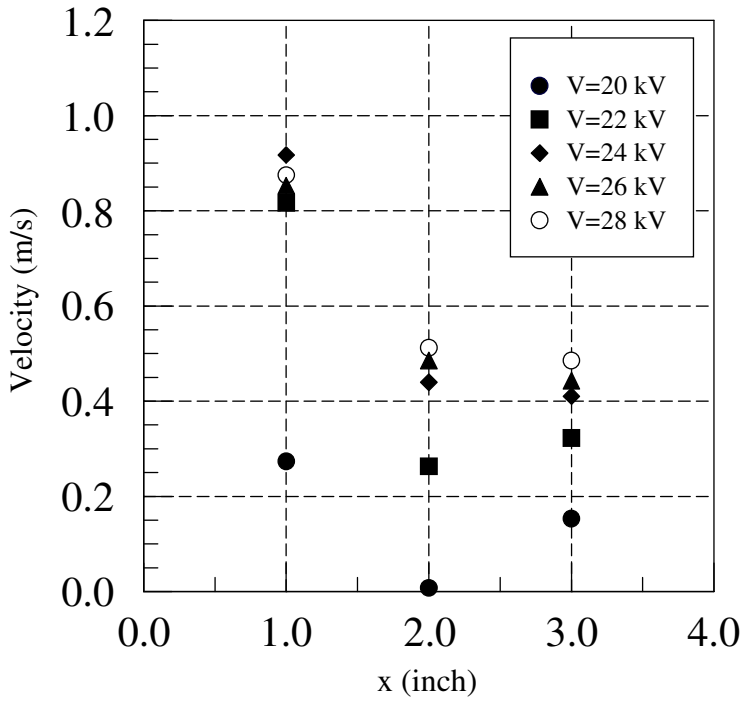

Figure A.14 Velocity profile inside channel, 4 pins, positive polarity (z=1 in.)

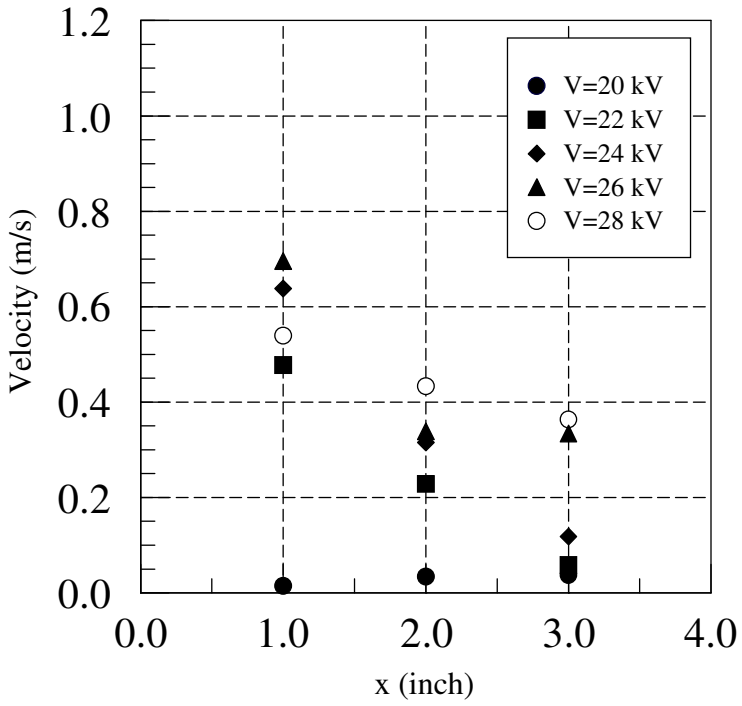

Figure A.15 Velocity profile inside channel, 4 pins, positive polarity (z=2.5 in.)

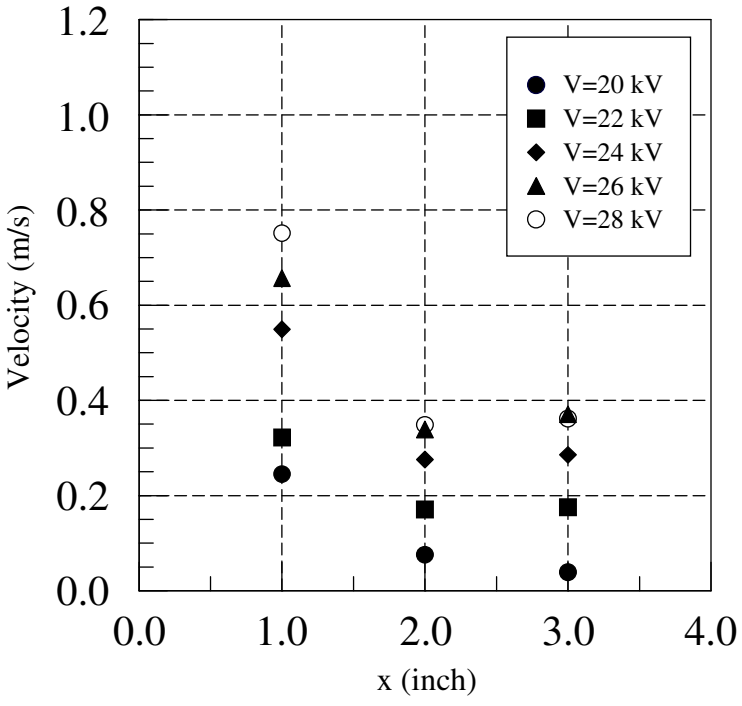

Figure A.16 Velocity profile inside channel, 4 pins, positive polarity (z=4 in.)

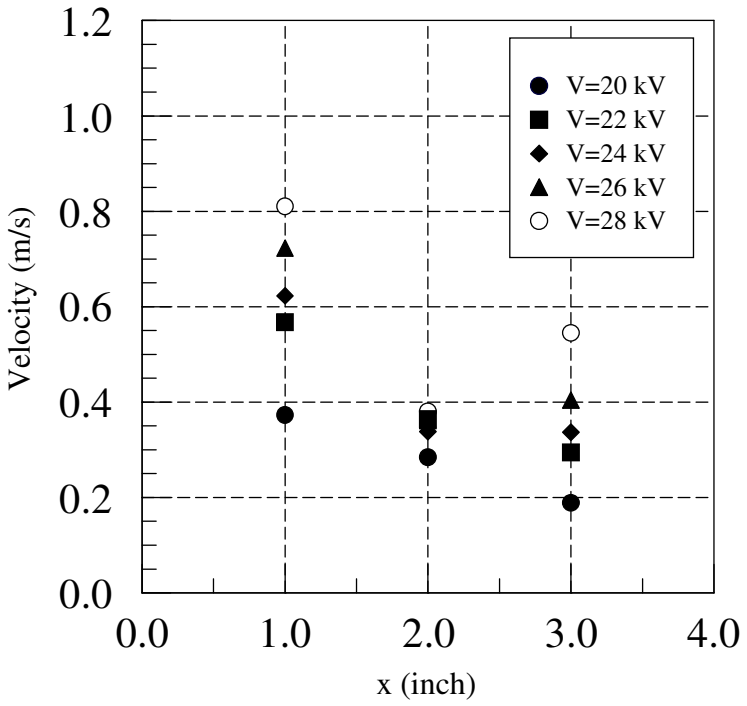

Figure A.17 Velocity profile inside channel, 4 pins, negative polarity (z=1 in.)

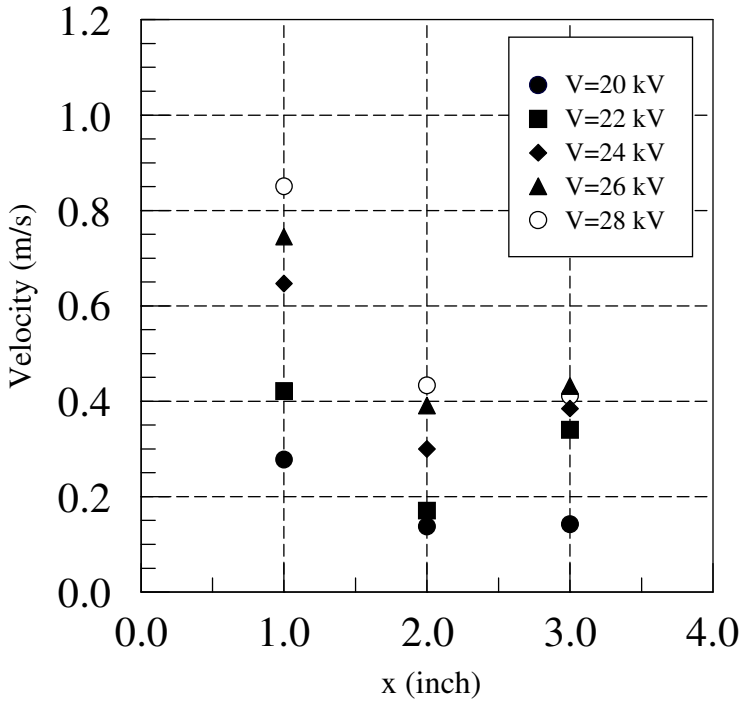

Figure A.18 Velocity profile inside channel, 4 pins, negative polarity (z=2.5 in.)

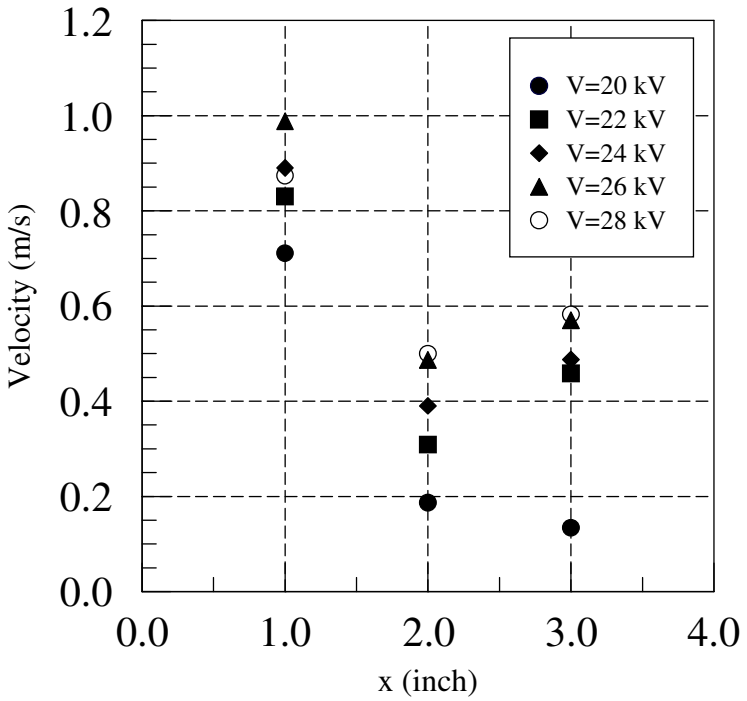

Figure A.19 Velocity profile inside channel, 4 pins, negative polarity (z=4 in.)

APPENDIX B

NUMERICAL RESULTS

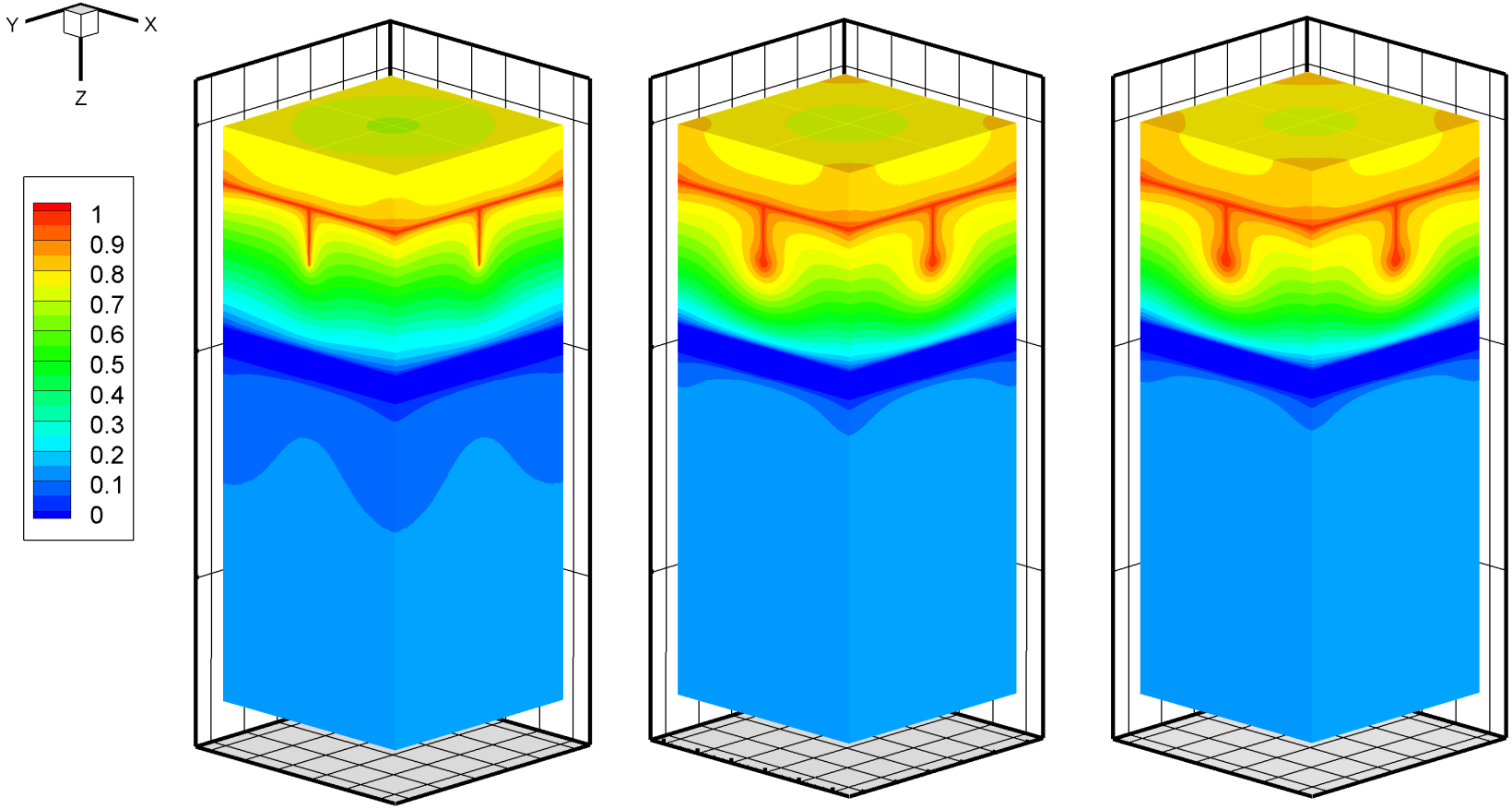

Figure B.1 Electric potential distribution of an EHD gas pump (4 pins, $\Delta\overline{V}$=0.05)
(a) V_0 = 20 kV, (b) V_0 = 24 kV, (c) V_0 = 28 kV

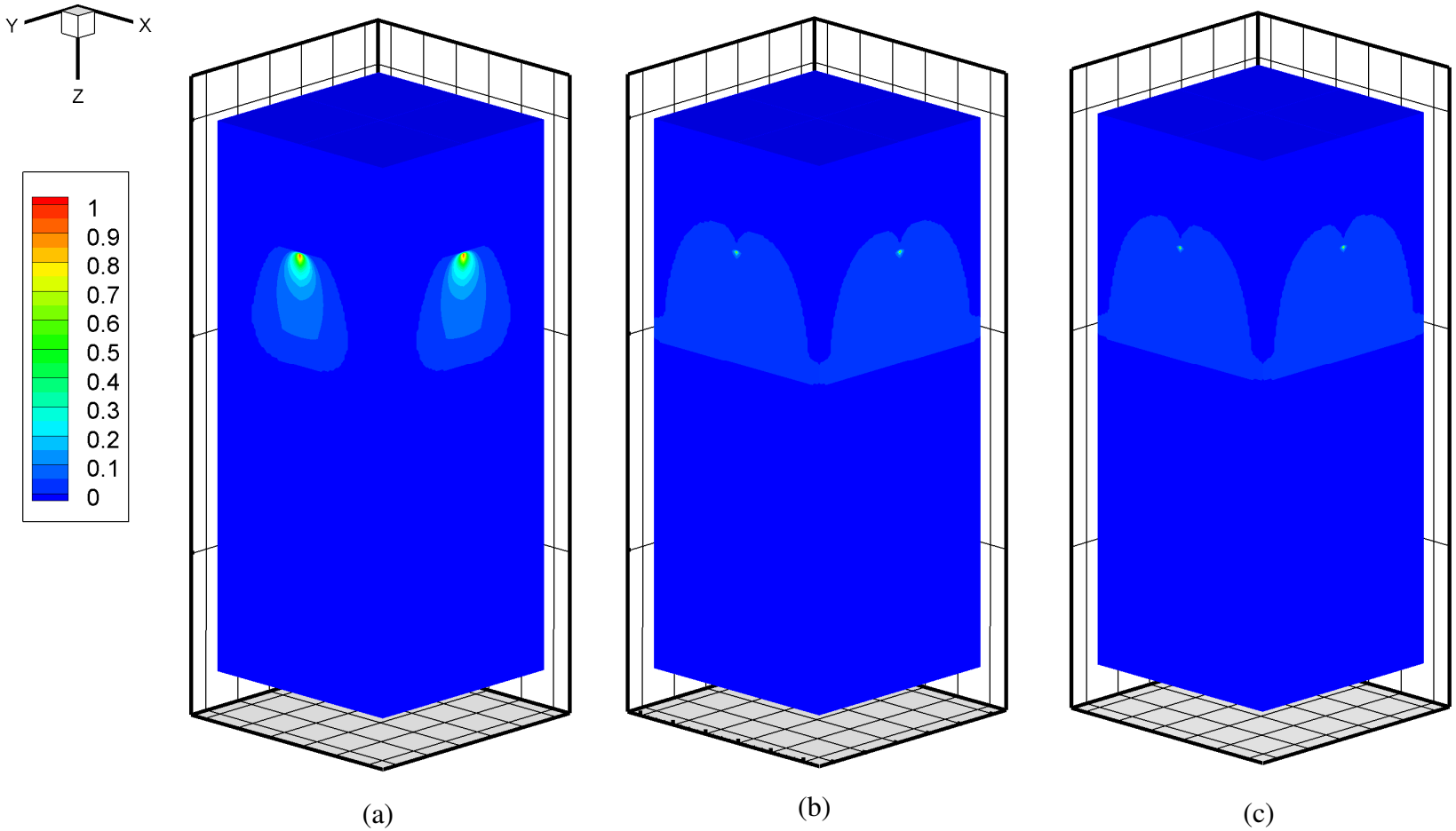

Figure B.2 Space charge distribution of an EHD gas pump (4 pins, $\overline{\Delta\rho_c} = 0.05$)
(a) $V_0 = 20$ kV, (b) $V_0 = 24$ kV, (c) $V_0 = 28$ kV

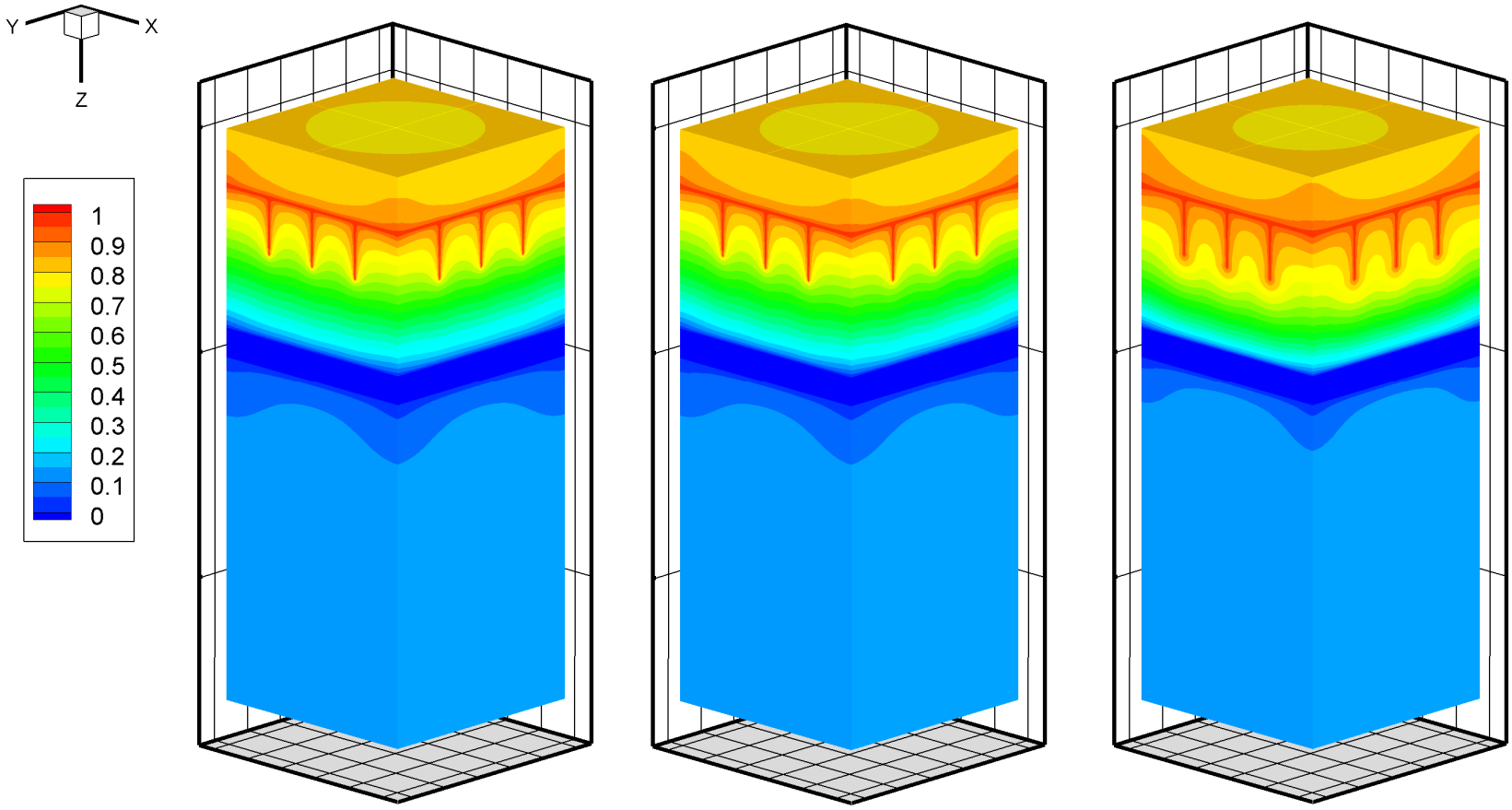

Figure B.3 Electric potential distribution of an EHD gas pump (12 pins, $\Delta\overline{V}$ =0.05)
(a) V_0 = 20 kV, (b) V_0 = 24 kV, (c) V_0 = 28 kV

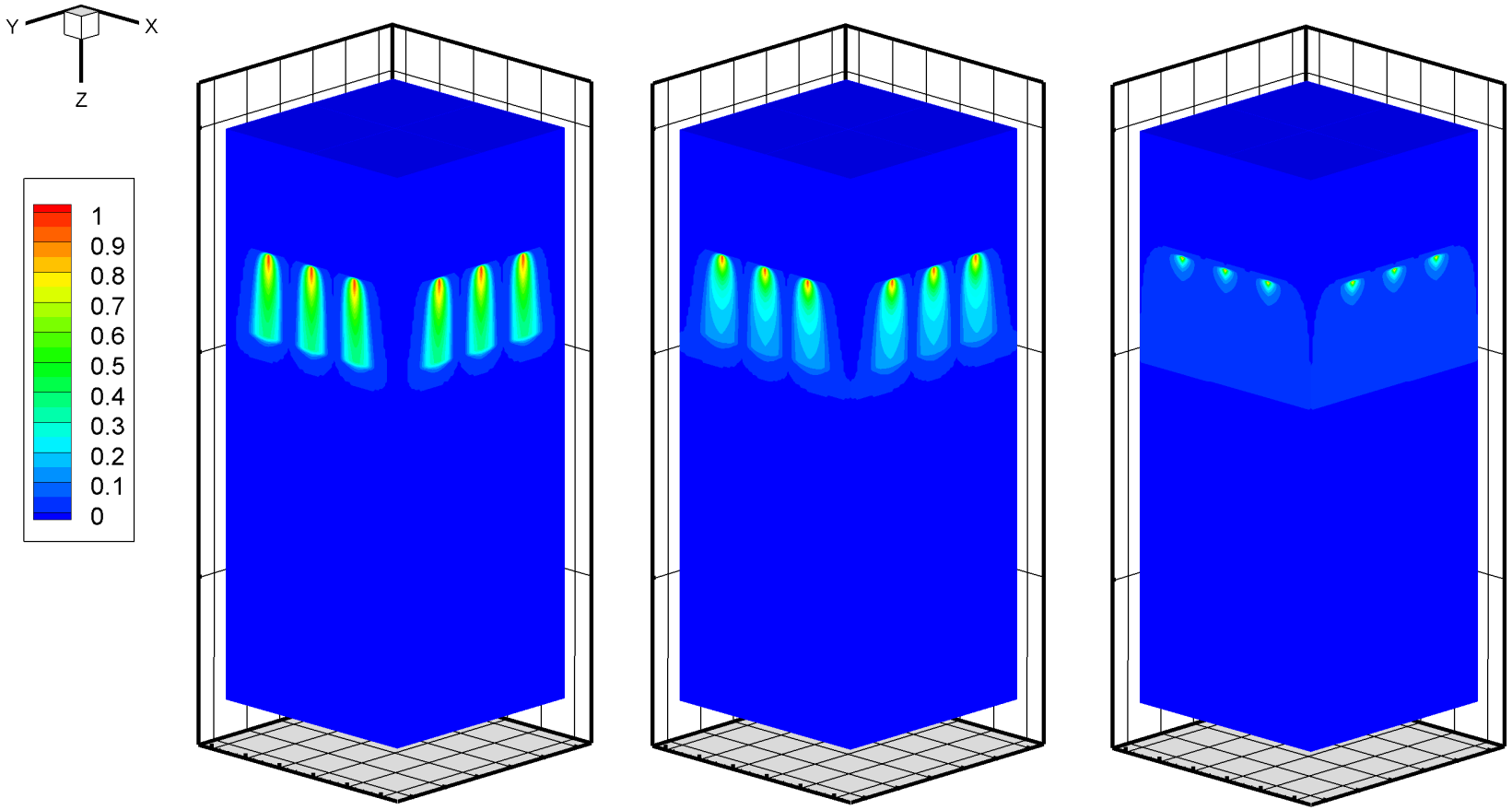

Figure B.4 Space charge distribution of an EHD gas pump (12 pins, $\Delta\overline{\rho_c} = 0.05$)
(a) $V_0 = 20$ kV, (b) $V_0 = 24$ kV, (c) $V_0 = 28$ kV

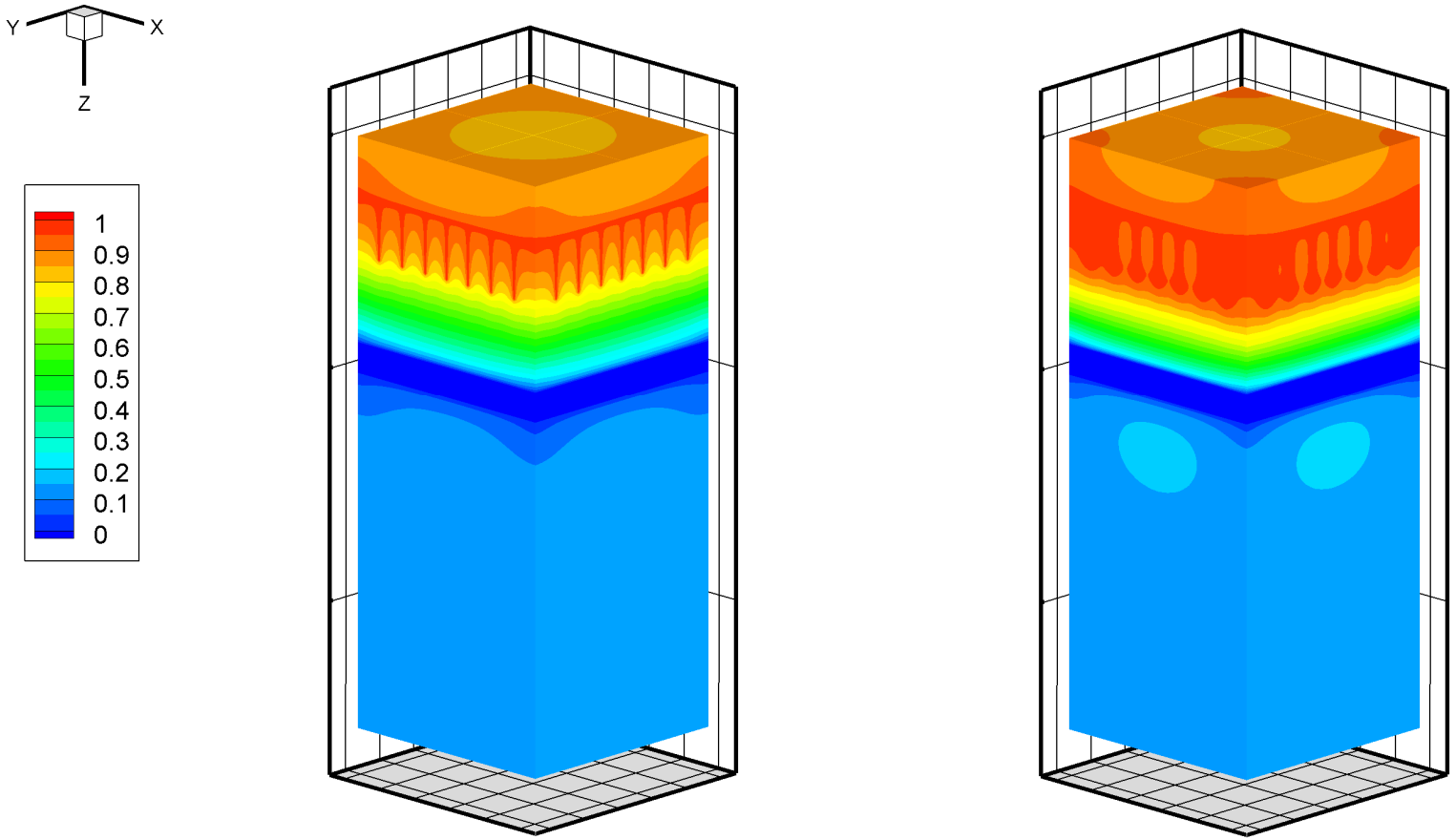

(a) (b)

Figure B.5 Electric potential distribution of an EHD gas pump (28 pins, $\Delta\overline{V}$ =0.05)
(a) V_0 = 24 kV, (b) V_0 = 28 kV

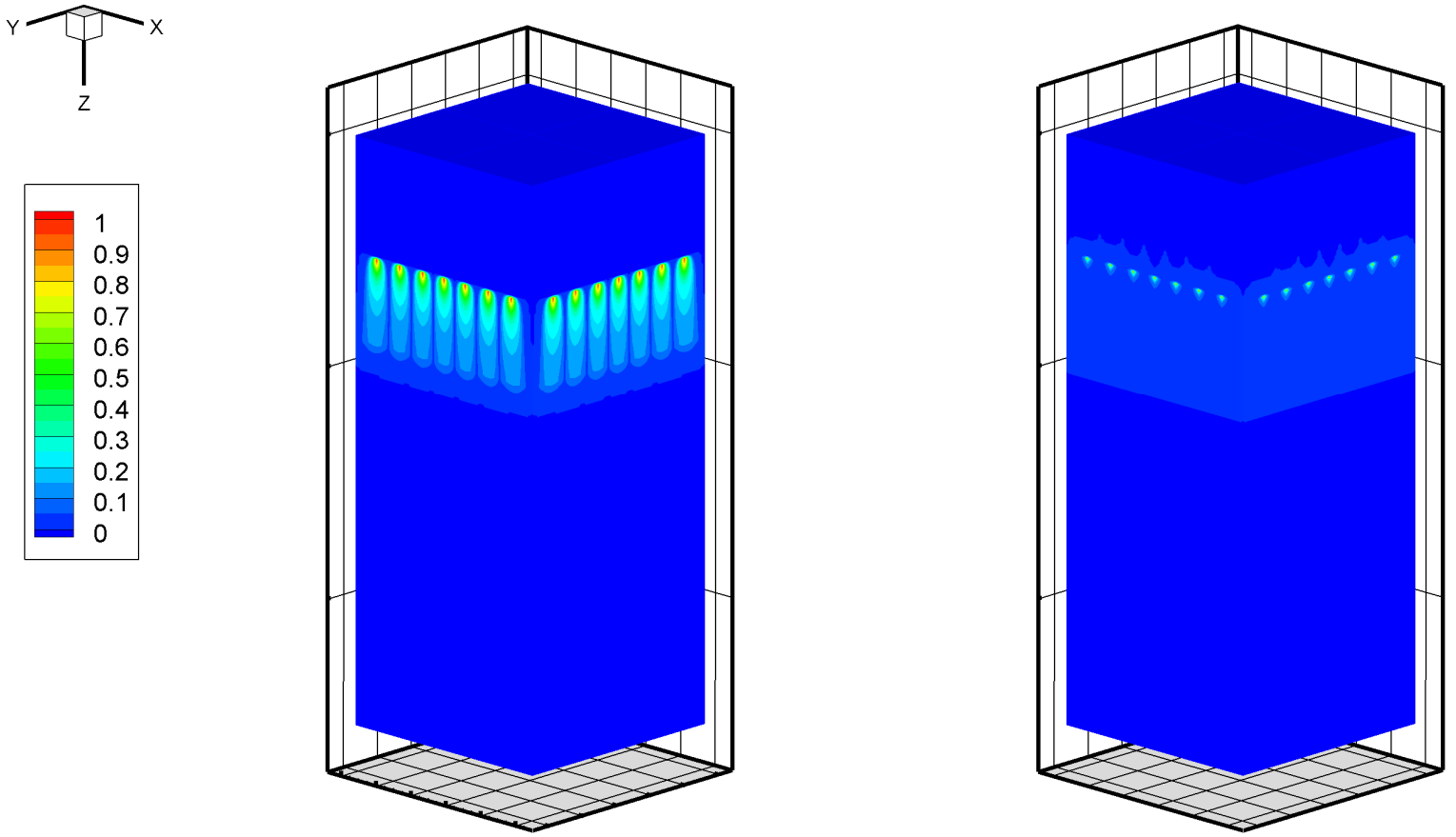

Figure B.6 Space charge distribution of an EHD gas pump (28 pins, $\Delta\overline{\rho_c} = 0.05$)
(a) $V_0 = 24$ kV, (b) $V_0 = 28$ kV

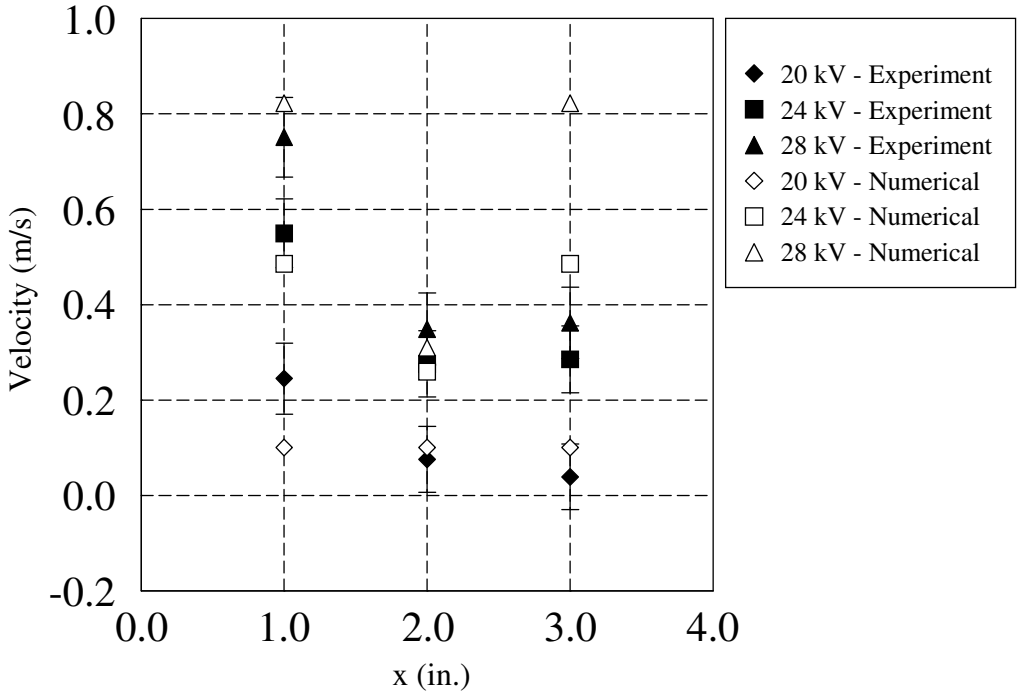

Figure B.7 Velocity profile comparison, 4 pins

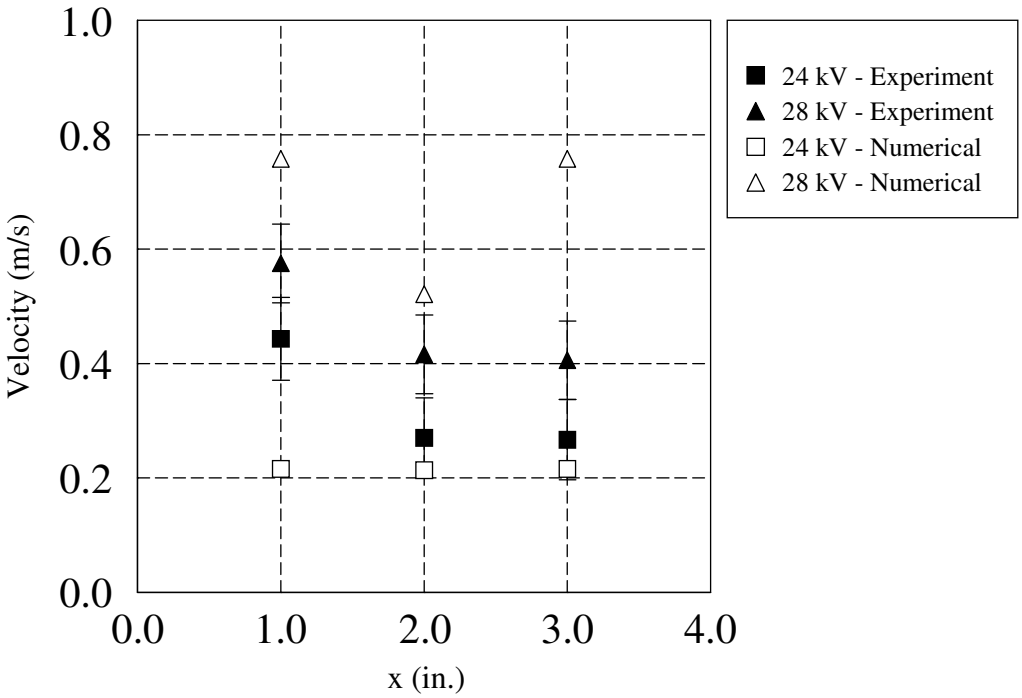

Figure B.8 Velocity profile comparison, 28 pins

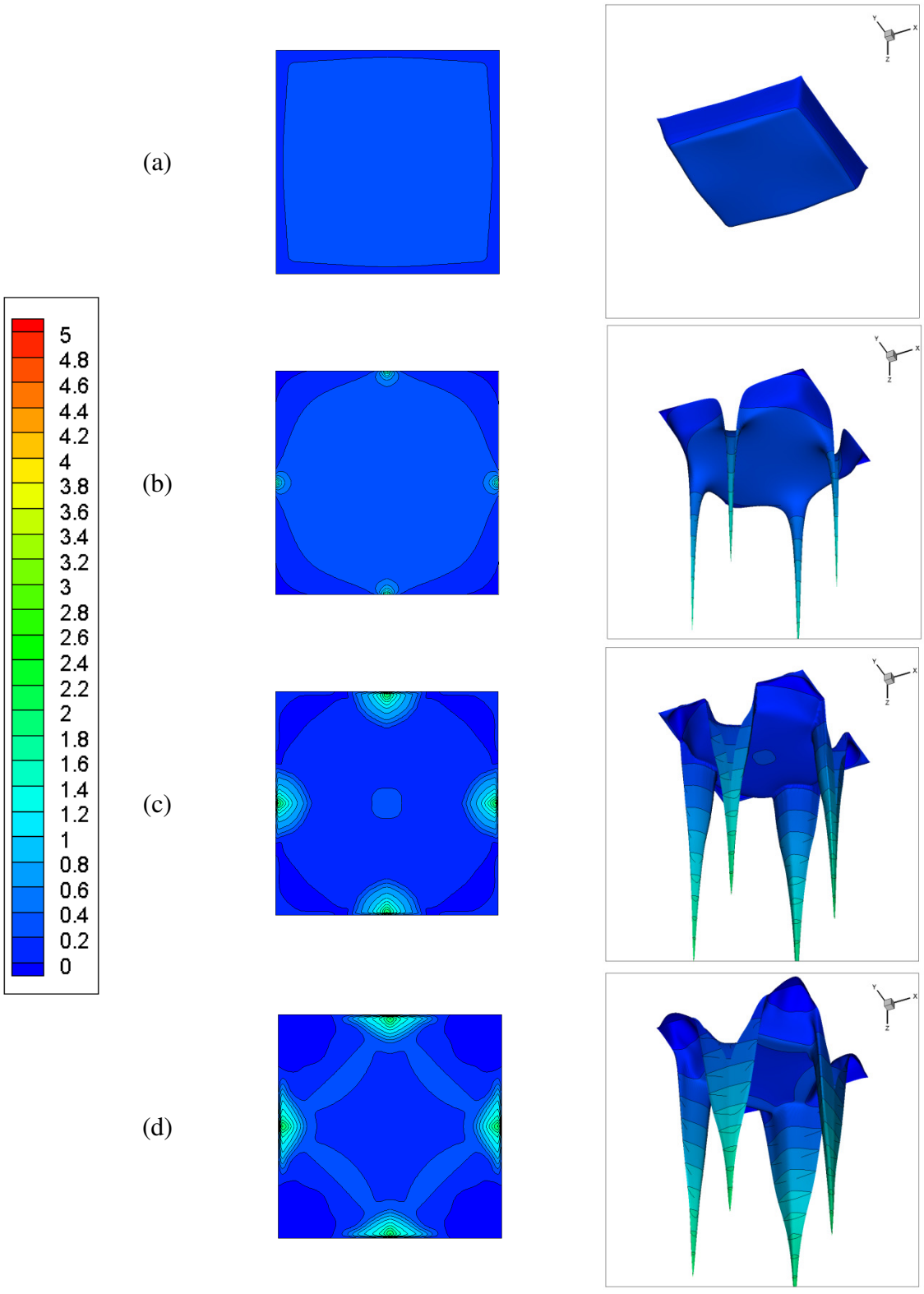

Figure B.9 EHD-induced flow field at various cross-sections (4 pins, V_0 = 20 kV)
(a) $\bar{z}$ = 1/4, (b) $\bar{z}$ = 1/2, (c) $\bar{z}$ = 3/4, (d) $\bar{z}$ = 1

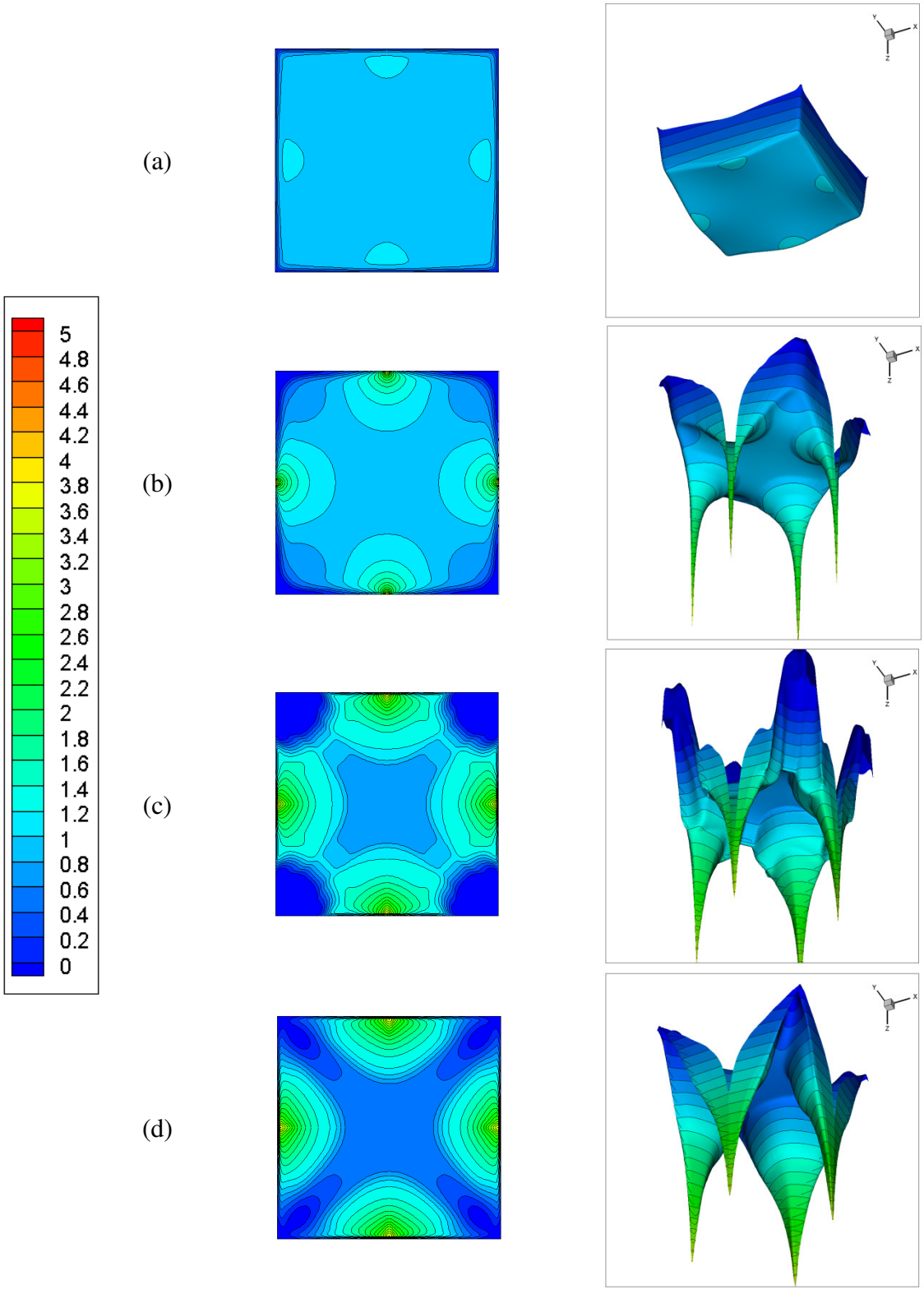

Figure B.10 EHD-induced flow field at various cross-sections (4 pins, V_0 = 24 kV)
(a) $\bar{z}$ = 1/4, (b) $\bar{z}$ = 1/2, (c) $\bar{z}$ = 3/4, (d) $\bar{z}$ = 1

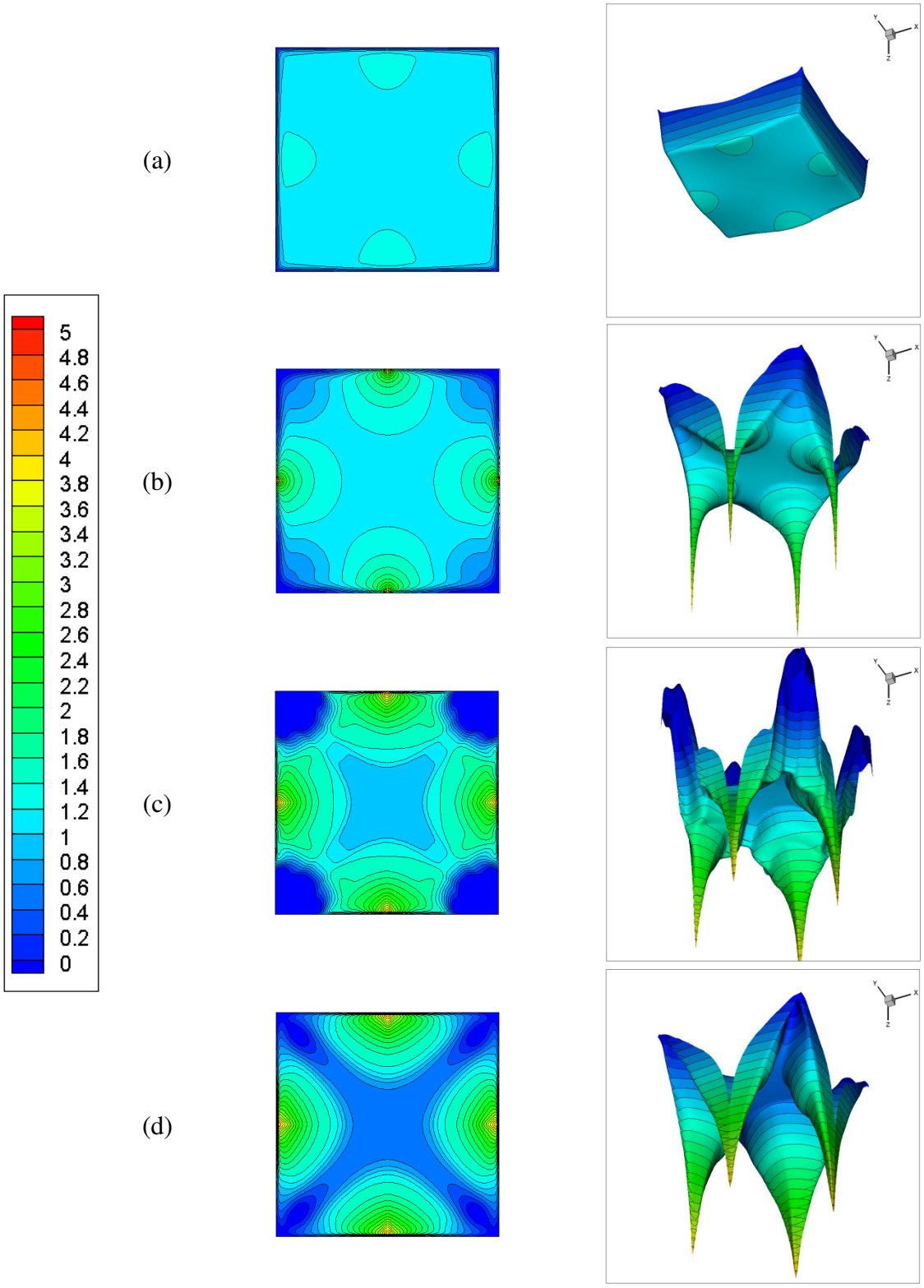

Figure B.11 EHD-induced flow field at various cross-sections (4 pins, V_0 = 28 kV)
(a) $\bar{z}$ = 1/4, (b) $\bar{z}$ = 1/2, (c) $\bar{z}$ = 3/4, (d) $\bar{z}$ = 1

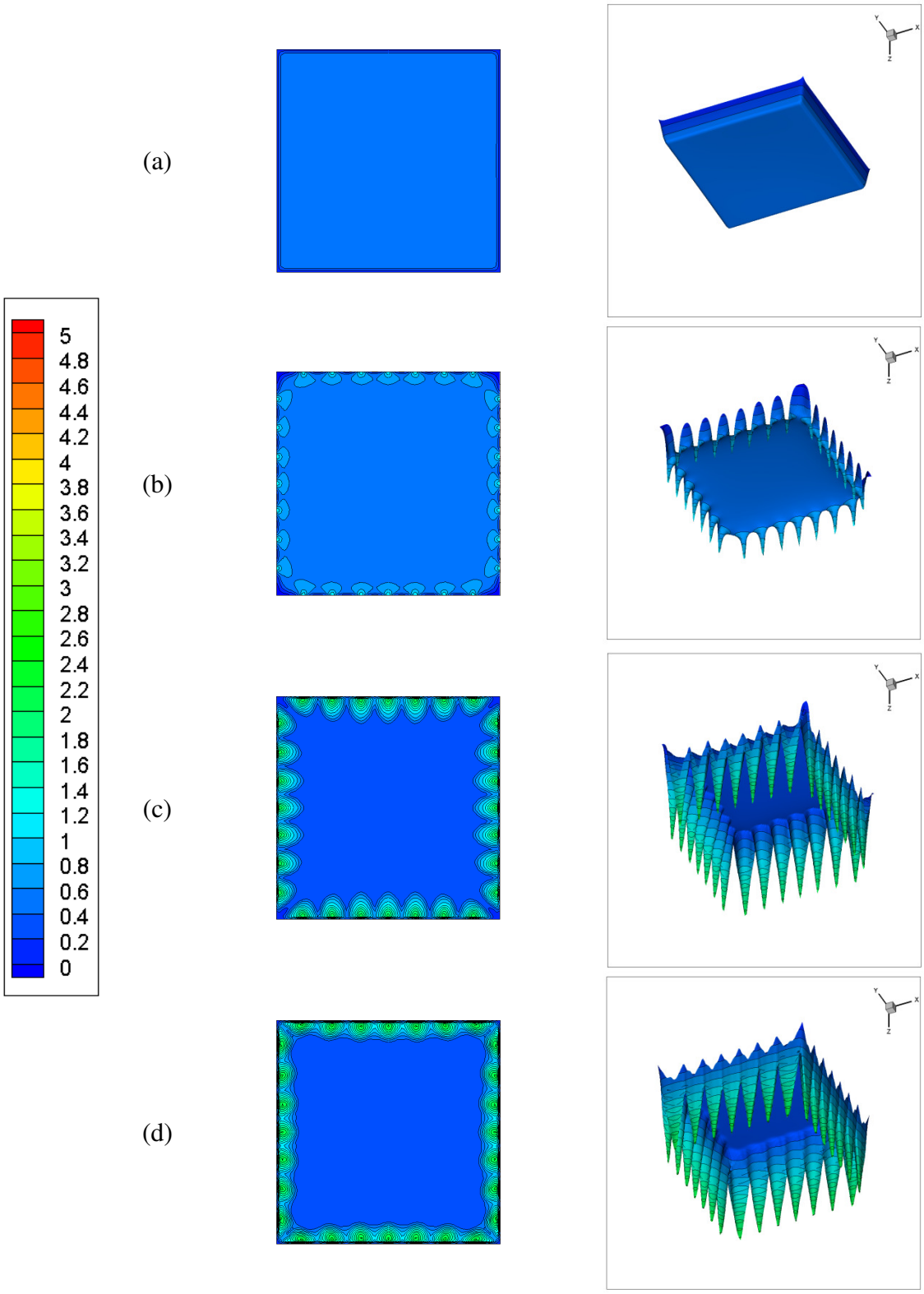

Figure B.12 EHD-induced flow field at various cross-sections (28 pins, V_0 = 24 kV)
(a) $\bar{z}$ = 1/4, (b) $\bar{z}$ = 1/2, (c) $\bar{z}$ = 3/4, (d) $\bar{z}$ = 1

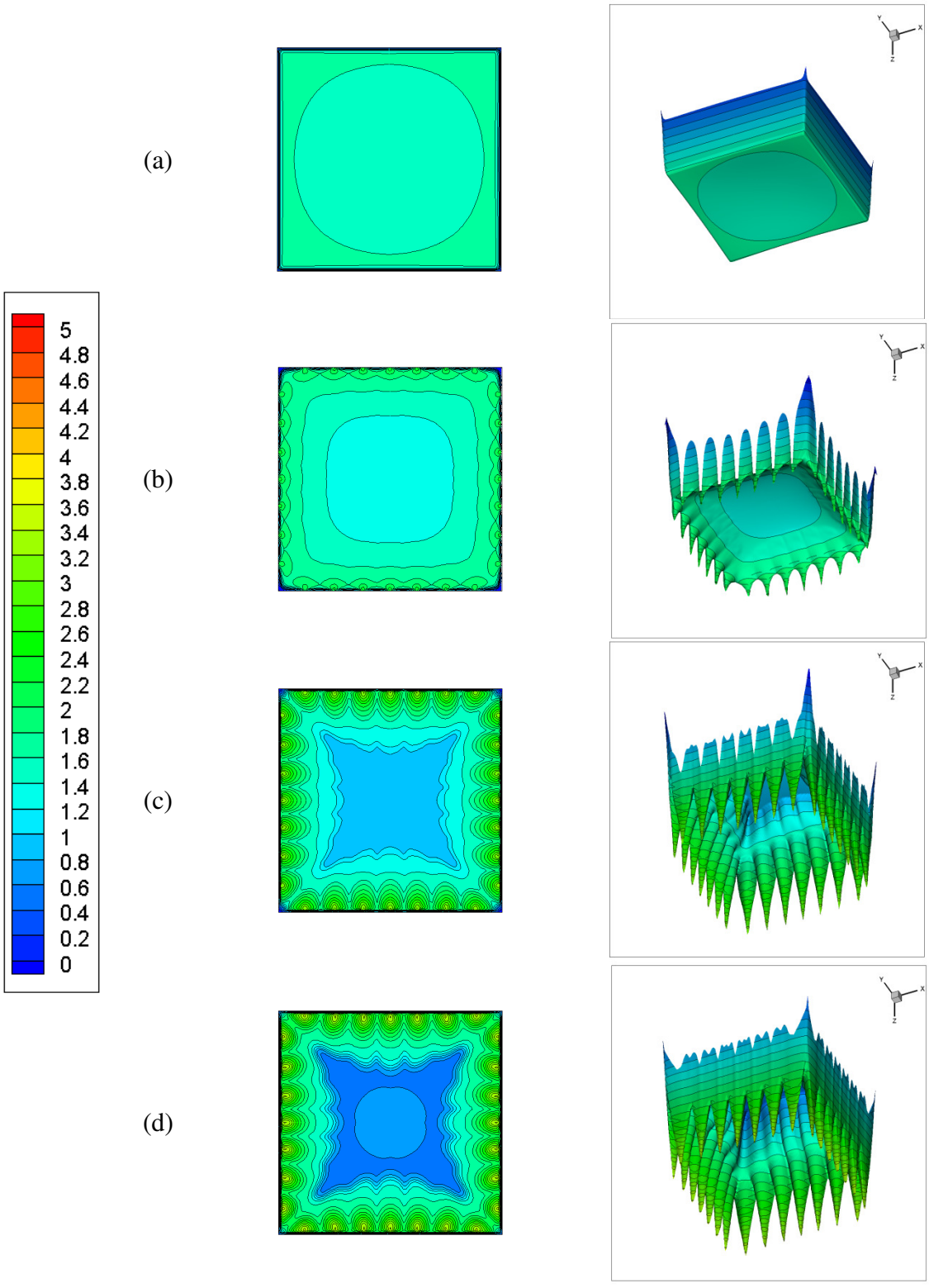

Figure B.13 EHD-induced flow field at various cross-sections (28 pins, V_0 = 28 kV)
(a) $\bar{z}$ = 1/4, (b) $\bar{z}$ = 1/2, (c) $\bar{z}$ = 3/4, (d) $\bar{z}$ = 1

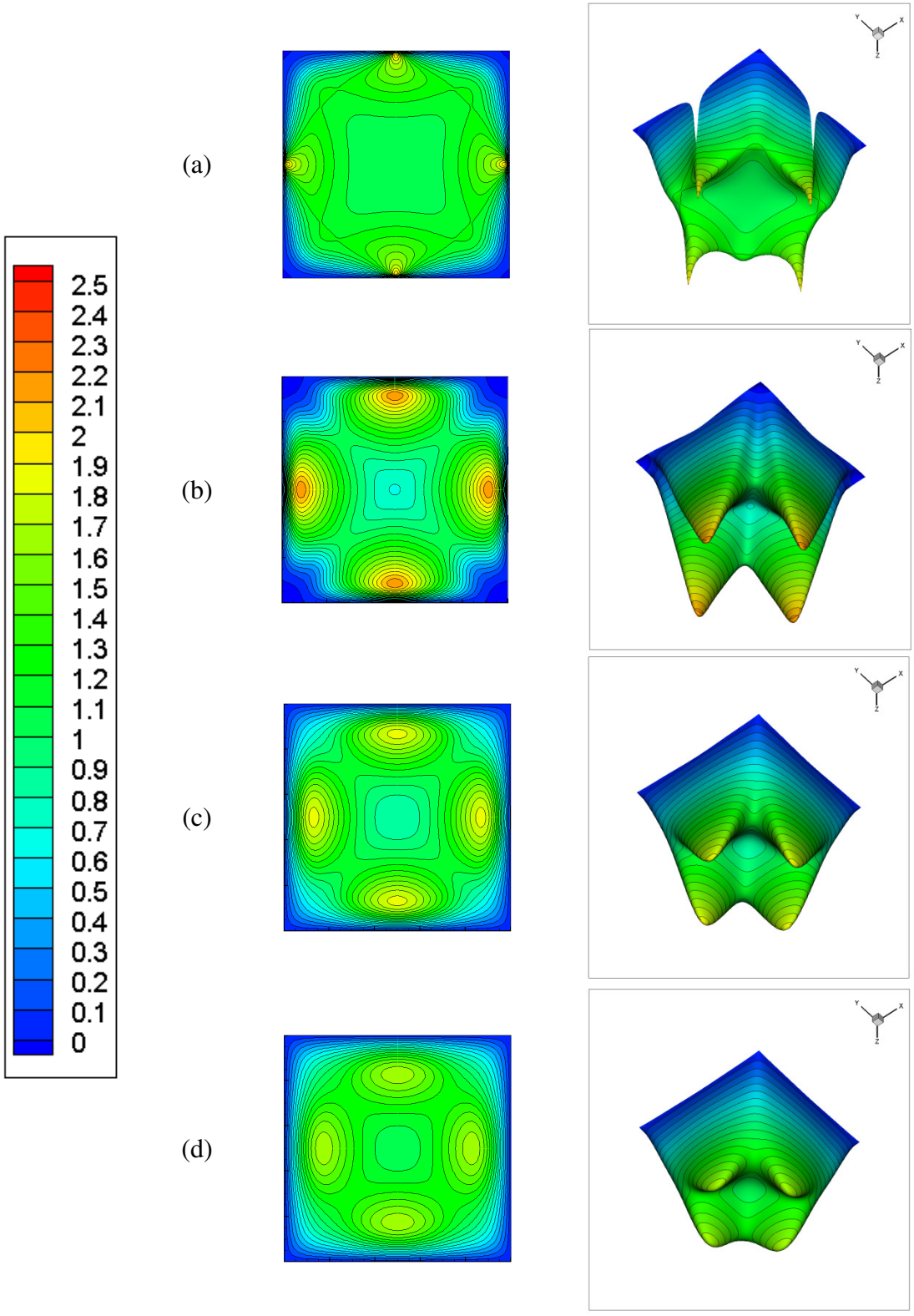

Figure B.14 Flow field for forced convection with Re = 200 at 24 kV (4 pins, $\Delta\overline{w}$ =0.1)
(a) $\overline{z}$ = 0.5, (b) $\overline{z}$ = 1, (c) $\overline{z}$ = 1.5, (d) $\overline{z}$ = 2

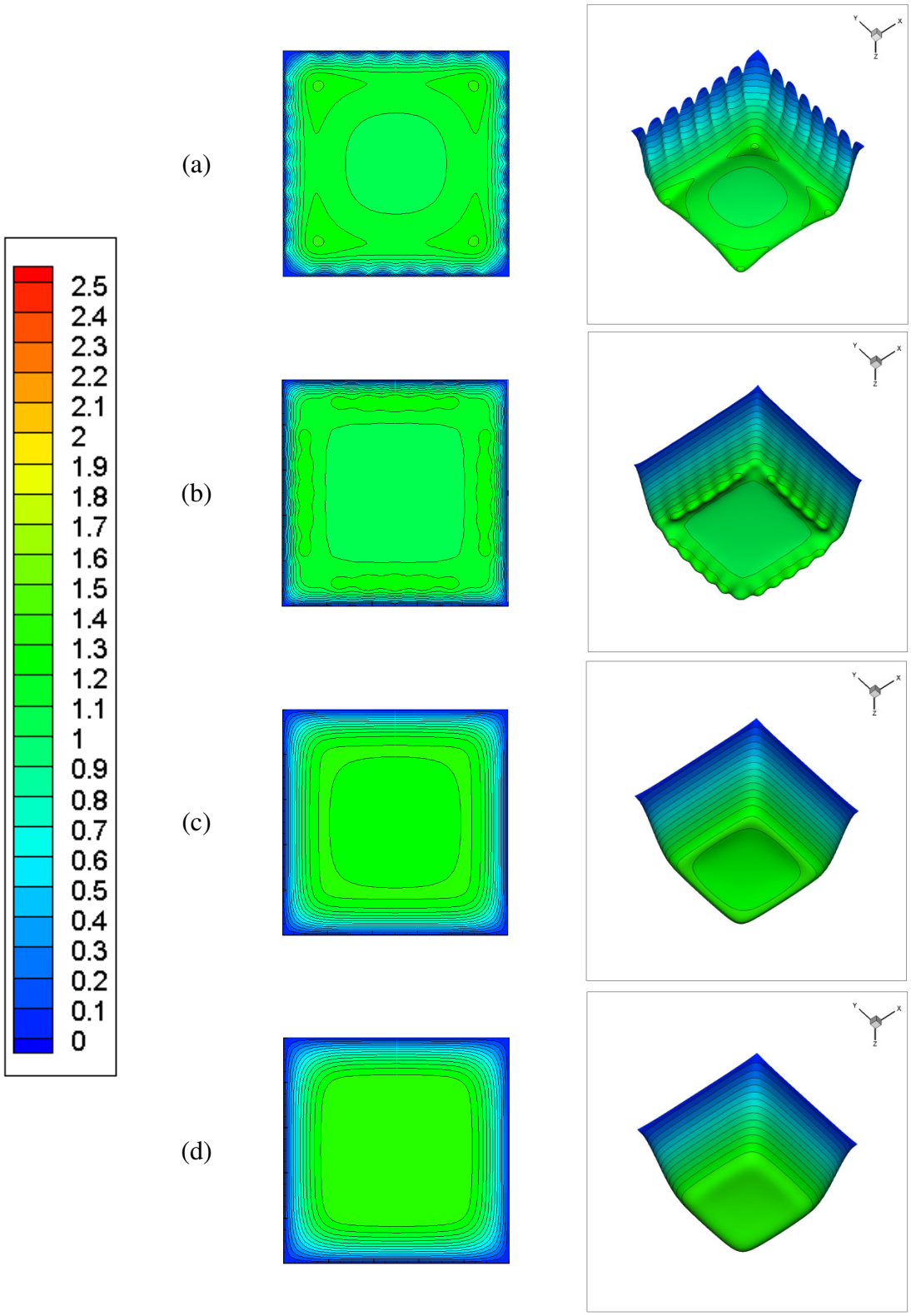

Figure B.15 Flow field for forced convection with Re = 200 at 24 kV (28 pins, $\Delta\overline{w}$ =0.1)
(a) $\overline{z}$ = 0.5, (b) $\overline{z}$ = 1, (c) $\overline{z}$ = 1.5, (d) $\overline{z}$ = 2

Table B.1 EHD number for positive corona discharge

		N_{EHD}		
	Re	V_0=20 kV	V_0=24 kV	V_0=28 kV
4 pins	200		1136.07	
	500		181.77	
	1000		45.44	
	2000		11.36	
12 pins	200	134.93	689.27	5420.35
	500	21.59	110.28	867.26
	1000	5.40	27.57	216.81
	2000	1.35	6.89	54.20
28 pins	200		3816.38	
	500		610.62	
	1000		152.66	
	2000		38.16	

NOMENCLATURE

A	Surface area of the grounded plate, [m^2]
A_s	heat transfer surface area, [m^2]
b	ion mobility, [$m^2/V \cdot s$]
d	distance between electrode tip and grounded plate, [m]
D	hydraulic diameter, [m]
$\mathbf{E}$	electric field strength, [V/m]
E_x	x-component electric field strength, [V/m]
E_y	y-component electric field strength, [V/m]
E_z	z-component electric field strength, [V/m]
f	friction factor
$\mathbf{f}_e$	electric body force, [N]
g	gravitational acceleration, [m^2/s]
h	convective heat transfer coefficient, [$W/m^2 \cdot K$]
I	total corona current, [A]
$\mathbf{J}$	current density, [A/m^2]
k	thermal conductivity, [$W/m \cdot K$]
L	channel length, [m]
L_h	hydrodynamic entry length, [m]
L_t	thermal entry length, [m]
N_{EHD}	EHD number
Nu	average Nusselt number, hD/k

Nu_x local Nusselt number, hx/k

Nu_{x0} local Nusselt number without electric field, hx/k

Nu_0 average Nusselt number without electric field, hD/k

p pressure, [Pa]

p_i pressure at the inlet, [Pa]

p_o pressure at the outlet, [Pa]

Pr Prandtl number, ν/α

$\bar{p}$ dimensionless pressure, $(p - p_i)/\rho u_i^2$

q heat flux, [W/m^2]

Re Reynolds number, $u_i D/\nu$

t time, [s]

T temperature, [K]

T_i incoming fluid temperature, [K]

T_m mean fluid temperature, [K]

T_o temperature at the outlet, [K]

T_w wall temperature, [K]

$\mathbf{u}$ fluid velocity, [m/s]

u x-component of velocity, [m/s]

u_e characteristic velocity of corona wind, $\sqrt{\rho_{c0} V_0/\rho}$

u_i inlet fluid velocity, [m/s]

u_m mean fluid velocity, [m/s]

$\bar{u}$ dimensionless velocity in x direction, u/u_i

v y-component of velocity, [m/s]

V electric potential, [V]

V_0 electric potential at the wire, [V]

$\bar{v}$ dimensionless velocity in y direction, v/u_i

$\bar{V}$ dimensionless electric potential, V/V_0

w z-component of velocity, [m/s]

$\bar{w}$ dimensionless velocity in z direction, w/u_i

x, y, z Cartesian coordinates, [m]

$\bar{x}, \bar{y}, \bar{z}$ dimensionless Cartesian coordinates

Greek Symbols

α thermal diffusivity, [m^2/s]

ε electric permittivity, [F/m]

ν kinematic viscosity, [m^2/s]

θ dimensionless temperature, $(T - T_w)/(T_i - T_w)$

θ_0 dimensionless temperature at the outlet, $(T_0 - T_w)/(T_i - T_w)$

ρ fluid density, [kg/m^3]

ρ_c space charge density, [C/m^3]

ρ_{c0} space charge density at the wire tip, [C/m^3]

$\bar{\rho}_c$ dimensionless space charge density, ρ_c/ρ_{c0}